Table of contents

Artifacts in UTE images reflect the differences in the eddy-current compensation between changing the applied shim currents versus shifting the rf frequency

F. Badar[1], D Gross[2], T Oerther[2], Y. Xia[1]

[1]Oakland University, Michigan, USA; [2]Bruker BioSpin, Rheinstetten, Germany

Introduction Ultra-short echo (UTE) MRI can visualize biological tissues and porous media that have very short T2 relaxation times [1,2]. The reduction of TE is generally done by shortening the time delay between the rf excitation pulses and the signal acquisition. This reduction makes the signals susceptible to the residual eddy currents and other imperfections in the imaging hardware, which can result in various artifacts in the UTE images. In this study, we compare the effects of the eddy-current compensation between changing the applied shim currents versus shifting the rf frequency by two different systems.

Methods Single and multiple glass tubes containing doped solutions (0.1 and 1% $CuSO_4$) were imaged using a 2D UTE sequence and a multi-slice-multi-echo (MSME) sequence. Two Bruker consoles were used: an AVANCE II (AVII) and an AVANCE IIIHD (AVIIIHD), both using the same 7T/9 cm magnet and same Bruker 25mm rf coil, and running the same Paravision 6.0.1 software. The MSME sequence had a TR of 2000ms, TE of ~ 8ms, and 256 matrix size with 25mm field of view and a bandwidth of 50kHz. The UTE sequence had the same geometry setting except for a TR of 100ms and a minimum TE of ~270µs. The premeasured gradient trajectory was acquired on a glass sphere phantom on both systems.

Results and Discussion The MSME images from both systems looked nearly identical from a 10mm single tube phantom (a, c). Artifacts on the UTE images from AVII were the bright rings around the outer edges of the tube, where the signal intensity drops sharply towards the interior (b, red arrow). Such artifact, however, was absent on the UTE images from AVIIIHD (d). The intensity profiles (e, f) illustrate clearly the differences in image intensity variations between the two pulse sequences on the same system and between the two systems with the same sequence. A further examination on UTE sequence imaged a tube of saline, on both AVII and AVIIIHD at four different echo times showed the difference in the decay curves due to the artifacts in AVII (g, h). The key differences between the two imaging systems are in the hardware architecture of the consoles, in how the B0 compensation is applied. AVII adds analogically the correction current to the shim coils; AVIIIHD, in contrast, digitally shifts the spectrometer rf frequency during data acquisition (via the FRED unit).

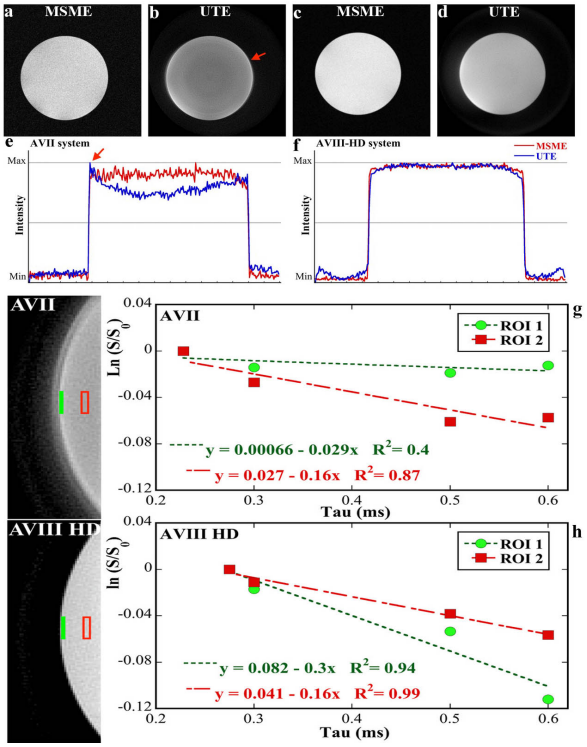

Conclusion: UTE images on AVIIIHD have minimal artifacts, which result in more reliable measure of the intensity-based quantitative MRI parameters such as the relaxation times and diffusion constants.

References: [1] Shao H, et al, Osteoarthr. Cartil. (2016). [2] Fabich HT, et al, J Magn. Reson. (2016).

Acknowledgement A Moreno and Pietro Landi (Bruker BioSpin) for tech help, and NIH R01 grant (AR69047).

Design of a lamellar phantom for validation of in vivo diffusion MRI methods

Hong Jiang[1], *João P. de Almeida Martins*[1,2], *Dan Lundberg*[3], *and Daniel Topgaard*[1]
[1]Physical Chemistry, Lund University, Sweden, [2]Random Walk Imaging AB, Lund, Sweden,
[3]CR Competence, Lund, Sweden

Introduction: Diffusion magnetic resonance imaging (MRI) is a non-invasive method that probes micrometer or millimeter-scale microstructure of biological tissue. With increased clinical demand to assess cellular changes caused by pathological conditions such as cancer, Alzheimer's disease, and tumor diseases, dMRI methods have been developed for quantifying heterogenity and anistropy in biological tissues [1,2].Therefore, a challenge for the optimization of these new diffusion MRI methods is to design phantoms that adequately reproduce the diffusion and relaxation properties of bio-tissue pathological conditions. Our work presents the design of a lamellar liquid crystal phantom which can be used in clinical MRI scanners.

Methods: Here, the chemicals used are sodium octanoate (as surfactant) and 1-decanol (as oil) and water. According to the ternary phase diagram of sodium octanoate-decanol-water system, we mixed several different samples by varying relative proportions of three components in the lamellar phase region. After observing the samples by polarized light microscopy, we chose some lamellar samples to run NMR experiments. Specifically, we measured deuterium NMR spectra and its transverse relaxation time T_2, and then recorded NMR diffusion imaging for these samples.

Results and discussion: Fig.1shows that the results from NMR experiments for this phantom. Fig.1(a) shows diffusion tensor distribution (DTD) imaging [3] of this phantom, the feature that points gathered on the bottom of each voxel indicates that the microstructure of this phantom is in pure lamellar phase. We can see almost all the points gathered the bottom of the global DTD in Fig.1(b) that further indicates that the microstructure of this phantom is pure lamellar, different color stand different orientation. We also study the microstructure with temperature variation for this sample. From Fig.(c), we can see that the microstructure of this sample is insensitive to changes temperature.

Conclusions: We obtain a phantom with homogeneous lamellar microstructure, long transverse relaxation time, insensitive to changes in temperature and easy to scale up to the size of brain for using in a clinical scanner. Such phantom may be useful to mimic the microstructure of brain tumor tissue or epidermoid cyst with flat cells.

References: [1] de Almeida Martins, Phys. Rev. Lett. (2016). [2] de Almeida Martins, Sci. Rep. (2018). [3] Topgaard, NMR Biomed. (2019).

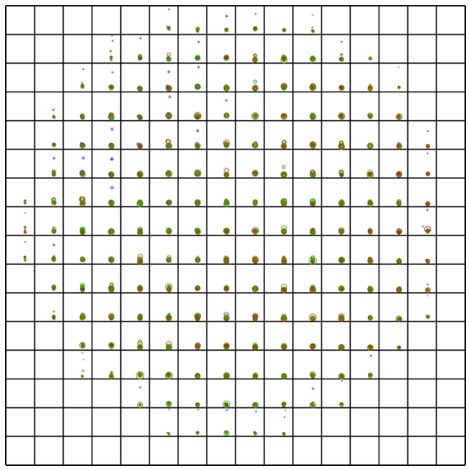

Figure 1. show results for this phantom. (a) Array of DTD imaging for every voxel. Almost all of voxel consist similar pattern that all points gathered on the bottom of each voxel, that means this phantom is in lamellar phase. (b) The corresponding DTD for the whole sample, obtains by superposition each voxel in Fig.(a). X-axis ($\log(D_{iso}/m^2\ s^{-1})$) reflects the size of diffusion tensor. Y-axis ($\log(D_\parallel/D_\perp)$) reflects the shape of the tensor. It is more intuitive to see that all the points are concentrated at the bottom of Fig.(b), that further indicates that the microstructure of this phantom is pure lamellar. Different color stand for different orientations. (c) Deuterium spectra with temperature change for this phantom. We can see it could keep pure lamellar microstructure up to 29°C, continue to heat this sample, some micelles will come out.

Diffusion tensor distribution imaging of in vivo mouse brain at ultra-high magnetic field using spatiotemporal encoding

D. Topgaard[a] *M. Yon*[b], *L. Frydman*[b]

[a]Lund University, Lund, Sweden, [b]Weizmann Institute, Rehovot, Israel

Introduction: Multidimensional diffusion encoding (MDE) yields model-free estimation of diffusion tensor distributions and resolution of multiple microscopic water environments in heterogeneous porous materials [1]. MDE has previously been combined with RARE and EPI signal read-out for investigations of liquid crystals [2] and in vivo human brain [3]. Here we introduce MDE into a spatiotemporal encoding (SPEN) [4] sequence for in vivo studies at ultra-high magnetic fields where RARE and EPI suffer from image distortions originating from, respectively, RF inhomogeneity and magnetic susceptibility differences.

Methods: In vivo mouse brain was investigated on a 15.2 T Bruker Biospec using a 180º chirp T_2*-refocused SPEN sequence [5] augmented with variable-angle spinning gradient waveforms [6,7] giving MDE as a function of the magnitude b, normalized anisotropy b_Δ, and orientation (Θ,Φ) of the diffusion encoding tensor **b**. Images were acquired with 99 × 98 μm^2 in-plane spatial resolution and 0.70 mm slice thickness at 364 points in the (b,b_Δ,Θ,Φ)-space. For every voxel, the acquired signal $S(b,b_\Delta,\Theta,\Phi)$ was subjected to Monte Carlo inversion to retrieve distributions $P(D_{iso},D_\Delta,\theta,\phi)$ defined in a 4D space of the isotropic average D_{iso} ("size"), normalized anisotropy D_Δ ("shape"), and orientation (θ,ϕ) of the diffusion tensors [1].

Results and discussion: The SPEN S_0 image in Fig 1(a) appears to be free from the distortions typical for RARE and EPI at ultra-high magnetic field. The bins in the 2D size-shape space in Fig 1(b) separate components with diffusion properties corresponding to water in white matter ("thin": low D_0, high D_Δ^2), gray matter ("thick": low D_0, low D_Δ^2), and cerebrospinal fluid ("big": high D_0), giving component-resolved parameter maps in Fig 1(c).

Conclusions: Implementation of MDE within a SPEN sequence enables 4D diffusion tensor distribution imaging in vivo at ultra-high magnetic fields.

References: [1] Topgaard, NMR Biomed. (2019). [2] Lasič. Front. Physics (2014). [3] Szczepankiewicz. Neuroimage (2015). [4] Tal, J. Magn. Reson. (2006). [5] Solomon, Magn. Reson. Med. (2017). [6] Frydman, J. Chem. Phys. (1992). [7] Topgaard, J. Magn. Reson. (2017).

Funding: Swedish Research Council (2018-03697), Swedish Foundation for Strategic Research (ITM17-0267), Israel Science Foundation (2508/17 and 965/18), NIH's Human Placenta Project (R01HD086323), the Kimmel Institute for Magnetic Resonance, and the Perlman Family Foundation.

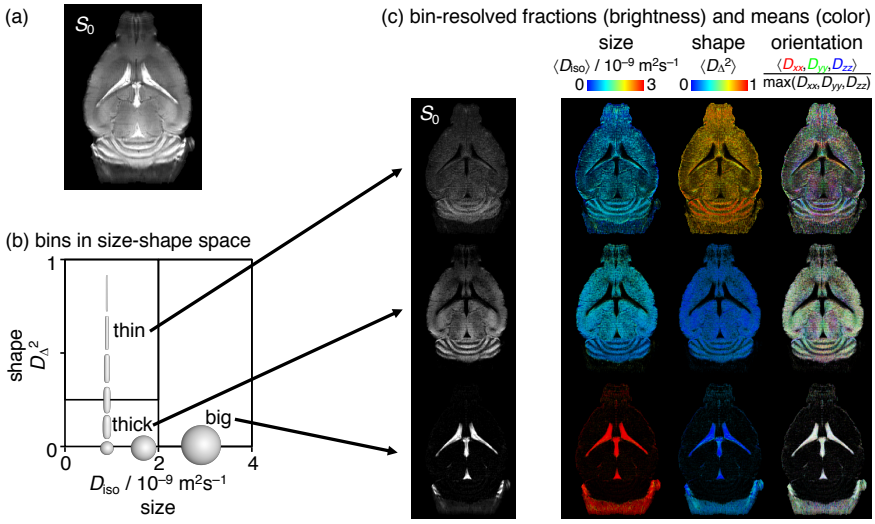

Fig. 1: Experimental results for in vivo mouse brain at 15.2 T obtained with a spatiotemporal encoding (SPEN) imaging sequence augmented with multidimensional diffusion encoding. (a) SPEN S_0 image. (b) 2D size-shape projection of the 4D size-shape-orientation space of the diffusion tensor distribution with rectangles indicating the "thin", "thick", and "big" bins. The glyphs illustrate the tensor size and shape properties. (c) Maps of S_0 and mean diffusion tensor size, shape, and orientation for each of the three bins.

Ultra high-field (17.6T) magnetic resonance microimaging reveals dysfunction of the circadian master clock in Alzheimer´s disease brain

A. Alia[a,b] , *U. Roy*[b], *S. Roßner*[c]

[a]Leiden Institute of Chemistry, Leiden University, Leiden, The Netherlands
[b]Institute of Medical Physics and Biophysics, University of Leipzig, Leipzig, Germany
[c]Paul Flechsig Institute for Brain Research, University of Leipzig, Leipzig, Germany

Introduction: In Alzheimer's disease (AD), disturbances in the circadian rhythm and sleep-wake cycle are frequently observed [1]. Circadian ryhthms are orchestrated by the master clock: the suprachiasmatic nucleus (SCN), a tiny brain area located just above the optic chiasm. *In vivo* studies to probe microstructural changes in SCN are challenging due to its very small size, especially in animal models such as mice. In the present study, we optimized ultra high-field (17.6T) *in vivo* magnetic resonance microimaging in conjunction with MR spectroscopy methods to get access to subtle microstructural changes in SCN and plaque affected brain regions of a mouse model of AD.

Methods: The transgenic mouse model of AD (Tg2576) and WT mice (n=20) were used. The experiments were performed at 17.6T vertical 89-mm bore magnets equipped with a 1 Tm^{-1} actively shielded imaging gradient insert (Bruker) using a volume coil (20 mm). During measurements, mice remained under isoflurane anesthesia and the respiration rate was constantly monitored. Images were acquired using RARE sequence and *in vivo* T_2 were followed with age (10 to 18 month) using MSME sequence as described [2]. For Multiexponential T_2 analysis, nonnegative least-squares (NNLS) algorithm was implemented using the MATLAB codes (MathWorks, Natick, MA) [2]. For 2D MRS, a localized 2D shift correlated spectroscopic sequence (L-COSY) was used [3].

Results & Discussion: Prior to the T_2 study, the test-retest reliability of *in vivo* T_2 measurements in was analyzed which was found to be very high for the SCN (ICC=0.73, P<0.05) as well as for hippocampus (ICC = 0.66, P < 0.05). The effect of CPMG refocusing interpulse interval (τ) on T_2 for the SCN, rules out any influence of magnetic field disturbances on T_2 changes. Longitudinal monitoring of *in vivo* T_2 relaxation with age shows significant shortening of T_2 in the SCN of AD mice. Multiexponential T_2 analysis detected a unique long T_2 component in SCN of AD mice which was absent in WT mice (Fig. 1). The existence of this slow relaxing component in SCN hints towards inflammation. Immunohistology revealed elevated numbers of activated astrocytes in SCN of AD mice. In addition, low neurotransmitter GABA production in SCN was detected in AD.

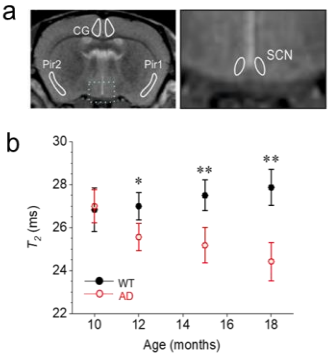

c

	WT		AD	
	T_2 (msec)	Amplitude (%)	T_2 (msec)	Amplitude (%)
Short component	5.47±2.3	0.9	10.46±2.38	1.15
Intermediate component	27.19±1.02	99.1	23.06±1.67	79.8
Long component	-		81.66±8.52	19.0

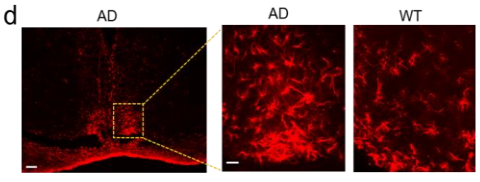

Fig 1. (a) Anatomical T_2 -weighted MR coronal slices of a mouse brain, showing SCN and other brain regions for T_2 measurements acquired with the RARE sequence at 17.6 T; (b) Age-dependent *in vivo* T_2 changes of the suprachiasmatic nucleus (SCN) of the wild-type (WT) and Tg2576 (AD) mice. Values are expressed as mean T_2 in ms ± SD (error bars) (95% C.I.). Student t- test: *p <0.05, **p <0.01; (c) Multicomponent analysis of the experimental T_2 relaxation decay curves using a non-negative least square based algorithm showing time and amplitude of various T_2 components; (d) Immunohistochemical analyses of number of astrocytes in SCN of AD and WT mice. Scale bar, 250 µm (and 60 µm in magnifications).

Conclusions: Our results demonstrate the ability of *in vivo* MR methods at ultrahigh field to detect AD-related subtle microstructural changes in SCN and support its use as a potential non-invasive diagnostic approach in early sleep disturbance in AD.

References: [1] Musiek et al Exp. Mol. Med. (2015). [2] Roy et al. J. Alzheimer Dis (2019).
[3] Braakman N, Oerther T, de Groot HJM, Alia A. Magn Reson Med (2008).

Multicomponent T_2 relaxation analysis in the muscles of Zebrafish

Muhamed N.H. Eeza[a,b], *N. Nowik*[c], *Y. Ding*[c], *Z. Zuberi*[d,e], *J. Matysik*[b], *H.P. Spaink*[c], *A. Alia*[a,e]

[a]Institute of Medical Physics & Biophysics, Leipzig University, Germany; [b]Institute of Analytical Chemistry, Leipzig University, Germany; [c]Leiden Institute of Biology, Leiden University, The Netherlands; [d]The School of Pharmacy &Pharmaceutical Sciences, Trinity College, Dublin, Ireland; [e]Leiden Institute of Chemistry, Leiden University, Leiden, The Netherlands.

Introduction: The zebrafish has emerged as an excellent model organism for studies of vertebrate diseases and hormone response mechanisms [1]. Leptin is an anorectic hormone that plays a key role in controlled food intake & energy homeostasis. Skeletal muscle constitutes an important target for leptin and recent studies show that leptin deficiency may lead to muscular atrophy [2]. However, mechanistic view on leptin deficiency induced structural and metabolic changes in muscles have not been studied so far. In this study we used state-of-the-art magnetic resonance methods to explore muscle wasting in leptin receptor deficient (Lep $^{-/-}$) zebrafish model. Changes in T_2 relaxation times in conjunction with multiexponential T_2 relaxation analysis and chemical shift selective imaging provided quantitative information of the microstructural changes in muscles of zebrafish.

Methods: Magnetic resonance microimaging (μMRI) measurements were performed on a vertical wide-bore 7T Bruker spectrometer using birdcage radiofrequency coil (10 mm). Anatomical images were acquired using rapid acquisition with relaxation enhancement (RARE) sequence [1]. The fat mapping was done using CHESS sequence [TR=1s, TE=3.4 ms, FOV=22 cm^2 and matrix =128^2]. Multi-spin multi-echo (MSME) pulse sequence with 28 echoes and refocusing interpulse interval of 5.2 ms, TR=2500 ms was used for T_2 mapping. For T_2 multicomponent analysis, nonnegative least-squares (NNLS) algorithm was implemented using the MATLAB codes (MathWorks, Natick, MA) as described recently [3]. Wild-type (WT) and Lep$^{-/-}$ zebrafish (n=10) were used in this study.

Results and Discussion: RARE imaging show significant structural changes in the muscles of mutant Lep$^{-/-}$ zebrafish. The T_2 relaxation times were changed at various regions in the muscles of Lep$^{-/-}$ as compared to WT zebrafish (Fig. 1). The T_2 multicomponent analysis of WT zebrafish muscle shows three well-distinguished components: A short T_2 component represented 17.84 ± 2% of the total curve area. An intermediate T_2 component with size 81.56 ± 5% and a long T_2 component of 0,6 ± 0.3%. The changes in the magnitude and time of these three components in muscles of Lep$^{-/-}$ zebrafish related to specific microstructural changes will be discussed.

Conclusion: The results of this study demonstrate that the muscles of Lep$^{-/-}$ zebrafish undergoes several microstructural changes in comparison to WT zebrafish, such as the increase of T_2 values, the increase of fat infiltration within the muscle fiber, the lower muscle cross sectional area and the difference of T_2 multicomponent characteristics.

References: [1] Kabli S, Spaink HP, De Groot HJ, Alia A. *J. Mag. Res. Imag.* (2009); [2] Friedman J.M. *Metabolism Clinical and Experimental* (2015); Roy U *et al. J. Alzheimer's Disease* (2019).

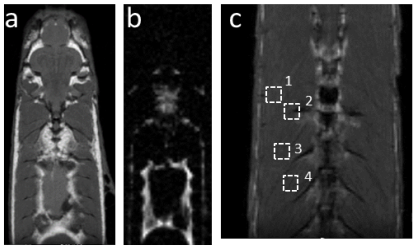

Area	T_2 (ms)	
	WT	Lep $^{-/-}$
SM1	22.6 ± 0.38	30.3 ± 1.26
SM2	23.8 ± 0.26	31.6 ± 0.96
SM3	21.2 ± 0.39	29.7 ± 0.76
SM4	22.7 ± 0.64	29.9 ± 0.62

Fig. 1: RARE image (a) and CHESS image (b) of Lep-/- zebrafish showing fat deposition and fat infiltration in muscles . (c) Regions for T_2 relaxation time measurement in various muscle areas. (d) T_2 relaxation time in WT and Lep-/- zebrafish in 4 selected somatic muscle areas. Data represents the mean T2 in ms ± standard deviation (SD) .

Identification of water compartments in spinal cords by deuterium double quantum-filtered NMR

U. Eliav, H. Shinar, G. Navon
School of Chemistry, Tel Aviv University Tel Aviv, Israel

Introduction: The identification and characterization of water compartments in neuronal tissues is commonly done on the basis of differences of their proton relaxation times and diffusion characteristics. [1]. In ^{2}H double quantum filtered (DQF) NMR the various water compartments are characterized by their different residual quadrupolar interactions [2]. The distinct quadrupolar-spit spectra enable also to study the water exchange between the compartments.

Methods: Excised porcine spinal cords were eaquilibrated in D_2O saline. The pulse sequence used to resolve the ^{2}H quadrupolar splitting was the DQF-MT: 90^o-τ-90^o-t_{DQ}-90^o-τ-90^o-t_{LM}-acq, where the double quantum coherence during the period t_{DQ} is selected by suitable phase cycling and the acq can used either for spectroscopic or imaging purpose [3, 4]. The intensity of signal is given by $\sin^2(\omega_Q\tau)$ which for $\omega_Q\tau << 1$ is $(\omega_Q\tau)^2$. Thus, by setting τ to a specific value we select compartment characterized by specific value of ω_Q.

Results and discussion

In Fig. 1 the dependence of the spectra obtained by the pulse sequence DQF-MT on τ is shown. Five different types of spectra are observed: Three pairs of quadrupolar split satellites with splitting of ~1500 (not shown), 550 and 400 Hz. (The 400 Hz is better resolved at lower temperatures) and two unresolved spectra with linewidths of about 400 and 20Hz that are most noticeable for τ =1.75 and 3 ms. By varying t_{LM} exchange among the various compartments was measured. The splitting of 550 Hz has been previously observed also in sciatic and optic nerve [2, 5] and were assigned to myelin water. ^{2}H DQF-MT image (Fig 2) obtained with τ=0.8 ms optimised for the 550 Hz splitting indicates that it is mostly originates from the white matter. Changing the orientation of the spinal cord symmetry axis with respect to the magnetic field by 0^o, 90^o and 54.7^o have shown that the 550 Hz splitting is hardly changed. Thus, indicating liquid-crystalline nature.

Conclusion: ^{2}H NMR is a very useful method for the study of the components of the nervous system. One of the advantages of this technique over the ^{1}H studies is that the various water sites can be distinguished by their different quadrupolar interactions. This enables to study ~~each~~ the five water sites independently and also to study the magnetization transfer among them.

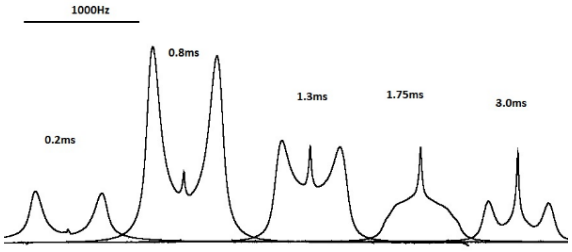

Fig 1,

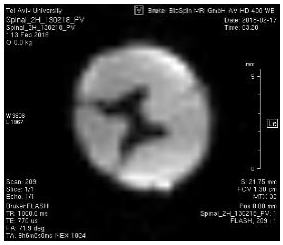

Fig. 2.

References: [1] Does, Neuroimage (2018). [2] Shinar, J. Magn. Reson. (1997). [3] Eliav, J. Magn.Reson. (1999). [4] Neufeld, Magn. Reson. Med. (2003). [5] Shinar, Proc. ESMRMB (2006).

An in vivo Continuous Sequential 3D MRM Study of Honey Bee Metamorphosis

A. Mohorič[a,b], *J. Božič*[c], *K. Tušar*[a], *Y. I. Ye*[c], *A. Sepe*[b], *U. Mikac*[b], *I. Serša*[b]

[a]Faculty of mathematics and physics, University of Ljubljana, Ljubljana, Slovenia, [b]Jožef Stefan Institute, Ljubljana, Slovenia, [c]Biotechnical Faculty, University of Ljubljana, Ljubljana, Slovenia

Introduction: Insects are ideal samples for studies with MRM because of their size and optimal water/lipid content [1]. MRM has been successfully employed to study morphology of honey bees [2], wasp metamorphosis [3], organ systems [4-6] or to follow lipid content in insects [7] and research of parasite/host relationship [8]. In this study, metamorphosis of Apis mellifera carnica was studied by sequential 3D MRM of the same specimen. The images were analyzed for information on transformation of individual organs, systems and tissues such as tracheal system, gastrointestinal tract and muscles. Image segmentation was used to obtain morphological changes of the body systems and also to calculate their volumes and compositional changes as a function of time.

Methods: A specimen was kept in a capped honeycomb cell at constant humidity and temperature during 14 days of experiment. The study was performed on a 9.4 T MRM system and a 3D T1-weighted spin-echo imaging scan made every four hours with 78 μm spatial resolution. Tracheal system and gastrointestinal tract were segmented and corresponding volumes were determined as a function of time after beginning of metamorphosis.

Results and discussion: Metamorphosis of organs and the internal structure of the bee can be seen in Fig 1. Surprising is a sudden transformation of prepupa to pupa at 70h. Gastrointestinal tract is first elongated and then twists, gets wider and starts growing towards the thorax section. Tracheal system is shown in the coronal view. Volume rendering analysis is shown in Fig 2. The metamorphosis process took 12 days. Graph of bee volume as a function of time is showing a constant decrease, explained by use of nutrients. In the case of the tracheal system, only major tracheal sacks can be seen in MR images due to limited resolution. Fat-content-sensitive T1-wighted imaging enabled a good discrimination between fat-rich tissues and as well improved morphological visualization of different sections of the bee needed for compositional analysis.

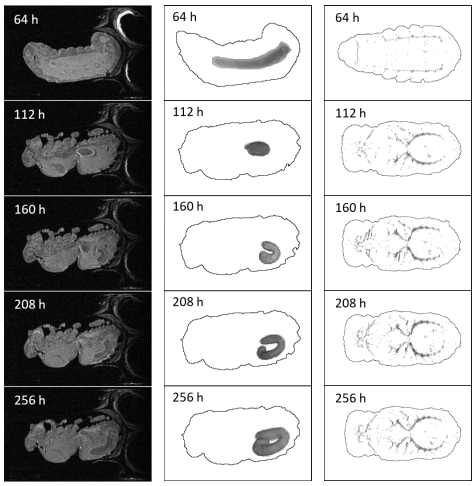

Fig. 1: A few samples of a time series of a bee metamorphosis: left column – sagittal slice of a 3D sequential images, central column – gastrointestinal tract, right column – tracheal system.

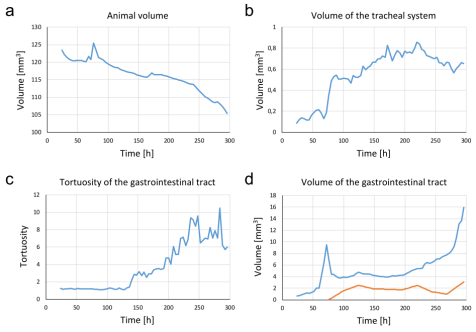

Fig. 2: Volume of specimen (a), tracheal (b) and gastrointestinal (d) systems and its tortuosity (c) as a function of time.

Conclusion: The study confirms MRM as a powerful tool for analysis of morphological and compositional changes of small insects and gives a clear insight into the entire metamorphosis process. The study is important also from the perspective of universality as it can be easily adapted for studying metamorphosis of other insects or any similar incremental biological process on a similar spatial and temporal scale.

References: [1] Hart, J Insect Sci. (2003). [2] Tomanek, J Apicult Res. (1996). [3] Chudek, Magn Reson I. (1996). [4] Haddad, J Insect Sci. (2004). [5] Michaelis, Neuroimage (2005). [6] Watanabe, J Neurosci Meth. (2006). [7] Schilling, J. Exp. Biol. (2012). [8] Chudek, Spatially Resolved Magnetic Resonance, Wiley-VCH (1998).

Minimally invasive implantable NMR microcoil for in vivo MRS and MRI in submicroliter volumes

Y. Crémillieux[1], *V.T. T. Pham*[1], *N. Pinaud*[1], *A. Wong*[2]

[1]Institut des Sciences Moléculaires, UMR 5255, Université de Bordeaux, France
[2]Nimbe, CEA-Saclay, UMR 3685, Gif-sur-Yvette, France

Introduction: The use of implanted NMR microcoils still remains a relatively unexploited research area, without emerging or significant biomedical applications. In this study, we present in vitro and in vivo results obtained with innovative and minimally invasive microcoils.

Methods: An example of implantable NMR microprobe is shown in Figure 1. This filar-type architecture is based on the use of twisted copper microwires (diameter of 150 µm). The twisted wires are inserted inside a polyamide tubing (inner and outer diameter of 350 and 380 µm). A biocompatible glue is used to seal the polyamide tube and to the two sides of the wire are connected to variable tuning and matching capacitors. In vitro and in vivo experiments were performed on a 7 T Bruker MRI scanner. NMR spectra were acquired using a PRESS sequence. 3D MRI acquisitions were performed using ZTE sequence. Male Wistar rats were used for in vivo experiments.

Results and discussion:

The quality factor of the loaded coils was ranging between 50 and 60. The FWHM's of water peak were measured to 6 Hz with a detection proximity of about 200 µm apart from the wire. In vivo results are illustrated in Figure 2 with NMR spectra obtained in the rat brain (acquisition time 10 min). The main peaks of brain metabolites are visible and quantifiable. The ZTE MRI image (Figure 1) shows the sensitive detection zone of the microprobe (volume evaluated to 500 nL).

Conclusion:

The MRS/MRI results obtained in vitro and in vivo illustrate the relevance of the microcoil design in respect of spectral resolution, detection sensitivity, spatial selectivity and limited invasiveness. Foreseen applications include the investigation of metabolism in submicroliter volumes.

Fig. 1. Left: implantable twisted microcoil with 150 µm copper wire and a total length of 3 mm. Right: MRI image obtained with the microcoil, illustrating the sensitive detection zone of the NMR probe.

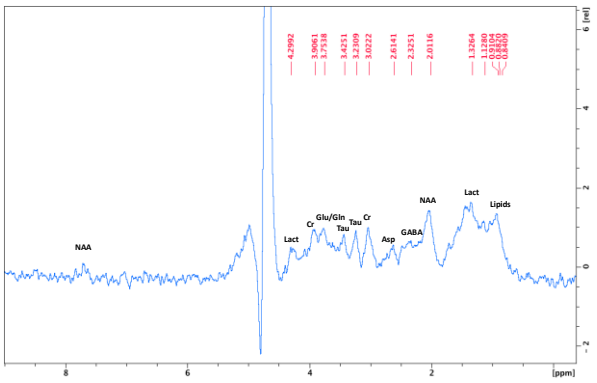

Fig. 2: NMR spectrum acquired at 7 Tesla in the rat brain using a PRESS sequence with water suppression. Total acquisition time is 10 minutes.

3D MR Microscopy with 6D Diffusion-Relaxation Distributions

L. W. Thrane[1], *H. Jiang*[1], *D. Topgaard*[1]
[1]Department of Chemistry, Lund University, Lund, Sweden

Introduction: In traditional magnetic resonance imaging (MRI) each imaging voxel contains voxel-averaged information about the chemical composition and translational motion of the spins. However, each voxel is typically comprised of multiple microscopic domains with different chemical and diffusion properties that can be probed by multidimensional relaxation rate and diffusion tensor correlation experiments [1]. The ability to probe microscopic domains within a voxel is of particular interest in investigations of various heterogeneous materials such as animal meat and biological tissue where each voxel can contain various chemical and structural properties.

Methods: Here, we introduce a 6D diffusion relaxation correlation MRI sequence which encodes the signal in a 6D sampling space of echo time TE, recovery time TR, the magnitude b, anisotropy b_Δ, and orientation (Θ,Φ). An inversion of the signal results in distributions in the 6D space of R_1, R_2, isotropic diffusion D_{iso}, diffusion anisotropy D_Δ, and diffusion tensor orientation (θ,φ), which combined gives the intra-voxel heterogeneity. Implementation of the pulse sequence was done on a Bruker 11.7 T microimaging system with in-plane spatial resolution of 0.3x0.3 mm^2 and slice thickness of 0.6 mm. The signal inversion is performed with our unregularized free inversion algorithm [1, 2] and the 6 physical parameters from the inversion are reported in correlation maps.

Results and Discussion: The pulse sequence used to execute the signal encoding is shown in Fig. 1 and is a diffusion-weighted spin echo RARE where the trapezoidal gradient pulses have been replaced by free gradient waveforms. Experiments were performed and validated on materials with known diffusion and relaxation properties.

Conclusion: The results show great potential for identifying intra-voxel chemical and structural micro-environments in various heterogeneous materials indicating also the potential for detecting microscopic changes occurring in the material.

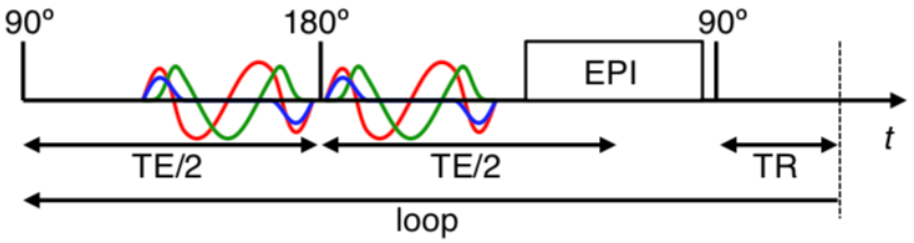

Fig. 1: Multidimensional diffusion-relaxation correlation pulse sequence. The 90° and 180° slice selective rf pulses produce an echo at the center of the RARE read gradient. The recovery time TR and echo time TE encode for R_1 and R_2 relaxation. The b-tensor encoding, consisting of the magnitude b, anisotropy b_Δ, and orientation (Θ,Φ), allows control of the size, shape, and orientation (isotropic diffusion D_{iso}, diffusion anisotropy D_Δ, and diffusion tensor orientation (θ,φ), respectively) of the diffusion encoding tensor by adjusting the free gradient waveforms on either side of the 180° pulse. The final 90° pulse, along with a crusher gradient (not shown) null the magnetization of the slice.

References: [1] Martins, Sci. Rep. (2018). [2] Martins, Phys. Rev. (2016).

Spatial encoding magnetic resonance imaging using quadratic gradients

S. Marhabaie, G. Bodenhausen, and P. Pelupessy
École normale supérieure, Paris, France

Abstract: In spatial encoding methods imparting a quadratic phase onto the transverse magnetization is the first crucial step. This is usually achieved by simultaneous application of a frequency-swept (chirp) pulse and a linear magnetic field gradient. In this work we show how a quadratic gradient can be used for spatial encoding MRI.

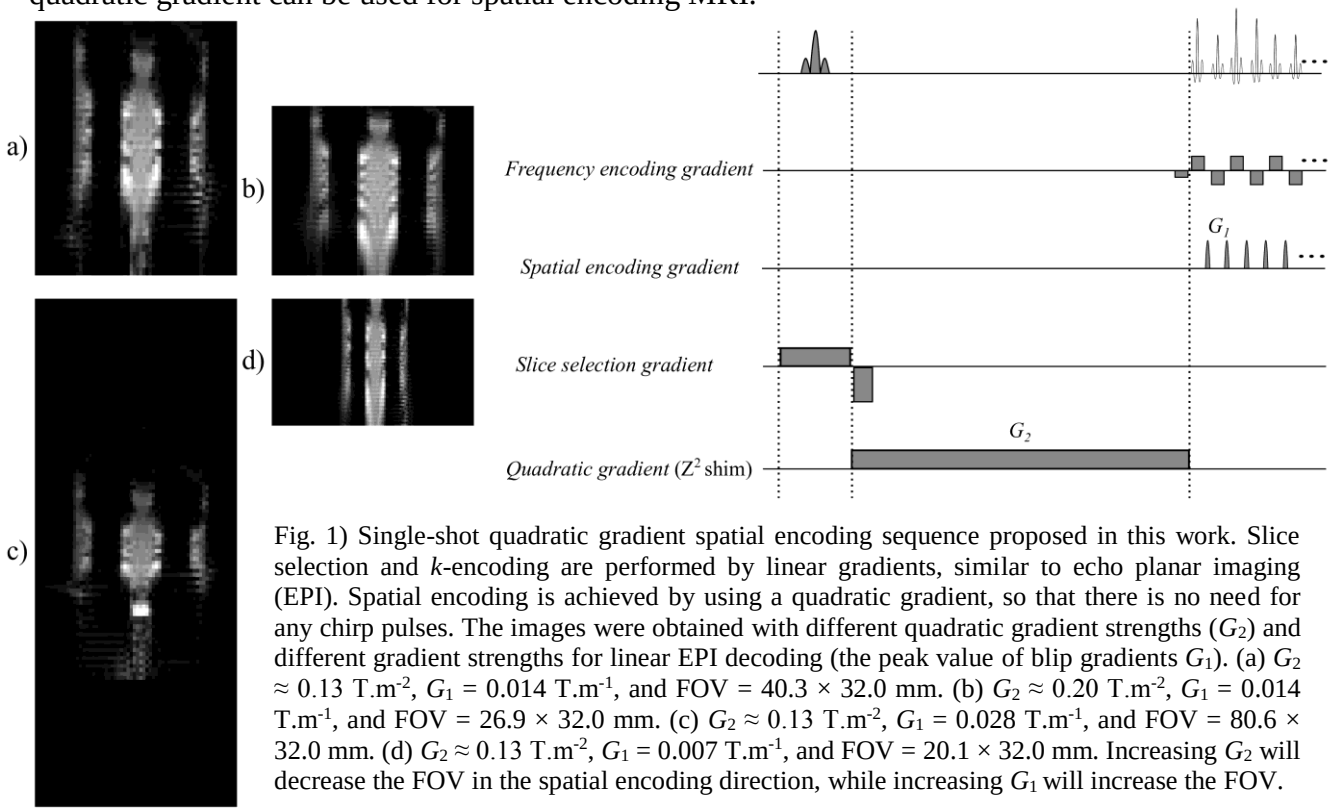

Fig. 1) Single-shot quadratic gradient spatial encoding sequence proposed in this work. Slice selection and *k*-encoding are performed by linear gradients, similar to echo planar imaging (EPI). Spatial encoding is achieved by using a quadratic gradient, so that there is no need for any chirp pulses. The images were obtained with different quadratic gradient strengths (G_2) and different gradient strengths for linear EPI decoding (the peak value of blip gradients G_1). (a) $G_2 \approx 0.13$ T.m^{-2}, $G_1 = 0.014$ T.m^{-1}, and FOV = 40.3 × 32.0 mm. (b) $G_2 \approx 0.20$ T.m^{-2}, $G_1 = 0.014$ T.m^{-1}, and FOV = 26.9 × 32.0 mm. (c) $G_2 \approx 0.13$ T.m^{-2}, $G_1 = 0.028$ T.m^{-1}, and FOV = 80.6 × 32.0 mm. (d) $G_2 \approx 0.13$ T.m^{-2}, $G_1 = 0.007$ T.m^{-1}, and FOV = 20.1 × 32.0 mm. Increasing G_2 will decrease the FOV in the spatial encoding direction, while increasing G_1 will increase the FOV.

Introduction: Non-Fourier MRI techniques like spatial encoding methods [1,2] do not need a Fourier transformation to produce an image. In spatial encoding, a quadratic phase can be imparted onto the magnetization by simultaneous application of a linear gradient and a frequency-swept pulse. This method suffers from some drawbacks like large specific absorption ratios (SARs), difficulties in performing multiple slice experiments, and long echo times (TEs). These limitations can be circumvented by using quadratic gradients.

Methods: The experiments have been performed on a plastic phantom using an 800 MHz Bruker NMR spectrometer. The pulse programs were written and implemented using the Paravision program, and the data were processed by a home-written Python code.

Results and discussion: Four single-shot images obtained with the proposed sequence are shown in Fig. 1. The quadratic gradient is stronger in Fig. 1(b) than in Fig. 1(a), so that the FOV is reduced, and the resolution is improved. The strength of the quadratic gradients are the same in Figs. 1(d), 1(a), and 1(c), but the strengths of the decoding gradients are stepwise increased, so that their FOVs are also increased. These observations prove the validity of this method. The absence of aliasing (when the object is larger than FOV), the variation of the FOV and of the resolution with the strength of the quadratic gradient are clear indications that our images are indeed spatially encoded.

Conclusion: The proposed quadratic gradient method avoids chirp pulses so that one can achieve much smaller SARs and shorter TEs. Furthermore, it is better adapted for multiple slice applications.

References: [1] Pipe, Magn. Reson. Med. (1995). [2] Shrot and Frydman, J. Magn. Reson. (2005).

Wine Cork Evolution during Aging: Insights from MRI Measurements

Jeffrey H. Walton[1], *Annegret Cantu*[1], *Michael Mackay*[2], *Greg Hirson*[3], *Andrew L. Waterhouse*[1]
[1]University of California, Davis, CA, USA, [2]University of Delaware, Newark, DE, USA, [3] Cork Supply, Benicia, CA, USA

Introduction: Wine aging is dictated by oxygen transport through the cork and natural cork is a nanostructured material with multiple pathways for oxygen transport. Imperfections in cork result mainly from crushed cell walls with defect concentration being the largest variable in wine cork structure and thus an influence in proper wine aging.

Methods: Intact corks were cut off of the bottle with a tile saw. Wine was poured into the wet side and stoppered with a cork. Care was taken to exclude bubbles. The cork/glass/wine/stopper assemblies were placed in the MRI system (Bruker Biospec 7T) such that the wine cork interface was approximately on isocenter. Microgradients (max gradient 950 mT/m) were used with the standard 35 mm inner diameter mouse volume coil. Both FLASH (TE=3ms, 256X128 pixels, FOV=40mm, slice=0.7mm) and multislice multiecho (TE=10ms, 256X256 pixels, FOV = 40mm, slice=0.2mm) data was taken. Cork has a very short T_2 and thus wine is bright and cork is dark in the images.

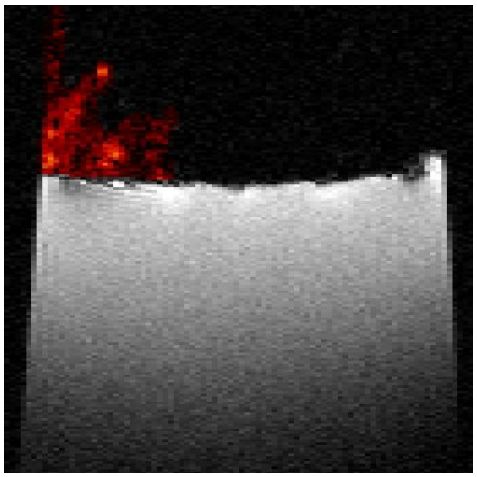

Figure 1. Flash Transverse Image showing wine penetration into the cork in red.

Results and discussion: Images are shown in Figures 1 and 2. Oxygen diffusion is 10,000 times slower through water than air thus slowing down oxygen transfer in the cork. During wine storage water also penetrates further into the cork and causes the cork to deteriorate with prolonged contact. We hypothesize that a combination of defects, plasmodesmata, water penetration into the defects, and wine-cork contact time during storage dictates the corks oxygen transmission rate. In our ongoing research we are measuring liquid penetration into corks with MRI measurements. Moreover, we can see how the water from the wine affects these defects during storage.

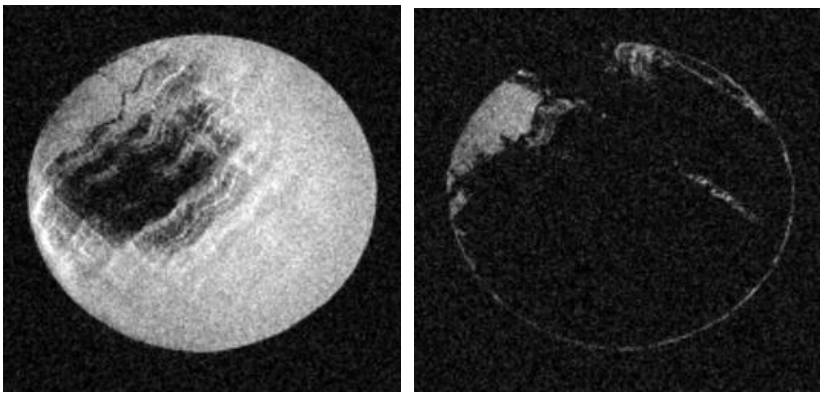

Figure 2. Two slices from the same cork. Left is at the wine-cork interface. Right is 3 mm inside the cork. Note that wine penetration into the cork follows a definite path presumably a path where cork cells are damaged.

Conclusion: MRI technology is a helpful tool to elucidate how wine contact affects natural cork closure performance to better understand how natural corks preserve wine quality.

Acknowledgements: The authors gratefully acknowledge Cork Supply, G3 Enterprises, Cade Winery (Plumpjack Group), J. Lohr Winery, and Silver Oak Winery for contributing samples and materials to the study.

Temperature dependence of T_2 relaxation times in fresh tomato pericarp

Rodolphe Leforestier, Maja Musse, François Mariette
IRSTEA, UR OPAALE, Rennes, France; Université Bretagne Loire, France

Introduction: Quantitative MRI can be used to investigate structural organization and dynamics of water in a non-invasive way [1]. It allows spatially resolved measurements of multi-exponential transversal relaxation times [2], making possible to access information on the status and distribution of water at a sub-cellular level. However, the variations of the relaxation signal occurring during physical processes such as drying or heating/cooling remains complex and only partially understood [3], in view of different tissue characteristics impacting relaxation mechanisms that are subject to modification. These relaxation mechanisms include chemical exchange of proton and diffusive exchange of water molecule between adjacent water compartments, and both will have an effect on each relaxing component but also on the multi-exponential distribution of the spectra. The objective of our study was to investigate the specific effects of temperature on the multi-exponential relaxation time T_2 distribution and water diffusion coefficient in the tomato.

Material and Methods: T_2 and apparent diffusion coefficient (ADC) measurements were performed on 4 ripe tomatoes with a Siemens Avanto 1.5T whole body scanner equipped with a temperature regulation device. The 5-mm median plane of fruits was acquired with a pixel resolution of 1.2^2 mm² at T = 5, 15, 25 and 35°C. T_2 was measured with a MSE sequence with 256 echoes, TE = 6.5 ms and TR = 20 ms. ADC was obtained from the PFGSE sequence with TE = 91 ms, TR = 5 s, Δ = 60 ms; δ = 20 ms and 8 b values ranging from 0 to 1197 s.mm^{-2}. The same experiments were repeated on the juice, extracted from the pericarp tissue of the tomatoes analyzed.

Results and discussion: T_2 relaxation decay computed on the pericarp has been described by a 3-exponential model with T_{21}~ 50 ms/ I_{01}~3 %; T_{22}~330 ms/ I_{02}~25 %; T_{23}~710 ms/ I_{03}~72 %, at 15 °C, corresponding respectively to water protons from cell wall, cytoplasm and vacuole. The total signal intensity varied linearly with the temperature according to the Curie law. Contrary to what had been expected, T_{21} and T_{23} remained stable, while ln(T_{22}) slightly increased with 1/T. In the case of the juice, ln(T_2) decreased linearly with 1/T, as expected from an Arrhenius model. Both tomato and extracted juice showed expected linear decrease of ln(ADC) with 1/T. Differences in temperature dependence of T_2 measured in fresh tomato pericarp and extracted juice indicated that modifications in diffusive exchanges between different cell compartments are at the origin of the unexpected T_2 behavior in the tomato pericarp, probably due both to changes in permeability of cell membranes and increase in ADC of different water fractions. This hypothesis is supported by the differences in relative signal intensities of the 3-exponential signal observed for different temperatures. The impact of chemical exchanges between water protons and exchangeable protons of different carbohydrates and acids present in the tomato did not lead to a non-linear relationship between ln(T_2) and 1/T, as demonstrated on the juice. The latter was consistent with its relatively low pH of about 5, according to [4], indeed at this pH, the exchange rate is too fast compared to the echo time to modulate the relaxation .

Conclusion: The complex dependence of the multi-exponential transverse relaxation signal on temperature measured in intact tomato tissues has been interpreted by taking into account the chemical proton exchange between water and cell metabolites and the diffusional exchanges of water molecules between cell compartments. The relaxation signal has been shown to be especially sensitive to the latter phenomenon.

References: [1] Snaar, Biophys. J (1992). [2] Adriaensen, Magn. Reson. Imaging (2013). [3] Hills, Appl. Magn. Reson. (1999). [4] Hills, J. Chem. Soc. (1990).

Site-resolved distribution and molecular dynamics of water within fibril aggregates: from plant cell-wall scale to atomistic resolution.

C. Terenzi[a], *P. Chen*[b], *J. Wohlert*[b], *L.A. Berglund*[b], *I. Furó*[b]

[a]Wageningen University, Wageningen, The Netherlands, [b]WWSC and KTH, Stockholm, Sweden

Introduction: Natural or synthetic functional polymers, such as those based on cellulose nanofibers (CNFs), exhibit strongly heterogeneous structures, with highly crystalline cores surrounded by non-crystalline surface polymers and less ordered domains, that react differently to the ingress of moisture or to chemical treatments. This heterogeneity is carried over to synthetic composites, whose structure-function relationship depends in a complex way on the amount, and spatial localization, of moisture. Describing polymer-water interactions quantitatively and with high spatial and chemical resolution is, thus, vital when designing new functional materials with finely-tuned properties. To probe spatial scales from sub-µm down to sub-nm, we have successfully combined high-field (7 T and 11.7 T) static and MAS multi-nuclear NMR spectroscopy and relaxometry with numerical spectral modelling or molecular dynamics (MD) simulations of ^{13}C NMR T_1 data.

Methods:

1. ^{1}H spectroscopy of hydrated Norway spruce wood with its radial (R), tangential (T) or longitudinal (L) directions along the magnetic field, and spectral simulations in MATLAB. [1]
2. Static ^{2}H T_2 relaxometry of hydrated CNFs, xyloglucan (XG), and their composite (CNF/XG [2,3], and ^{2}H MAS spectroscopy of cellulose hydrated in $^{2}H_2O$.[4]
3. Site-specific CP-MAS ^{13}C T_1 relaxometry in CNFs, XG and CNF/XG, and their MD simulations.[2,5,6]

Results and discussion:

1. The inhomogeneous spectral broadening for spectra of *mobile* water recorded with field along the T- and R-directions was explained in terms of structural heterogeneities on length scales > 100 nm.[1]
2. *Surface* or *bulk-like* $^{2}H_2O$ distributions could be detected in CNF and XG, respectively, and quantified in the CNF/XG composite.[2,3] By ^{2}H MAS spectra of cellulose, *immobile* and *mobile* surface water could be further assigned to *intra-* and *inter*-aggregate domains.[4]
3. Broad ^{13}C CP-MAS T_1 distributions (Fig.1), and their evolution with moisture content, unraveled faster polymer dynamics in XG as compared to CNF, especially at non-crystalline/less ordered carbon sites. Dynamical heterogeneity within spectrally overlapping sites was further resolved by MD simulations, that could also directly correlate ^{13}C T_1 values with local water densities.[2,5,6]

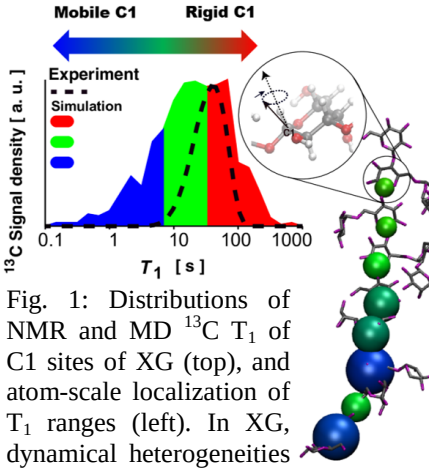

Fig. 1: Distributions of NMR and MD ^{13}C T_1 of C1 sites of XG (top), and atom-scale localization of T_1 ranges (left). In XG, dynamical heterogeneities are more averaged out at the long NMR time scale (seconds) than over the short MD trajectories (50 ns).[5]

Conclusion: ^{2}H and ^{13}C NMR spectroscopy and relaxometry constitute a powerful tool to selectively investigate spatial heterogeneities in hydrated soft bio-materials. When combined with MD simulations, atomistic-level resolution can be achieved that provides unprecedented insight from NMR data.

References: [1] Terenzi et al, Phys. Chem. B. (2013). [2] Terenzi et al, Biomacromolecules (2015). [3] Prakobna et al, Carb. Polym. (2015). [4] Lindh et al, PCCP (2016). [5] Chen et al, Biomacromolecules (2018). [6] Chen et al, Submitted to Macromolecules (2019).

" Using biological magnetization as a tool for bacterial imaging"

Our understanding of the dynamic interplay between bacteria and their mammalian hosts would benefit tremendously from noninvasive imaging techniques that can specifically detect bacteria in complex ecosystems. This study develops such techniques to detect image bacteria using magnetic resonance imaging. Our approach involves labeling bacteria with macromolecular assemblies that are engineered for cell selectivity and loading them with contrast agents detectable using noninvasive modalities such as MRI. In preliminary *in cellulo* experiments, we have established the feasibility of this approach by specifically distinguishing distinct bacterial strains using MRI.

In-situ NMR highlights structural change during apple heating

Sylvie Clerjon[a], Alexandre Leca[b], Catherine Renard[b], Jean-Marie Bonny[a] and Amidou Traore[a]
[a]AgroResonance, UR370 QuaPA - INRA, 63122 Saint-Genès-Champanelle, France
[b] SQPOV, INRA, 84914, Avignon, France

Introduction: Microstructure and texture evolution of foods during cooking is difficult to achieve, because conventional techniques cannot analyze the internal structure, while preserving its integrity. For this very often-processed product that is apple, it is essential to understand thermal degradations. To study such phenomena, we undertook in-situ quantitative NMR during the cooking process.

Methods: Five Golden Delicious apples were sampled in four 10 mm long and 5 mm diameter cylinders. Each of the twenty samples was sealed in parafilm. The thermal treatments were performed *in situ* in a 9.4 T Bruker Ascend 400WB instrument. A 5-mm diameter microimaging birdcage radiofrequency coil was used for both excitation and signal reception. A controlled hot air flow cooked the sample from 20 to 60°C in 70 min.
Non-spatially resolved (spectroscopy) T2 measurements were performed with a Carr-Purcell-Meiboom-Gill (CPMG) pulse sequence [1], with the interpulse delay τ of 125 microseconds. The repetition time was set to 5 seconds for a total acquisition duration of 2min30s.
Assuming that the T2 decay curve stands as a sum of weighted exponential decays describing the complexity of the internal structure of the sample:

$$S = \sum_{j=1}^{m} A_j e^{\left(-t_i / T_{2j}\right)} \qquad i=1, 2 \ldots .n$$

each decay curve was analyzed with an in-house Matlab® implementation of the non-negative least squares (NNLS) algorithm [2].

Results and discussion:
As an illustration, this figure shows T2 change with cooking temperature for one of our sample. A shift in T2 value of the main water fraction is between 50 and 53°C (arrow). This critical temperature is in accordance with mechanical properties changes measured on samples cooked at various temperature.

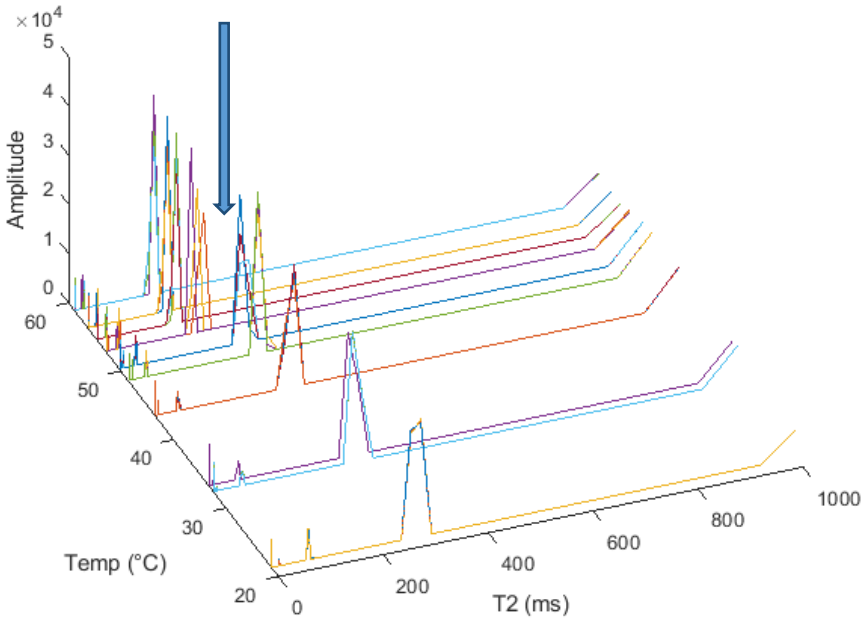

Conclusion: This study points out the feasibility of resolving multiexponential T2 decay, at high magnetic field, during apple sample cooking. It provides longitudinal information about structure change and water redistribution on a same sample during the whole process.

References: [1] Meiboom, S. and D. Gill, Rev. Sci. Instrum. (1958).
[2] Istratov, A. A. and O. F. Vyvenko, Rev. Sci. Instrum. (1999).

Nuclear Magnetic Resonance Multi-Phase Flowmeter & Fluid Analyzer

F. Deng[1], S.W. Chen[1], G.H. Chen[1], H.B. Liu[2], L.Z. Xiao[3]

[1]Petrochina Research Institute of Petroleum Exploration & Development, China National Petroleum Corporation, Beijing, China, [2]Beijing Limecho Technology Limited Company, Beijing, China, [3]State Key Laboratory of Petroleum Resources and Prospecting, China University of Petroleum, Beijing, China

Introduction:

Quantitative information regarding multi-phase flow of oil, gas & water in wells or pipelines are very important in continuous well performance monitoring, production optimization, flow assurance, well testing, production allocation, etc. So far, the multi-phase flow measurement methods are usually with low-efficiency, low-accuracy, high-costs and delay-delivery, and hard to reflect the real instantaneous fluid producing properties at wellheads or pipelines. Therefore, it is urgent to seek for accurate and reliable multi-phase flow detection devices and methods that can meet the monitoring demands of unconventional oil and gas resources.

Methods:

Proposed a set of nuclear magnetic resonance (NMR) multi-phase fluid analytical methods & device. The flowing NMR data acquisition, processing and interpretation methods are proposed to fill the blank of traditional methods. The full bore, straight tube design does not restrict the flow line and eliminates wear of internal parts and pressure drops, the Halbach magnet structure are designed to provide a homogeneous magnetic field inside the bore while cancelling the magnetic field outside the housing of the device, the separate antenna structure are designed to eliminate the flow effects on NMR measurement, the application of integration of measurement and control technology realize unmanned operation.

Results:

This progress helps to apply the NMR technology to oil & gas production industry, to realize green, efficient, online, low cost, full range multi-phase fluid measurements. The on-site fluid properties analysis capability moved the laboratory test to the oil & gas fields, improved efficiency, accuracy and reduce costs.

Conclusion:

As a flowmeter, the device reduces the amount of measuring equipment needed and manage wells more efficiently, as a ‘fluid analysis laboratory’, can provide the first-hand information on the oil/gas properties.

References: [1] F. Deng, L.Z. Xiao, H.B. Liu, et al, Appl Magn Reson. (2013). [2] M. Appel, J.J. Freeman,SPE 141465. (2011).

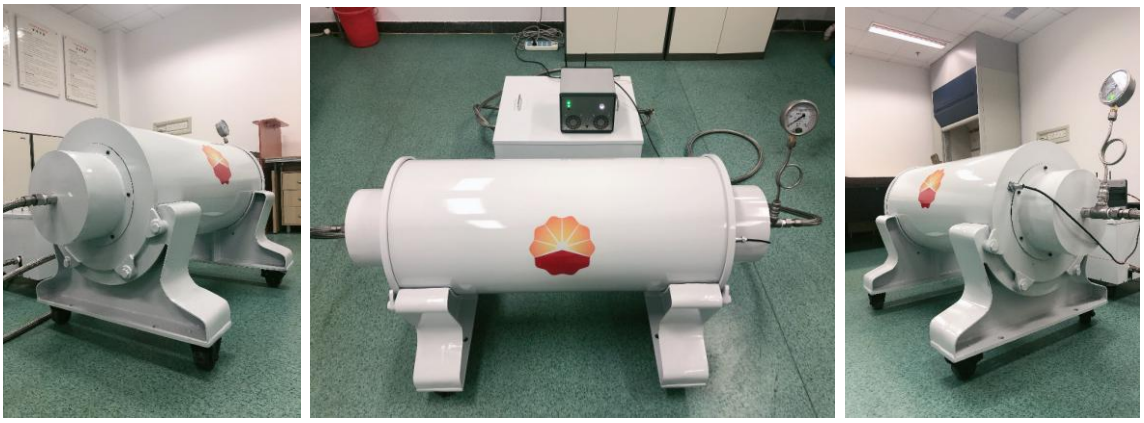

Fig. 1: The photo of NMR multi-phase flowmeter & fluid analyzer.

Deposit layer formation during protein filtration by 1D inverse Abel-transformation MRI

N.Schork[1], S.Schuhmann[1], D.Gross[2], H.Nirschl[1], G.Guthausen[1,3]
[1]Institute of Mechanical Process Engineering and Mechanics, KIT, 76131 Karlsruhe, Germany
[2]Bruker BioSpin MRI GmbH, 76287 Rheinstetten, Germany
[3]EBI, Chair of Water Chemistry and Water Technology, KIT, 76131 Karlsruhe, Germany

Introduction: Skim milk protein separation aims for the separation of the casein proteins (d = 50 - 400 nm) from the smaller whey proteins (d = 3 - 4 nm). A deposit is formed on the inside of the hollow fiber membranes. With filtration time, the permeating mass flow and consequently the whey protein throughput declines rapidly. This decrease in separation efficiency requires a costly back-washing or chemical cleaning of the hollow fiber membranes. Because the details of the spatially and time-dependent deposit formation are not fully understood, time-resolved structural MR imaging of the deposit layer formation can be measured by conventional MRI methods [1, 2]. An alternative is 1D MRI with subsequent inverse Abel transformation [3, 4].

Methods: Typical MRI experiments, such as diffusion-weighted imaging require long measurement times. 1D projection MRI was utilized to detect the deposit formation of milk proteins and diffusion in the deposit. To observe and extract quantitative information of the time-dependent filtration process, alternative forms of dedicated image data transformation and subsequently processing algorithms were explored. In a first approximation, the cylindrical hollow fiber membrane and the filtration module are rotationally symmetric. Consequently, an inverse Abel-transformation of 1D projections was utilized. For the reconstruction of the image space from the projection, an algorithm with a Gaussian basis-set expansion was implemented [5, 6]. Apart from relaxation- and spin density- weighted imaging, spatially resolved diffusion coefficients were measured.

Results and discussion: Conventional 2D data acquisition is compared with 1D inverse Abel transformation. Via diffusion-weighted imaging, the apparent water self-diffusion coefficients are quantified. Apparent water self-diffusion coefficients are explored to describe the deposit formation during the filtration process and address questions of protein concentration in the deposit.

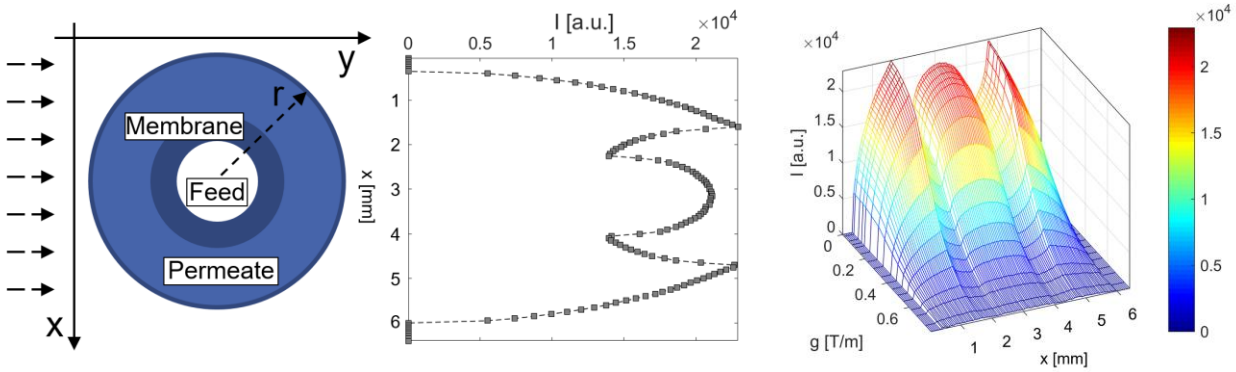

Fig. 1: The filtration setup is approximately rotationally symmetric (left) and is measured by 1D projection experiments (middle). Diffusion weighted projections reveal spatially resolved diffusion coefficients (right).

References:

[1] Schuhmann et al., Aiche Journal 64(11), 4039–4046, 2018. DOI: 10.1016/j.memsci.2018.10.072
[2] Schork et al., Magn. Reson. Chem., *in press*, 1-11, 2019. DOI: 10.1002/mrc.4826
[3] Meininger et al., Journal of Magnetic Resonance 125(2): 325-331, 1997. DOI: 10.1006/jmre.1997.1124
[4] Hollingsworth et al., Journal of Magnetic Resonance 176(1): 71-78, 2005. DOI: 0.1016/j.jmr.2005.05.019
[5] Garcia et al., Review of Scientific Instruments 75(11), 4989-4996, 2002. DOI: 10.1063/1.1807578
[6] Dribinski, et al. Review of Scientific Instruments 73(7): 2634-2642, 2002. DOI: 10.1063/1.1482156

Deposit layer formation during skim milk protein filtration by MRI

N.Schork[1], S.Schuhmann[1], E.Amling[1], H.Nirschl[1], G.Guthausen[1,2]
[1]Institute of Mechanical Process Engineering and Mechanics, KIT, 76131 Karlsruhe, Germany
[2]EBI, Chair of Water Chemistry and Water Technology, KIT, 76131 Karlsruhe, Germany

Introduction: Skim milk protein separation by membrane processes has a high market share in the food-processing sector. An advantage of applying a membrane filtration process instead of separation processes is that the proteins remain in their native state and therefore maintain their nutritional value and functionalization. During the separation of the major casein proteins (d = 50 - 400 nm) from the smaller whey protein fraction (d = 3 - 4 nm), a deposit is formed on the inside of hollow fiber or multi-channel membranes. With filtration time, the permeating mass flow and consequently the whey protein throughput declines rapidly. Because the details of the deposit formation and impact on filtration efficiency are not fully understood, time and spatially-resolved structural MR images of the deposit layer formation was measured [1,2].

Methods: The properties of the skim milk are known to be dependent on temperature, pressure, pH, shear and velocity forces, among others. Therefore, filtration and deposit formation depend on those parameters. The process temperature and feed pressure were varied to observe the protein accumulation on the membrane surface. During the *in situ* filtration, the milk protein's deposit formation on the inside of the hollow fiber membrane was detected by RARE MRI. The image contrast of the protein deposit was enhanced by chemically compatible superparamagnetic nanoparticles as MRI contrast agents. Dedicated image analysis with radial averaging was applied afterwards. To investigate the nature of the deposit, the signal intensity distribution in the membrane lumen was quantified and analyzed in detail. The question of the deposit's reversibility was also addressed and measured by MRI.

Results and discussion: The detailed description of the deposit layer formation and its reversibility allow an evaluation of the structure and nature of the deposit and its dependence on the process parameters such as pressure and temperature. By applying a model to the radial signal intensity distribution, the deposit layer could be further characterized. The deposit consists of two regions that behave differently during filtration and reversibility experiments.

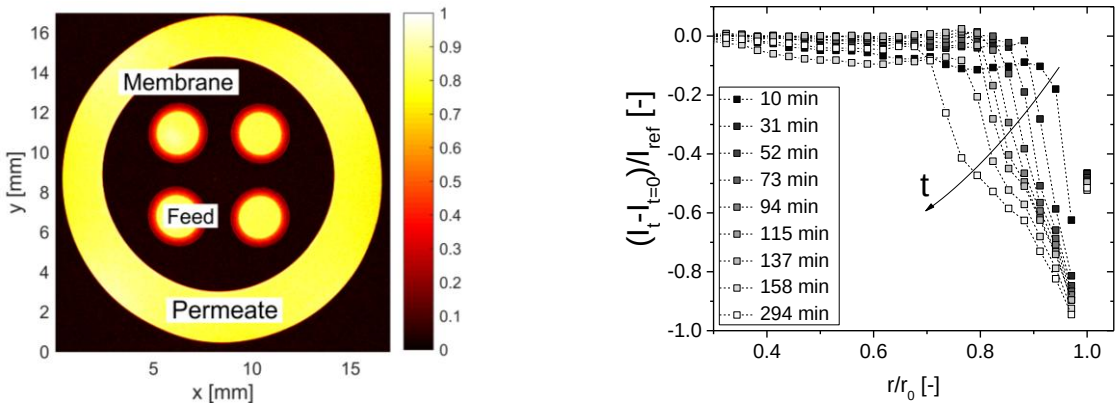

Fig. 1: Skim milk filtration in a four-channel ceramic membrane at the end of a dead-end filtration for about t = 5 h (left) and radial signal intensity distribution as a function of radius in one of the channels (right).

References:

[1] Schuhmann et al., Aiche Journal 64(11), 4039–4046 (2018), DOI: 10.1016/j.memsci.2018.10.072
[2] Schork et al., Magn. Reson. Chem., *in press*, 1-11, (2019), DOI: 10.1002/mrc.4826

A low-cost, miniature Halbach magnet with adjustable homogeneity designed for accurate and immediate detection of blood glucose

Qing Yang[a], *Yi Chen*[a], *Rongsheng Lu*[a*] , *Zhonghua Ni*[a], *Hong Yi*[a]
[a]School of Mechanical Engineering, Southeast University, Nanjing, China
*Corresponding author: Rongsheng Lu, lurs@seu.edu.cn

Point of care detection of blood glucose concentration is of great significance for diabetes control. Glucose oxidase can react with glucose and form hydrogen peroxide which can convert Fe^{2+}toFe^{3+}. Fe^{2+} and Fe^{3+} will alter the relaxation rate of water solution with different speed, which result in the change of T_1. Based on this principle, accurate detection of blood glucose can be achieved by NMR device. However, state-of-the-art NMR devices are almost based on superconducting magnets or permanent magnets with a large size, which limit the NMR apparatus for the point of care detection of blood glucose. With the development of integrated circuits, probes and RF transceivers both are moving toward miniaturization. Therefore, a small magnet with high field strength and uniform magnetic field is the key to reduce the volume and the cost of the instrument. Since the Halbach magnet has the largest field strength-mass ratio among all types of magnets, it has always been the research focus of portable NMR. However, in order to achieve desired magnetic field performance, the components of traditional Halbach magnet should be manufactured and assembled with high precision up to 1um. In fact, the performance of actual magnet is significantly different from the designed magnet. To solve this problem, we propose a Halbach magnet structure with adjustable magnetic field homogeneity by using a shimming module. The magnet is composed of three main parts, including the main magnet made of SmCo32 which can produce dipolar magnetic field up to 1T, twenty magnetic strips made of N52 which can improve the magnetic field strength at the end of magnet, and a shimming module fixed in the center of magnet which is able to improve the magnetic field homogeneity accurately after machining. The shimming module can fix the small shimming magnets made of SmCo18 with a thickness of only 0.2mm. Then the parameters of the designed magnet are optimized based on the electromagnetic field finite element method. Besides, in the process of magnet parameter optimization analysis, the key error factor affecting the performance of magnet is obtained by introducing the machining error generated in the magnet processing—magnetization angle. Theoretically, the magnetic field uniformity of a cylindrical volume of 5 mm in diameter and 5 mm in length will rise from 30 ppm to 4200 ppm under the condition of maximum magnet machining error. However, by adjusting the position of the shimming magnets at the center of the magnet, the homogeneity value can be reduced to less than 100ppm. A better magnetic field homogeneity less than 40 ppm can be completed forward by using a shimming module. In the end, the size of the magnet designed in this paper is$\emptyset 64 \times 132mm^3$, and the weight is only 2.5kg, which can meet the requirements of portable and low-cost micro-NMR apparatus for point of care detection of blood glucose.

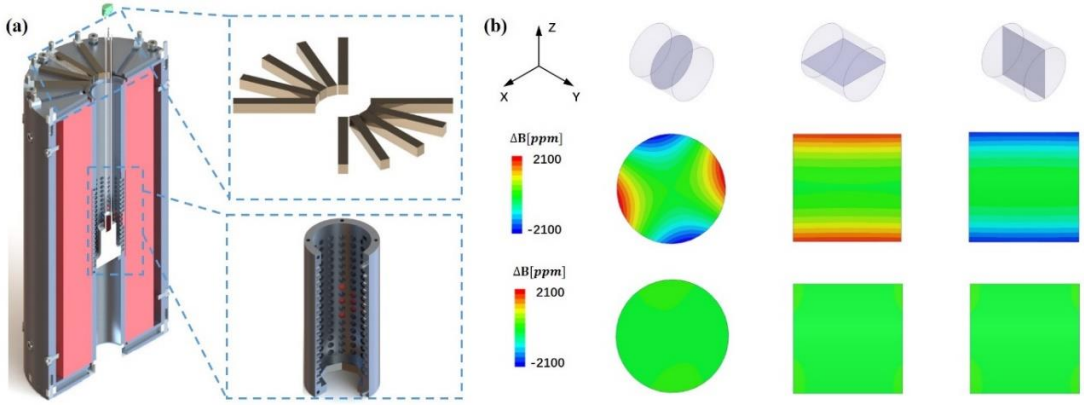

Fig. 1: A low-cost miniature Halbach magnet with adjustable homogeneity (a) schematic diagram of the magnet, the above inset is magnetic strips, the lower is shimming module; (b) 2D maps of magnetic field, the middle is before shimming and the lower is after shimming.

Passive radiofrequency shimming for rat head imaging at 17.2 Tesla

M. Dubois[1,2], *T.S. Vergara Gomez*[1,2], *C. Jouvaud*[3,4], *A. Ourir*[5], *J. De Rosny*[5], *F. Kober*[2], *R. Abdeddaim*[1], *S. Enoch*[1], *L. Ciobanu*[6]

[1]Aix Marseille Univ, CNRS, Centrale Marseille, Institut Fresnel, Marseille, France, [2]Aix Marseille Univ, CNRS, CRMBM, Marseille, France, [3]CEA-LETI MINATECH, Grenoble, France, [4]Université Grenoble Alpes, Grenoble, France, [5]ESPCI Paris, PSL Research University, CNRS, Institut Langevin, Paris, France, [6]CEA, DRF, JOLIOT, NeuroSpin, UNIRS, Université Paris-Saclay, Gif-sur-Yvette, France

Introduction: The Larmor frequency of proton reaches 730 MHz in a 17.2 T magnetic field intensity. This makes typical volume coil dimensions comparable with the electrical wavelength for sensitive volumes of a few centimeters cube. Consequently, the volume coils are much more sensitive to the sample loading and setting quadrature drive requires extra care depending on the sample [1]. Here we propose to start from a surface loop coil of 3 cm diameter and extend its sensitive volume by means of passive radiofrequency (RF) shimming [2,3]. We designed a metamaterial composed of four coupled metallic wires placed onto the floor of the MRI animal bed. The structure is able to extend the sensitive volume of the surface coil both in depth and in the longitudinal axis.

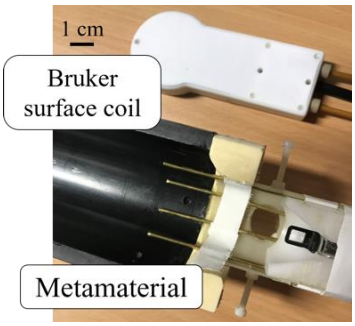

Fig.1: Experimental setup: 3 cm diameter surface coil (top) and 4 90 mm long brass rods placed onto the animal bed (bottom).

Methods: Electromagnetic simulations of the metamaterial and the surface loop coil were performed using CST Microwave Studio 2017. The metamaterial (four brass rods of 1 mm diameter and 90 mm length) and the surface loop coil are presented in Fig.1. A phantom tube containing NaCl solution and $CuSO_4$ was used for on-bench and *in vitro* characterization. All MRI experiments were performed on an animal scanner operating at 17.2 T (Bruker BioSpin, Germany). Actual Flip Angle Imaging (AFI) was used to obtain B_1^+ maps and SNR maps were obtained with a 2D Multi-Slice-Multi-Echo sequence (SE). *In vivo* measurements were performed with a 2D Rapid Imaging with Refocused Echoes (RARE) sequence on one anesthetized rat (Sprague Dawley).

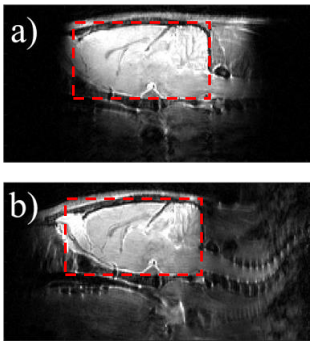

Fig. 2: *In vivo* images of a rat brain (sagittal slice) obtained with the surface coil alone (a) and with the metamaterial (b). FOV: 2.5x5 cm², resolution: (0.2 mm)², slice thickness: 0.5 mm

Results and discussion: The length of the metallic rods was chosen such that their impact on the surface coil detuning remained correctable via the coil's tuning and matching circuit [4]. Numerical results showed that although the resonant frequency of the metamaterials is much higher (>1 GHz) they provide enhancement of the sensitive volume in depth and along the longitudinal axis. This enhancement was observed experimentally on both the phantom and the animal as shown in Fig. 2. The *in vivo* acquisitions showed that 85% of the local signal corresponding to the loop alone is conserved in the region of interest (red dash) in the presence of the metamaterial while the in depth and the longitudinal sensitive volumes are increased.

Conclusion: We showed that the RF shimming approach is well suited for rat head imaging at high magnetic field intensity. The extension of the sensitive volume of the surface coil allows imaging of a large portion of the spinal cord while maintaining 85% of the initial signal in the brain area. The concept of combining metamaterials and commercial surface coils may help in the design of future coils for preclinical applications at ultra-high field. This project has received funding from the European Union's Horizon 2020 research and innovation program under grant agreement No 736937.

References: [1] Shajan et al, NMR in Biomed (2012). [2] Vaidya et al, Magn. Res. Med (2018). [3] Dubois et al, Phys. Rev. X (2018). [4] Vergara et al, NMR in Biomed (2018).

MRI and Localized NMR Spectroscopy of Sessile Droplets on Hydrophilic, Hydrophobic and Superhydrophobic Surfaces – Examination of the Chemical Composition of Sessile Droplets during Evaporation

J. Kind[a], *C. M. Thiele*[a]

[a] Clemens-Schöpf-Institut, Technische Universität Darmstadt, Darmstadt, Germany

Introduction: The investigation of sessile droplets on structured surfaces is currently a focus of research. The evaporation of such droplets depends not only on the boiling point and vapor pressure of the liquid, but also on the macro- and microscopic structure of the surface and its chemical composition.[1-2] The understanding of the droplet evaporation of homogeneous and heterogeneous substance mixtures is important, for example, to explain the formation of coffee stains or to optimize the results in offset printing.[3] Contact angles are usually measured with the aid of optical methods (e.g. drop shape analysis).[4] Such measurements can only provide indirect information on the composition of the droplet. For a detailed understanding of the evaporation of complex mixtures from structured surfaces, such as inks used in offset printing, a time-resolved analysis of the droplet composition is essential. Therefore, we demonstrate in this work that magnetic resonance methods can be used to a) image sessile droplets on structured surfaces and b) investigate their composition in a time-resolved manner.

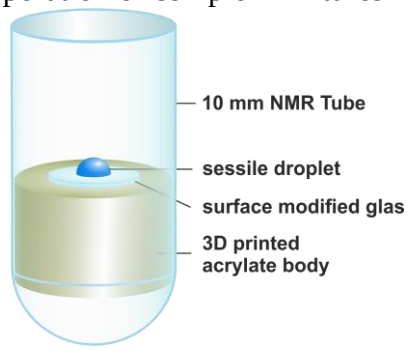

Fig. 1: Sample setup for examination of sessile droplets in 10 mm tubes.

Methods: Sessile droplets are examined on a 3D printed acrylate space modified with a glas surface (Fig. 1). By using chemically or physically modified glasses droplets with different contact angles can be examined with MRI experiments like FLASH[5] or RARE[6] as well as non-localised and localized NMR spectroscopy.

Results and Discussion: First it is shown that water droplets on superhydrophobic, hydrophobic and hydrophilic surfaces, despite the large liquid/gas interface, can be imaged well and without interfering artifacts using RARE (Fig. 2). Further, the signals are examined in PRESS[7] NMR spectra of water and 1-hexanol with respect to line shape and quantifiability. Finally, it is demonstrated that globally recorded NMR spectra can be used to track the droplet composition of a binary mixture (water/acetone) during evaporation.

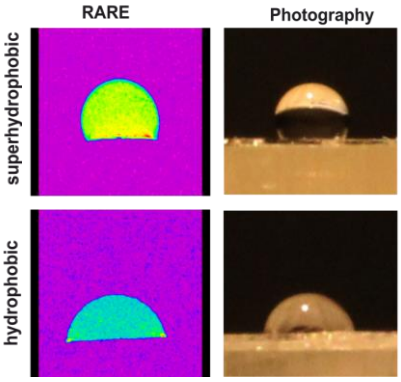

Fig. 2: RARE images as well as photo-graphies of water droplets on a a) superhydrophobic (silicon nanofilament), b) hydro-phobic (PFDTS, Perfuorodecyltrichloro-silane) surfaces.

Conclusion: MR techniques are valuable for the examination of sessile droplets on structured surfaces, as spectroscopic data allow to track the droplet composition during evaporation directly. With that, relations between surface properties and evaporation properties of sessile droplets can be examined. This might give a deeper understanding of complex drying processes as in offset printing.

References: [1] Bourges-Monnier *et al.*, *Langmuir* (1995) [2] Park, J. K. *et al.*, *Soft Matter* (2012) [3] Majumder, M. *et al.*; *J. Phys. Chem. B* (2012) [4] Neumann, A. W., Good, R. J., In *Surface and Colloid Science: Volume 11: Experimental Methods*, Good, R. J.; Stromberg, R. R., Eds. Springer US: Boston, MA, (1979) [5] Haase, A. *et al.*, *J. Mag. Reson.* (1986) [6] Hennig, J. *et al. Magnetic Resonance in Medicine* (1986), [7] Klose, U., *European Journal of Radiology* (2008)

Acknowledgement: This work was financially supported by the German Research Council (CRC 1194).The authors thank Melanie Britton for fruitfully discussions.

NMR relaxation and oxygen permeation studies on protein-sugar matrices conditioned at different humidities

Jens Meissner[a], *Nikolaus Nestle*[a], *Emma Thompson*[a], *Eduard Schreiner*[b], *Mireia Subinya Albrich*[a], *Fangfang Chu*[c]

[a] BASF SE Materials Physics, Analytics and Formulation, Ludwigshafen, Germany, [b] BASF SE Digitalization in Research and Development, Ludwigshafen, Germany,[c]BASF Nutrition and Health, Lampertheim, Germany

Introduction: Many food ingredients, including vitamins and other micronutrients, as well as aroma substances and pigments, are degraded over time by atmospheric oxygen. This significantly limits the shelf-life of many food and feed products, especially in powder formulations. In addition to the use of packaging materials offering a high oxygen barrier, the matrices used in the actual powder formulation can also contribute to reduced oxygen-induced degradation.
Many of these materials come with sufficiently low oxygen permeability in the dry state but, with increasing moisture content, the barrier properties deteriorate considerably. The present approach to study the oxygen permeation properties of such materials are permeation measurements on films conditioned at different humidities. This is a rather time-consuming approach and requires careful production of defect-free macroscopic films of the polymer mixtures to be studied.

Experiments and simulations: In order to gain insight into the impact of moisture on molecular dynamic inside matrix materials, NMR relaxation and molecular dynamics simulations, using LAMMPS, have been explored. By correlating molecular mobility to oxygen permeation rates, the need for time consuming oxygen permeation measurements can be reduced. (Furthermore, conclusions about the barrier properties of materials, which do not readily form a film, can be drawn.)

Correlations: In our contribution, we will present moisture dependent studies of NMR, permeation properties and simulation results for various matrices composed of proteins and sugars and discuss observed correlations and open questions. In the figure, an example is given for the correlations between simulated self-diffusion coefficients and measured T2-times of water in mixtures of gelatin and various sugars conditioned at different moisture levels. Due to the sensitivity of NMR relaxation times to processes on the time scale of simulations, relaxation times can play a key role in making the bridge between simulations and experiments in such systems.

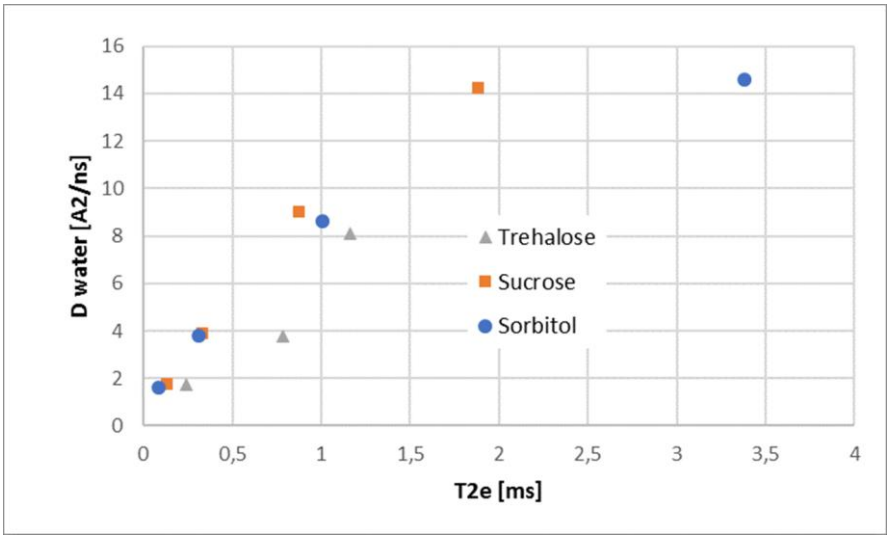

A solid echo T_1-T_2 method for enhancing hydrogen-containing solid NMR signal in hydrated cement paste

Zhengxiu Wu[a,b], *Xiaowen Jiang*[a,b], *Rongsheng Lu*[a,b,*], *Zhonghua Ni*[a,b], *Zonghai Xie*[a,b]

[a]Jiangsu Key Laboratory for Design and Manufacture of Micro-Nano Biomedical Instruments, Nanjing, China

[b]School of Mechanical Engineering, Southeast University, Nanjing, China

[*]corresponding author: Rongsheng Lu, lurs@seu.edu.cn

Low-field nuclear magnetic resonance (NMR) techniques have been widely used for continuously detecting hydrated cement paste due to the advantages of non-destructive and quantitative measurement. There are chemically combined solid crystalline phases such as calcium hydroxide and ettringite in hydrated cement paste. However, it is difficult to accurately measure hydrogen-containing solid signal in hydrated cement paste by traditional low-field NMR methods. In order to efficiently detect more signal of solid crystalline phases, IR combined solid echo train pulse sequence (solid echo T_1-T_2 method) was first employed to acquire two dimensional T_1-T_2 relaxation correlation signal of hydrated cement paste in this work. Experimental results indicate that solid echo T_1-T_2 relaxation measurement can gain more complete signal of solid crystalline phases in hydrated cement than conventional low-field NMR measurement. Fig. 1 shows the T_1-T_2 correlation maps of white cement with water to cement ratio of 0.4 for 7 days of hydration, Fig. 1(a) and Fig. 1(b) are the results measured by conventional T_1-T_2 method (IR combined CPMG pulse sequence) and solid echo T_1-T_2 method respectively. As shown in Fig. 1, the signal of the region 2 corresponds to the water in capillary pores and inter-C-S-H gel pores, the signal of the region 1 generated from highly bound water or solid crystalline phases. In region 1 of T_1-T_2 correlation maps, solid echo T_1-T_2 measurement method can discover additional peak, this peak location is far away from T_1-T_2 parity line with the ratio of $T_1/T_2 > 1000$, and the T_2 relaxation time is in the order of 30us. Therefore, the additional peak is mostly contributed by homonuclear dipolar coupling for isolated spin-1/2 pairs in solid crystalline phases such as calcium hydroxide, while this interaction cannot be refocused by CPMG pulse method. In addition, the signal intensity in region 1 acquired by solid echo T_1-T_2 method is approximately 48% higher than the conventional T_1-T_2 method. This component has a very short T_2 relaxation time and very high value of the ratio T_1/T_2. In conclusion, the solid echo T_1-T_2 measurement method can be efficiently used for the analysis of product composition on the hydration of cement, especially for the collection and analysis of complete solid NMR signals.

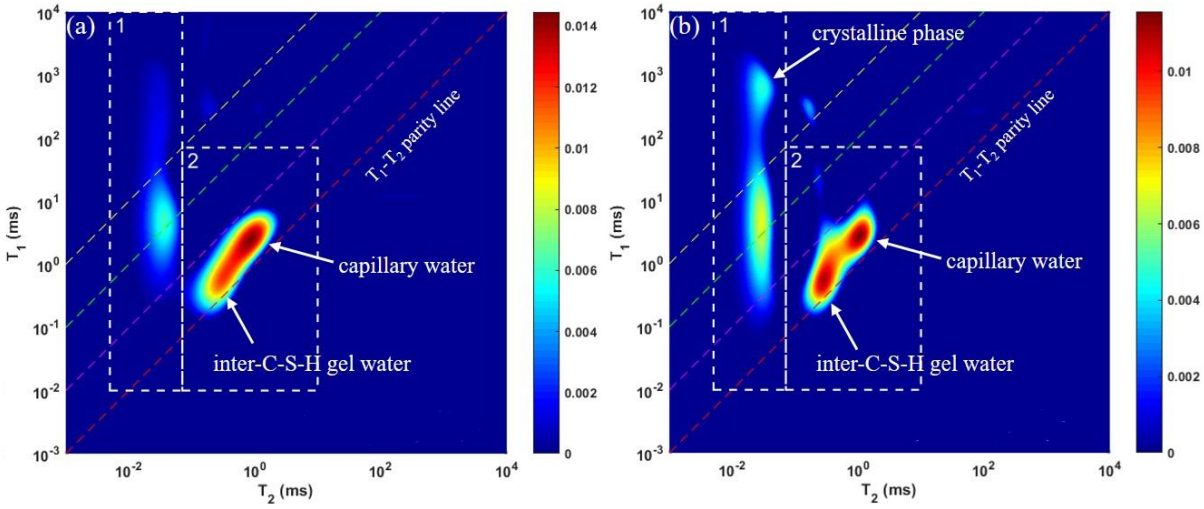

Fig. 1 T_1-T_2 correlation maps of white cement with w/c = 0.4 for 7 days of hydration. (a) conventional T_1-T_2 method, (b) solid echo T_1-T_2 method. (The magenta dashed line represents T_1/T_2 = 10; the green dashed line represents T_1/T_2 = 100; and the yellow dashed line represents T_1/T_2 = 1000.)

Generation of nuclear magnetic resonance logging curves using Bi-directional LSTM

Li Bo * [1]

[1] China University of Petroleum – China

Keywords: NMR curve, prediction, Bi, directional LSTM, deep learning

*Speaker

Magnetic Resonance Imaging as a Non-Destructive Method for the Characterization of Silicone Elastomer Chemistry *In-Situ*

A.M. Sawvel, H.E. Mason, J.M. Knipe, S.C. Chinn, E.A. Glascoe, J.P. Lewicki, and R.S. Maxwell
Lawrence Livermore National Laboratory, Livermore, CA, USA

Introduction: Silicone elastomers have industrial relevance as adhesives, sealants, and engineered parts in a myriad of commercial applications. Commercial silicones can be subject to a variety of curing conditions and harsh aging conditions, such as complex strain fields, that complicate predictions of component lifetime and performance. Non-destructive methods that can quantify changes in silicone chemistry are needed to further our understanding of how environmental stressors contribute to material curing and degradation. Residual proton dipolar couplings present due to topological constraints that prevent complete motional averaging are quite sensitive to morphological changes throughout elastomers.[1-4] Magnetic resonance imaging (MRI) provides an opportunity to spatially resolve fluctuations in dipolar couplings within a sample via changes in transverse relaxation times (T_2).[4-5] Here, we used T_2-weighted MRI not only to quantify the curing kinetics of a silicone sealant but also to visualize areas of material degradation in silicone elastomers as a function of compressive strain and material aging. The results presented here are part of an ongoing effort to develop non-destructive methodologies that can be used to monitor subtle changes in network chemistry as a function of curing, stress, and material lifetime.

Methods: Two-dimensional T_2-weighted images were collected on a 400MHz Bruker AVANCE spectrometer equipped with a high-resolution Micro2.5 microimaging system and a 25mm ^{1}H RF coil. The MSME sequence was employed to collect images for both the curing and strain experiments.

Results and Discussion: *In-Situ* T_2-weighted MRI used to visualize the reaction front of a humidity-cured silicone are shown in Figure 1. Each image in the panel displays a fast relaxation regime (15ms, blue/green) and a slow relaxation regime (40ms, red/orange) associated with the cured and uncured portion of the sample, respectively. Diffusion of water vapor from the surface of the silicone is expected to catalyze curing and create a distinct transition from uncured gel to cured solid. As a result, the reaction front is easily visualized, and kinetics can be determined from by measuring the portion of cured material in these images. These results were used to validate moisture uptake and reaction models for this class of material. In addition, we used MRI to visualize areas of deformation in elastomers placed under compressive strain and these results will also be discussed in detail.

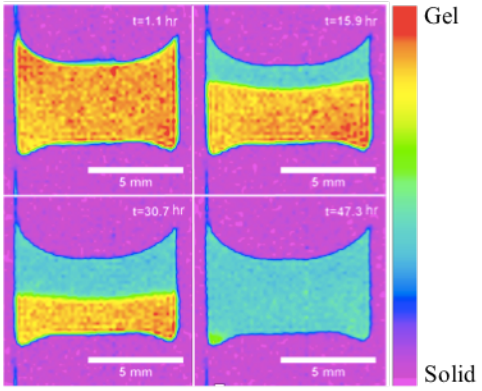

Figure 1. T_2-weighted MRI used to quantify *in-situ* curing kinetics in a commercial, humidity-cured silicone.

Conclusion: Spatially resolved T_2 relaxometry via MRI can be performed *in-situ* to validate curing mechanisms for commercial elastomers and to identify pathways for material deformation while in use. The non-destructive nature of MRI and the ability to collect data under relevant use conditions yields more accurate results than would be obtained through less adaptable methods. This work was performed under the auspices of the U.S. Department of Energy by Lawrence Livermore National Laboratory under contract DE-AC52-07NA27344.

References: [1] Cohen-Addad, Int. J. Radiat. Phys. Chem. (1976). [2] Chinn, Poly. Deg. Stab. (2005). [3] Saalwächter, Prog. Nuc. Mag. Res. Spec. (2007). [4] Herberg, Poly. Deg. Stab. (2006). [5] Blumich, NMR Imaging of Materials (2000).

Exploring the Origins of *Diffusive Diffraction* Behavior in Bottlebrush Polymers

V.J. Witherspoon,[1,2], *M. Komlosh*[2,3], *D. Benjamini*[2,3], *D. Vaccarello*[1], *P.J. Basser*[2]

[1]Material Science and engineering Division, Materials Measurement Laboratory, Gaithersburg, MD , [2]Intramural Research Program, Section on Quantitative Imagining and Tissue Sciences, National Institute of Health, Bethesda, MD, [3] The Henry Jackson Foundation for the Advancement of Military Medicine, Inc., Bethesda, MD, USA

Introduction: Bottlebrush polymers are a class of macromolecules comprising a linear backbone bearing many polymeric side chains (see Figure 1a). Excluded volume interactions between the side chains in densely grafted bottlebrushes causes the backbone and side chains to stretch and reduces intermolecular overlap[1] thus altering the local environment resulting in drastic changes viscoelastic and other macroscopic properties compared to the bulk linear homopolymer of similar molecular weights[2]. These polymers provide an excellent model system for studying the influence of polymer architecture on physical properties as they manifest in many engineering of polymer biological and material applications.

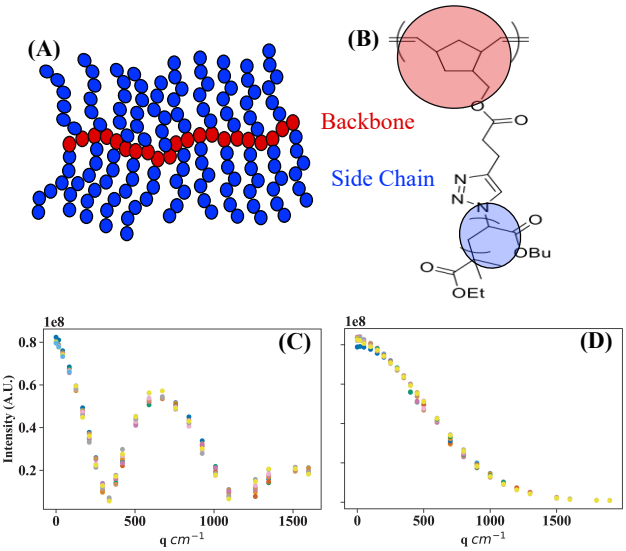

Fig. 1: (A) Schematic of fully grafted bottle brush polymer with (B) chemical formulation. (C) The intensity decay versus q(cm^{-1}) DDE with Δ= 25 ms (C) Δ= 100 ms with τ_m = 10 ms, τ_{Echo} ~ 100 ms., where the different colors are the angles 0-180°.

Method: A fully grafted bottle brush polymer was synthesized with polynorbornene backbone and polybutlyacrylate side chains(~4.1 kg/mol) resulting in molecular weight of ~220 kg/mol. We employed single diffusion encoding (SDE) and double diffusion encoding (DDE) for investigating the microscopic anisotropy of this neat polymer melt. The echo time was kept constant around 125 ms, while the observed diffusion time, Δ, range from 15-100 ms with all orthogonal gradient directions. The DDE mixing times, τ_m, were varied between 10 -100 ms, with the angle between the first (x) and second gradient (xz) pulse varied between 0-180, while the max gradient strength was 1.48 T/m.

Results and discussion: The bottle brush polymer displayed distribution of diffusivities in the melt state. Although generalized coarse-grain simulations studies of the bottlebrush melts indicated that the anisotropic molecular shape[4], we found that this shape did not manifest significant diffusional anisotropy. Suprisngly the DDE signal resulted in diffusive diffraction behavior that displayed non-intuitive dependence on Δ(see Figure 1b and Figure 2c), where characteristic diffraction dips manifested at short Δ yet disappeared as Δ ∞ (100 ms) with all mixing times and orientations.

Conclusion: We employ pulsed field gradient methods to investigate diffusive behavior of the neat brush polymer melt demonstrated a negligible amount of diffusive microscopic anisotropy. However we discovered diffraction phenomenon due to a boundary on the length scales of 3-7 μm which we attribute to hierarchical organization of brush the persist up to 50 ms.

References: [1] Liang, H. Macromolecules (2017). [2] Haugan, I. ACS Macro Lett . (2018) [3] Özarslan, E. J. Mag. Res. (2007) [4] Chremos, A. J. Chem. Phys. (2018)

Can the coagulation process of cellulose be studied by MRI?

M. Gunnarsson[a], *J. Bengtsson*[b], *L. Sveninngsson*[a], *D. Bernin*[a]
[a]Chalmers, Gothenburg, Sweden, [b]RISE IVF, Mölndal, Sweden

Coagulation of dissolved cellulose is an important industrial process for the production of man-made textile fibres, which in comparison to cotton are not based on emptying drinking water, child labor or occupying land that instead could be used for food. Cellulose is commonly dissolved in 1-ethyl-3-methylimidazolium acetate (EMIMAc) while the coagulation bath can be composed of water or ethanol. The fibre quality is known to be highly dependent on the nature of the coagulation process why the mass transport of the coagulation liquid and the cellulose solvent are of interest to study.

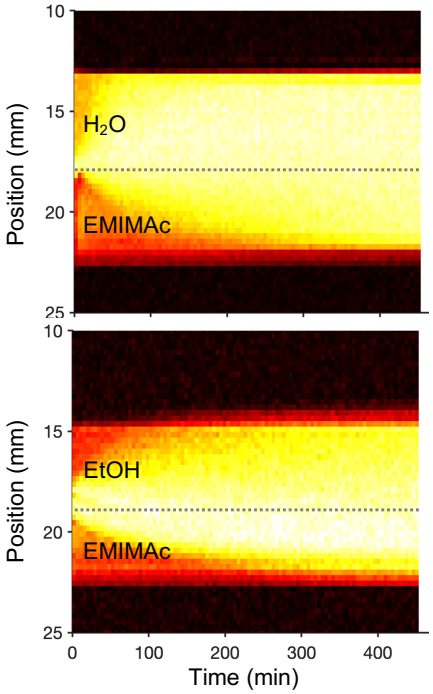

Fig. 1: Vertical profiles extracted from T_2 weighted images stacked with time for EMIMAc and water (top) or ethanol (bottom).

We used a super wide bore 300 MHz, in which we placed a beaker filled with water or ethanol. To follow the mixing between water or ethanol with EMIMAc, EMIMAc was placed on the bottom and water or ethanol carefully on top with a volume ratio of 1:1. For the coagulation, a 2.3 wt% cellulose solution was placed with the help of a syringe on a glass plate, which was then put into the beaker containing water or ethanol. The experiments were started immediately. Here we used a RARE sequence with an echo time of 160 ms to get contrast between the coagulations bath and EMIMAc with 27.5 s temporal resolution. 10 sagittal slices with 1 mm in thickness and a spatial resolution of 270 µm were collected.

The mixing process with time for H_2O or ethanol with EMIMAc was monitored with time (see Fig. 1). After 400 min, there is still a layer of EMIMAc at the bottom (dark red) of the beaker for both cases. The mixing with ethanol appeared slightly slower and an increase in volume was observed. The first test to monitor the coagulation of dissolved cellulose in EMIMAc is presented in Fig. 2. The T_2 weighted image at the start of the coagulation shows the "fibre" in dark red to the left of the glass plate (black). The "fibre" detached form the glass plate immediately. After 24 min, the dark features appeared in the "fibre" suggesting dense and less dense coagulated cellulose regions.

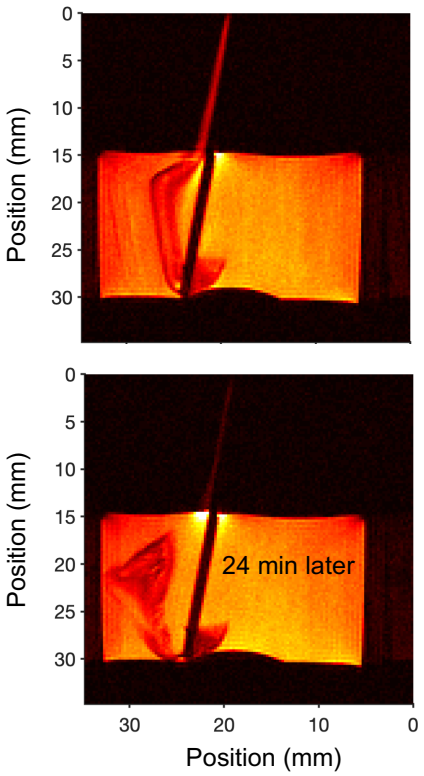

Fig. 2: Sagittal T_2 weighted images for coagulation of dissolved cellulose in EMIMAc in water at the start of the process (top) and after 24 min (bottom).

Preliminary results look very promising. Currently we work on an in situ experimental setup using automated syringe pumps to enable a constant flow minimizing the amount of variables.

Improving magnetic resonance imaging through 3DP

H. Vanduffel[a], *D. Sakellariou*[a], *R. Ameloot*[a,]
[a] cMACS, KULeuven, Leuven, Belgium

Introduction: High levels of magnetic field homogeneity are required inside an MRI scanner to obtain clear and undistorted images. Upon placement of a patient inside the bore, local field inhomogeneities are induced, significantly affecting the imaging quality in terms of signal-to-noise ratio and geometric distortion [1]. Since anatomical features are highly subject-specific, so are the type and extent of the magnetic field distortions. Magnetic fields can be corrected or "shimmed" to achieve the desired levels of magnetic field homogeneity. Currently, shimming is performed "actively" by inducing an electric current through coils and/or "passively" by the strategic placement of materials supporting some level of magnetization (ferro-, dia- or paramagnetic and metallic materials) [2]. Typically, passive shims are constructed by the manual placement of discrete magnetic materials at discrete locations inside the magnet bore in an iterative process [2]. This is a costly, time-consuming process that has difficulties rendering the higher order spherical harmonic terms required to shim field inhomogeneities induced by complex anatomical features. We propose using 3D-printing (3DP) as a novel method for manufacturing subject-specific passive shims. This allows the printing of different concentrations and amounts of magnetic ink at precise pre-calculated positions in the shim design to produce higher spherical harmonic terms.

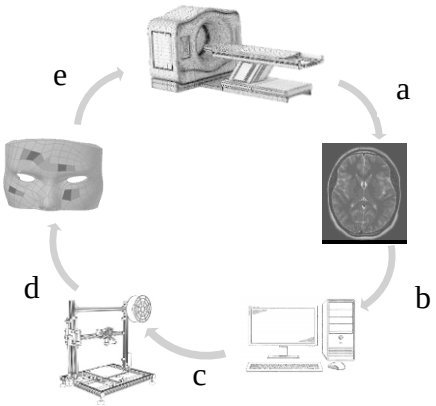

Figure 1: Subject specific passive shimming feedback loop. Field homogeneity maps **(a)** are acquired that are used as subject specific input for the shimming algorithm **(b)**. The shimming algorithm output is translated into a CAD design **(c)** which is then 3D printed **(d)**. The process can then be repeated **(e)**.

Methods: First a subject-specific field homogeneity map is acquired (9.4 preclinical MRI scanner). The subject-specific field maps are used as input for the shimming algorithm which is then translated into a CAD design. The CAD design is 3D printed and the resulting passive shim is used to acquire new MRI images with a higher B_0 homogeneity (fig. 1).

Preliminary results: 3D prints containing the magnetic functionalized ink were successfully printed (fig. 2a) with a resolution of 300 µm. The response of the 3DP shim configurations to a B_0 field of 9.4 T in the z-direction (fig. 2b) indicate that optimizing the shim configuration can be used to manipulate the magnetic field towards a desired state (fig. 2c).

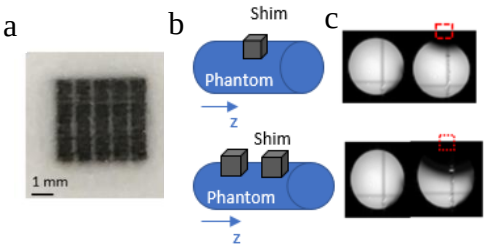

Figure 2: **(a)** 3DP shim b: shim configuration inside 9.4 T MRI scanner bore (blue: phantom, gray: shim) **(b)** Shim configuration inside scanner bore **(c)** Field map of resp. shim configuration as seen in fig. 2b (red: position of shim)

Conclusion and future perspectives: The results indicate that the hereby proposed technique can potentially be utilized to sculpt the magnetic field distribution towards a more uniform state via the passive response of the 3DP shims to the primary B_0 field. Future work will consist of the shimming of ex vivo and in vivo specimens with complex anatomical structures.

References: [1] Juchem, Anal. Biochem. (2016). [2] Koch, JMR. (2006)

In-Situ MR Imaging of Pharmaceutical Tablet Dissolution

B. MacMillan[1], H. Frericks-Schmidt[2], M. Zell[3], B. Balcom
[1]University of New Brunswick, Fredericton, Canada, [2]Pfizer Worldwide Research and Development, Groton, United States, [3]Takeda, Cambridge, United States

Magnetic Resonance Imaging allows intact pharmaceutical formulations to be studied during static and dynamic events, such as dissolution. The dissolution of two controlled release formulations was monitored using MRI methods optimized for visualization of short signal lifetime systems. These methods are SPRITE, a modified fast spin echo method and Pi-EPI.

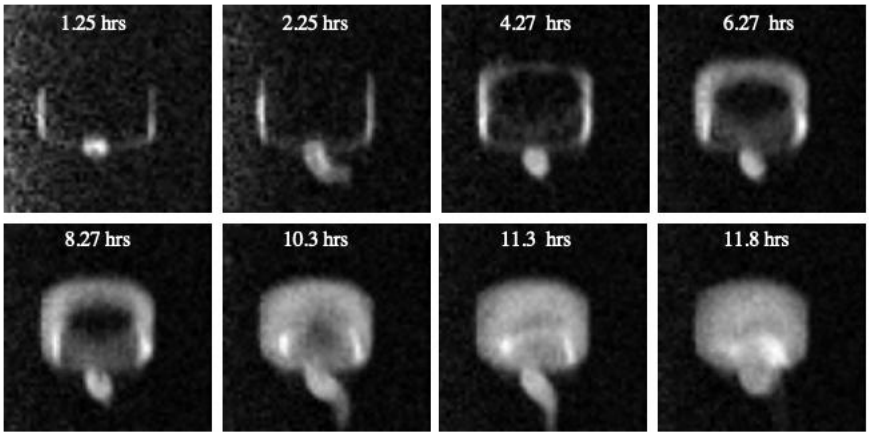

Fig. 1: Two dimensional slices from ^{1}H 3D Pi-EPI images of osmotic tablet dissolution as a function of time after exposure to D_2O. The images reveal excipient swelling with initial water contact then expulsion of the tablet contents through an orifice at tablet bottom.

To highlight wetting of the tablets the methods were optimized to select short T_2/T_2* relaxation and the dissolution was performed in D_2O. Image contrast observed is due to hydration and dissolution of excipients providing insight into the dissolution mechanism. Dissolution events were correlated to the excipient hydration behavior through relaxation properties.

NMR of chemical reactions at elevated process conditions

Hilary T. Fabich[1], Stephen A. Altobelli[1], Partha Nandi[2], Hans Thomann[2], Mark S. Conradi[1]
[1]ABQMR Inc., Albuquerque, USA, [2]ExxonMobil Research and Engineering, Annandale, USA

Introduction: Nuclear magnetic resonance (NMR) can be used to study chemical reactions in-situ and in real time. This is not common practice at conditions of high temperature and high pressure as the design of an NMR compatible reactor is not straightforward. In this study, we report real-time tracking of basic chemical reactions such as oxidation and hydrogenation. We use sealed glass capillaries (ID = 2.6 mm, OD = 7 mm) to hold the sample plus the required oxygen or hydrogen and any catalyst. To seal the capillaries, they are submerged in liquid nitrogen meaning that any condensable gas with a vapor pressure below 0.1 MPa (1 bar) at 77 K can be loaded and sealed. In addition to adding molecules that either freeze or condense at 77 K (including oxygen), hydrogen gas can be added by using a metal hydride that decomposes to release hydrogen at reaction conditions. This means that it is possible to study oxidation, hydration, hydrogenation, hydrogenolysis and isomerization reactions at process conditions with NMR.

Methods: All experiments are run in a 1T permanent magnet with a homebuilt probe. The sample is held in an 8 mm ID coil wound from PEEK coated wire and set in high temperature epoxy. Air flows over a nichrome wound heater stick which is positioned below the sample. It is easy to reach temperatures up to 400 °C. As the samples are sealed the pressure is determined by the contents of the sample. The glass capillaries typically hold up to 7 MPa (70 bar). A basic pulse-acquire sequence is used to acquire spectra at different temperatures. Scan times can be as little as a few seconds, even in the gas phase.

Results and discussion: Using this apparatus it is possible to track chemical reactions in real time. Figure 1 shows an example reaction of cyclohexene with a catalyst, platinum on alumina. The unreacted cyclohexene, top spectrum in Figure 1, has three peaks (1.6 ppm, 2.0 ppm and 5.7 ppm). As the sample is heated, the cyclohexene acts as both a hydrogen donor and acceptor, converting to cyclohexane and benzene. The middle spectrum shows five peaks with a decreasing concentration of cyclohexene and increasing concentrations of cyclohexane (1.4 ppm) and benzene (7.3 ppm). The bottom spectrum shows the fully reacted sample with only cyclohexane and benzene. If hydrogen gas is added to the fresh sample in addition to cyclohexene, the reaction will run to complete saturation, showing only cyclohexane and any excess hydrogen gas in the final spectrum.

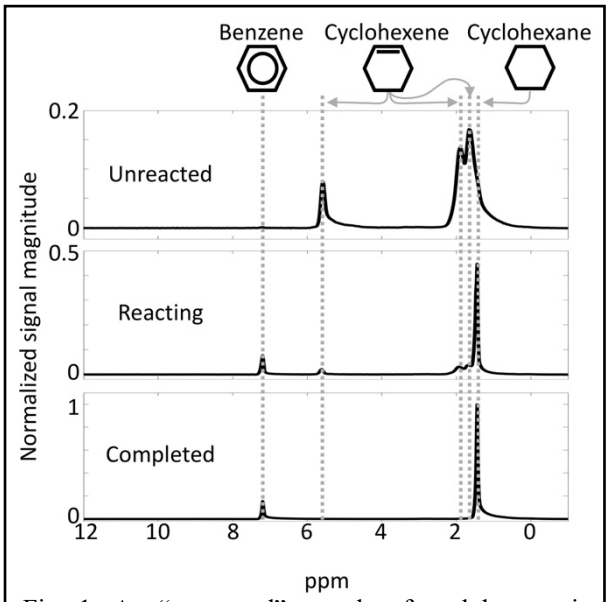

Fig. 1: An "unreacted" sample of cyclohexene is heated with a catalyst. The "reacting" sample is observed to produce benzene and cyclohexane. When all of the cyclohexene is consumed, "reacted", the sample has only cyclohexane and benzene.

Conclusion: The example of cyclohexene reacting to form cyclohexane and benzene is one of many reactions that occur at elevated temperatures which can be studied with low field magnetic resonance spectroscopy. These types of experiments open a new window to reaction engineering using NMR spectroscopy as a real-time monitor.

Design of main control system for nuclear magnetic resonance LWD tool

Yangyang, Xu[a], Guangzhi, Liao[a], Lizhi, Xiao[a],Hao,Liu[a],Wei,Liu[a]

a. State Key Laboratory of Petroleum Resources and Prospecting, China University of Petroleum, Beijing, China

NMR logging while drilling is a logging method for real-time measurement of formation information. It can measure the formation in real time, obtain accurate formation parameters. To design of the main control system of the NMR LWD tool we need to combine the cable NMR logging tool with the characteristic of LWD. The block diagram of main control system is shown in Fig. 1.

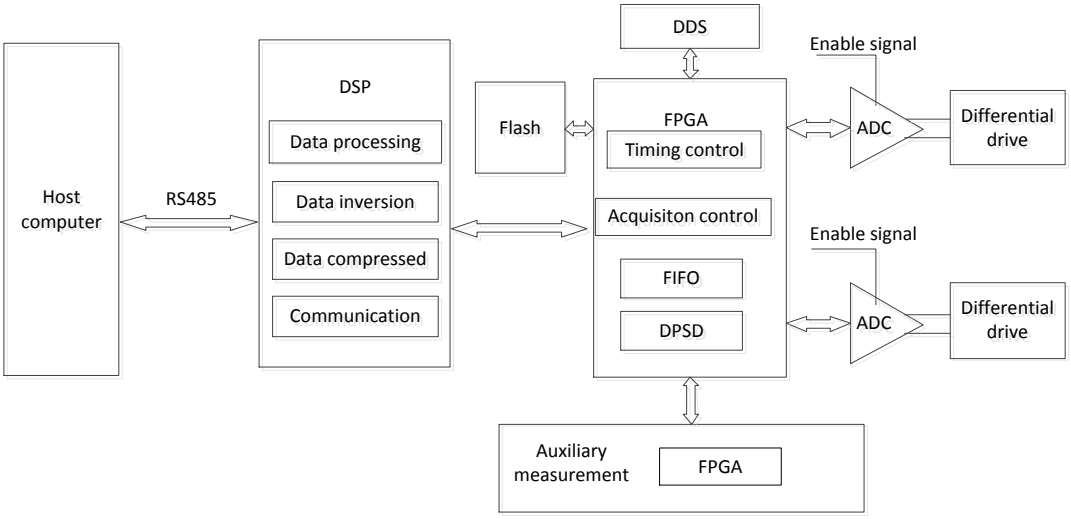

Fig. 1-The block diagram of main control system

The main control system adopts the embedded mode of DSP+FPGA. The DSP is used to complete the communication with the ground system and the compression processing of the echo signal data. The FPGA is used to generate all timing control signals. The DDS provides a reference clock for the generation of each timing signal; the ADC is used to convert the amplified analog echo signal into a digital signal. The main control system software design includes the slave computer control program design and the host computer software development. The host software design is based on the QT development platform to design the module function to match the NMR LWD tool. At the same time, the host computer interface is designed to achieve better human-computer interaction. Fig. 2 is the block diagram of main control system state transition in CPMG working mode.

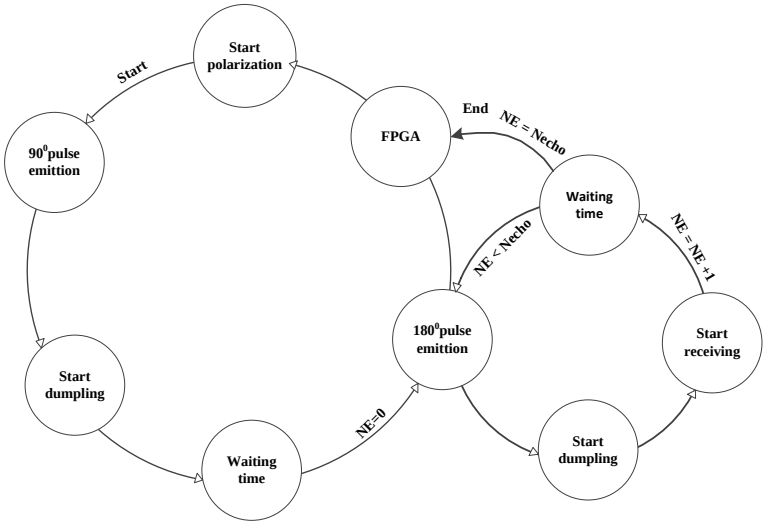

Fig. 2-The block diagram of main control system state transition

References:

[1] HALLIBURTON. MRIL Prime field operation manual[Z]. 2001.
[2] BAKER ATLAS. Magnetic resonance Explorer maintenance manual[Z]. 2004.
[3] SCHLUMBERGER. Magnetic Resonance eXpert maintenance manual[Z]. 2003.
[4] TAKEDA K. OPENCORE NMR: Open-source core modules for implementing an integrated FPGA-based NMR spectrometer[J]. Journal of Magnetic Resonance, 2008, 192(2): 218-229.

A New LWD Magnetic Resonance Imaging Tool

Zhe Sun[1], Lizhi Xiao[1, 2], Guangzhi Liao[1], Yan Zhang[1], Sihui Luo[1], Feixue Gong[1], Zhihao Long[1]

[1]State Key Laboratory of Petroleum Resources and Prospecting, China University of Petroleum, Beijing, China;

[2]Harvard SEAS-CUPB Joint Laboratory on Petroleum Science, 29 Oxford Street, Cambridge, MA, USA

In this paper, we will introduce the development of our logging while drilling (LWD) magnetic resonance imaging tool emphasized on probe performance. The LWD measurement could provide original information of the reservoir. A new LWD probe is designed and implemented in our borehole NMR tool, as shown in Fig.1. In general, only the instruction information can be acquired using the traditional (wireline) downhole NMR tools. The original information is equally important to instruction. In many cases, information influenced by partial invasion of drilling fluid or mud around borehole will cause problems and may have serious impact on applications. Improvement the LWD magnetic resonance imaging tool is the right direction for solving these problems.

Early version of the LWD magnetic resonance imaging tool was designed in 1995 (Halliburton & Sperry–Sun). Due to the characteristics of the LWD measurement, the probe remains vibration during measurement. The SNR of the echo may decrease dramatically due to B_0 changes caused by vibration. Moreover, the severe space limitation in the borehole poses a serious challenge to the design of the probe. As a result, how to design a probe that satisfies both the mechanical strength and the magnetic field strength is essential.

We have designed and built a new probe which includes 2 long hollow cylindrical magnets as the main magnets, 2 short hollow cylindrical magnets as the adjustment magnets and a hollow soft magnetic material part in the middle to produce the B_0 field, as shown in Fig.2. The total length of the magnet assembly is about 70 cm, which significantly improves the reliability of the machine strength of the whole tool. The 2 short hollow cylindrical magnets in both sides are used to adjust the location of the homogenous region around the probe and the height of the homogenous region along with y-axis. A winding coil with a wide frequency band corresponding to the width of homogeneous region has been designed for matching the static magnetic field. The sensitive region of our tool is about a 5 cm thick hollow cylinder at the working frequency, which could effectively suppress the SNR reduction caused by vibration and give the original information of the borehole. Simulation result of sensitive region width is shown in Fig.3. We will discuss the probe design and test performance in details.

Fig 1 –A new LWD probe is designed in our borehole NMR tool

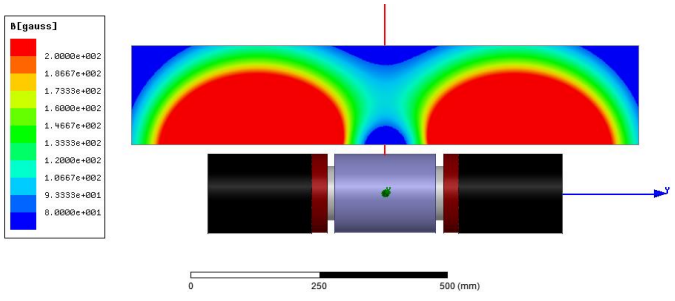

Fig 2 – Magnets assembly and its produced magnitude distribution of B_0. The total length of the magnet asembly is about 70 cm. The shape of the senstive region based on B_0 is an "X". The corresponding larmor frequency is about 500 kHz.

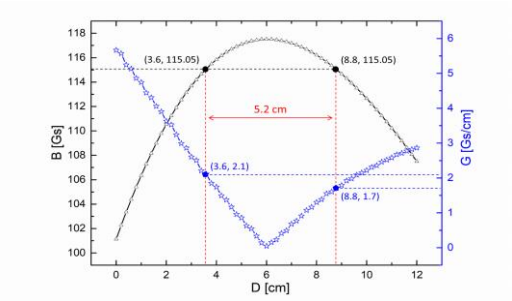

Fig 3 – Width of the sensitive region. The central point of the senstive region is about 16 cm away from y-axis. The gradient of B_0 in the sensitve region is no more than 2.1 Gs/cm.

References:

[1]Prammer, Concept Magn. Reson (2001). [2] Morley, SPE (2002). [3]Hürlimann, J. Magn. Reson. (2000).

Study on Evaluation of Vector Matching Effect between B_0 and B_1

Feixue Gong[1], *Lizhi Xiao*[1,2], *Guangzhi Liao*[1], *Yan Zhang*[1], *Zhe Sun*[1], *Sihui Luo*[1], *Zhihao Long*[1]

[1]State Key Laboratory of Petroleum Resources and Prospecting, China University of Petroleum, Beijing, China;

[2]Harvard SEAS-CUPB Joint Laboratory on Petroleum Science, 29 Oxford Street, Cambridge, MA, USA

In this paper, we will focus on the evaluation method and the influence of vector matching effect between static magnetic field (B_0) and radio frequency field (B_1) on SNR. Probe is the core component of a NMR logging tool and consists of a magnet and an antenna. The matching effect between the magnet and the antenna has an important influence on the detection effect of the instrument. A well-designed antenna can efficiently excite and detect samples, greatly improving signal-to-noise ratio and detection sensitivity. Therefore, evaluating the vector matching effect between B_0 and B_1 is crucial for probe design and optimization.

It is can be considered as that the NMR signal strength is always influenced by the directional matching between B_0 and B_1.The component of B_1 orthogonal to B_0 can be defined as:

$$B_{1c} = \frac{1}{2}\left[B_1(r) - B_0(r)\frac{B_1(r)\cdot B_0(r)}{B_0(r)\cdot B_0(r)}\right] \quad \text{Eq.1}$$

Then the induced voltage signal measured in the coil can be calculated as:

$$V_{x,y}(t) = \frac{2\chi}{\mu_0}\int dr\Phi(r)B_0^2(r)\frac{\omega_1(r)}{I}F\big(\Delta\omega(r)\big)m_{x,y}(rt) \quad \text{Eq.2}$$

However, the strength matching relationship between B_0 and B_1 is equally important to further optimize the design of the probe structure.

Figure 1 shows the directional relationship between B_0 and B_1. The B_0 and B_1 vector data were used to draw their angles at the same point to see if B_0 and B_1 are orthogonal. The angle contours between B_0 and B_1 in figure 1 can be used to evaluate the direction matching effect between B_0 and B_1 to optimize the antenna structure. In order to obtain a larger resonance region and a higher NMR signal, it is necessary to match the intensity shapes between B_0 and B_1 as much as possible. Fig. 2(a) shows the intensity contours distribution of B_0 generated by the magnet, and Fig. 2(b) shows the intensity contours distribution of B_1 emitted by the antenna. The detection distance of the instrument is determined by B_0. The intensities of B_0 and B_1 at the same detection distance were selected, and their contours were drawn to match the shape. Using their data points to find their correlation, the intensity matching effect between B_0 and B_1 is obtained. As shown in Fig. 2(c), the matching degree is 99.96%. Optimizing the vector matching effect between B_0 and B_1 can maximize the sensitive area of the nuclear magnetic resonance logging probe and obtain a greater signal-to-noise ratio.

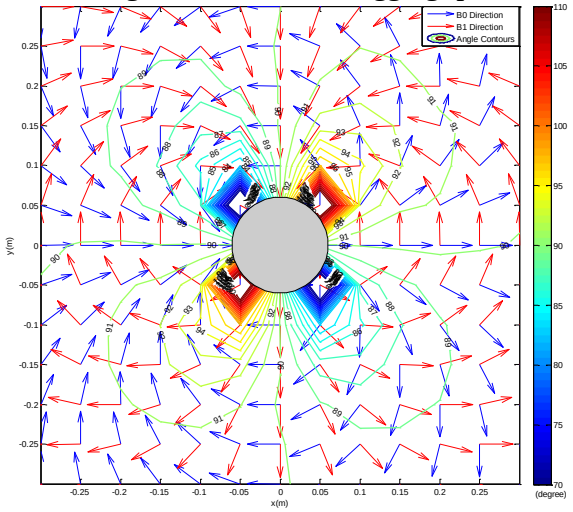

Figure 1 –Directional relationship matching between B_0 and B_1

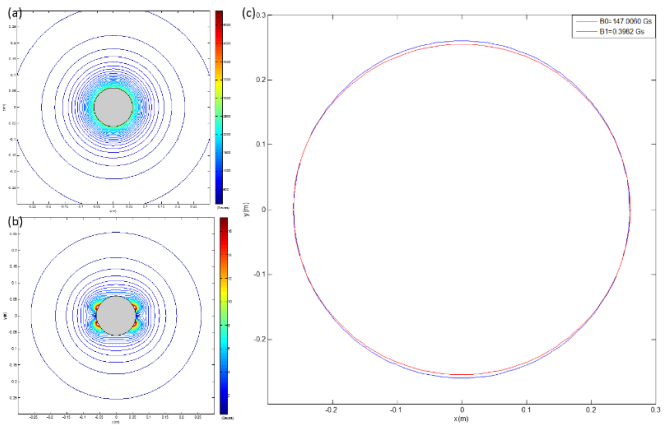

Figure 2 – (a) Intensity contours of B_0. (b) Intensity contours of B_1. (c) The intensity contours matching between B_0 and B_1 at the same detection distance

References: [1] Hürlimann, J. Magn. Reson. (2000).

Circuit Design of NMR Logging While Drilling Device

Authors: Yao Wei[a] , Guangzhi Liao[a], Lizhi Xiao[a], Wei Liu[a]
China University of Petroleum, Beijing, China

Nuclear magnetic resonance (NMR) logging while drilling can acquire abundant NMR information of formation fluid in real time during drilling[1]. While drilling NMR logging tools work in high temperature and high pressure, strong vibration environments. The structure of NMR logging tool is complex and challenging due to weak signal strength and low frequency of operation and extreme operating conditions. The electronic circuit of this instrument includes power amplifier, Q-switch, de-coupler/duplexer, preamplifier and digital circuit (Figure 1). The output voltage of a dual full-bridge switch mode power amplifier drives coil load directly without high-power transformer at 2400V, which is four times higher than the input DC voltage. Q-switch circuit is used to discharge the energy of the RF coil is controlled by a high voltage MOSFETs, which quickly releases the energy and efficiently shortens the recovery time of the RF coil. The de-coupler/duplexer uses actively controlled MOSFETs in order to protect the receiver. The pre-amplifier was designed based on low-noise principles with the first stage being a low noise BJT and second stage being a high-gain operational amplifier. The programmable attenuation is used to increase the dynamic range of the receiver amplifier circuit. Digital Signal Processor (DSP) and Field Programmable Gate Array (FPGA) are embedded in main-controller to generate pulse sequences, control instruments and acquire signals. The amplitudes and phases of echo signals are extracted with the digital phase sensitive detection (DPSD) algorithm.

This instrument has been tested in calibrator tank and acquired good echo train signal.

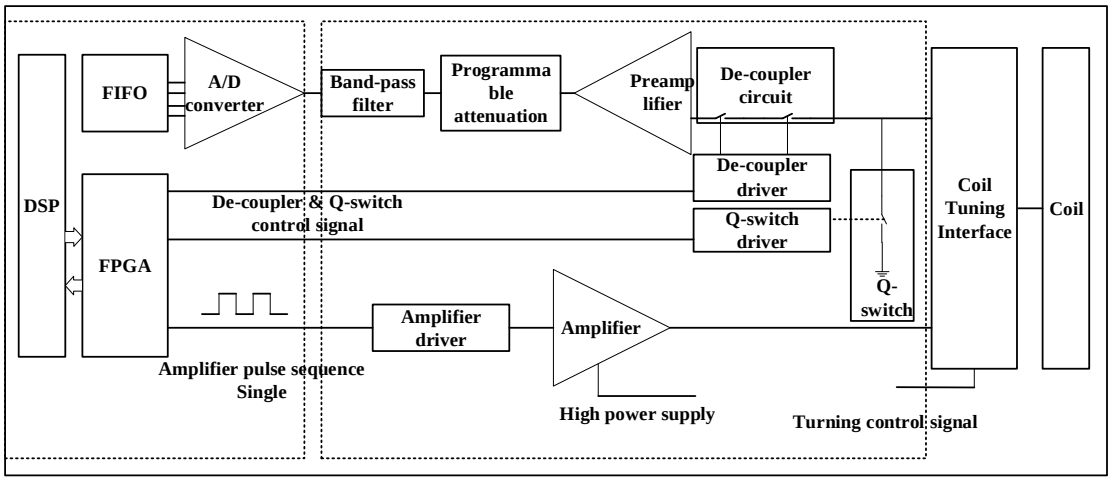

Fig 1： The functional block diagram of electronic circuit

Reference: [1] Coates G R, Xiao L Z, Prammer M G. NMR Logging Principles and Applications. (1999).

Study on RF coil design in LWD MRI tools with target field method

Zhihao Long [a], *Guangzhi Liao* [a], *Lizhi Xiao* [a, b], *Yan Zhang* [a], *Zhe Sun* [a], *Sihui Luo* [a], *Feixue Gong* [a]

[1]State Key Laboratory of Petroleum Resources and Prospecting, China University of Petroleum, Beijing, 102249;
[2]Harvard SEAS-CUPB Joint Laboratory on Petroleum Science, 29 Oxford Street, Cambridge, MA 02138

The inside-out design concept has expanded the application of MR tools to the reservoir measurement. The design of corresponding RF coils in these NMR logging tools has shifted from generating the magnetic field of coil inside to outside. Different with the wire line tools, the detecting SNR of logging while drilling (LWD) tools is lower, because of the influence of vibration, that propose a serious challenge to the design of the RF coil in the LWD tools. This adds requirements on the design of the RF coil for the LWD MR tools.

The RF coil design of the LWD MR tool is a kind of electromagnetic field inverse problem. The RF coil design methods in bench top tools used the target field method and stream function method. At present, the design of the coil of LWD and the optimization forward is still relay on the experience of designer. It is impossible to consider the influence of multi factors in the coil optimization process, and subsequent adjustment of the coil is cumbersome. Therefore, this paper applied the coil design method on the medical MRI tool to the design of the RF coil of the LWD tool.

This paper proposed a target field method to design a solenoid-type RF coil. The calculation method of the RF field is derived according to the electromagnetic field theory. The magnetic induction intensity B and the current density j are developed by the Bessel function to obtain the series expansion of the current density. Based on the Tikhonovz regularization method, the ill-conditioned problem in the equation solving process is solved by combining with the minimum coil length penalty function and the minimum eddy current loss penalty function. Therefore the current density distribution is obtained. The coil current path is obtained by discretizing the continuous current density distribution by the stream function method. We have used this method to calculate the internal magnetic field, the result is simulated by commercial software Ansys Maxwell and has shown in Fig.2. The external magnetic field will be discussed in the following work.

Fig 1–Schematic diagram of coil. The parameters of coil is calculated by TF method.

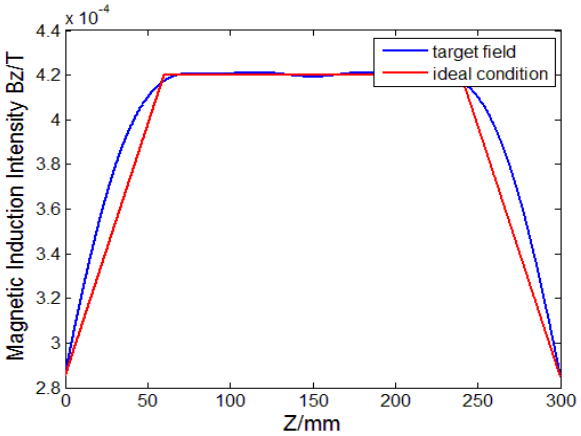

Fig 2–The result of the simulation is obtained by commercial software Ansys Maxwell.The blue one is the magnetic induction intensity Bz of target field Pointing in the z direction, the red one is the intensity in ideal condition. The correlation coefficient is 0.9817.

References: [1] Prammer, Concept Magn. Reson (2001). [2] Turner, J Phys D (1986).[3] Forbes, IEEE. Trans Magn (2004)

Matrix coil design based on target field method for Halbach magnet

Yajie Xu, Ya Wang, Xiaodong Yang
Suzhou Institute of Biomedical Engineering and Technology, Suzhou, China

Introduction: The Halbach magnet has the advantages of small size, high magnetic field strength, low stray field, thus it is of great potential in NMR applications[1]. However, the poor uniformity of the magnetic field has restricted its application and additional active shimming coils are required. Matrix coil could implement high order shimming taking up less coils space [2], which is suitable for Halbach shimming, but coils structure should be reasonably designed to fit the inhomogeneity.

Methods: Cylindrical shape is utilized as the current carrying surface for Halbach magnet. Therefore surface current can be simplified as axial and angular current densityJ_z, J_φ, respectively. For matrix coils, surface is separated into $K\times Q$ subregions, each with its local current density function. While[3] has given a model with directly calculation of each coil current to approximate the total target field. Here we combine field composition with spherical harmonic basis functions to simplify the calculation. Set Source points $r'(f,\alpha,\varphi)$ and field points$r(r,\theta,\phi)$, and current density in angular and axial direction could be denoted as the sinusoidal and cosinusoidal composition weighted by current coefficient U_{kq}^{vh}, where v, h are order in angular and axial direction[3]. Hence, the magnetic field $B_y$could be calculated by $dB_y = (\nabla 1/|r-r'|\times \mathrm{J})_y$. With the Green's function $1/|r-r'|$ decomposed in polar coordinate, magnetic field could be deduced as

$$dB_y = \frac{\mu_0}{4\pi}\sum_{n=0}^{N}\sum_{m=-n}^{n}\sum_{k=1}^{K}\sum_{q=1}^{Q}\sum_{v=1}^{V}\sum_{h=1}^{H}\varepsilon_m\frac{(n-m)!}{(n+m)!\,f^{n+2}}r^nP_n^m(\cos\theta)(\cos m\phi \quad \sin m\phi)\times \begin{pmatrix} -B\cos\varphi_{i,j}\cos m\varphi_{i,j}J_z^{kq} + A\sin\varphi_{i,j}\cos m\varphi_{i,j}J_\varphi^{kq} - C\sin\varphi_{i,j}\sin m\varphi_{i,j}J_z^{kq} \\ -B\cos\varphi_{i,j}\sin m\varphi_{i,j}J_z^{kq} + A\sin\varphi_{i,j}\sin m\varphi_{i,j}J_\varphi^{kq} - C\sin\varphi_{i,j}\cos m\varphi_{i,j}J_z^{kq}\end{pmatrix}\mathrm{d}z\mathrm{d}\varphi \qquad \text{Eq. 1}$$

In which $A=-(n+1)P_n^m(\cos\alpha)\cos\alpha - fC_{nm}^{Z1}$, $B=-(n+1)P_n^m(\cos\alpha)\sin\alpha + fcot\,\alpha C_{nm}^{Z1}$, $C=mfP_n^m(\cos\alpha)$, $C_{nm}^{Z1}=(n-m+1)P_{n+1}^m(\cos\alpha)-(n+1)\cos\alpha\,P_n^m(\cos\alpha)$, $\varepsilon_m=1$(m=0),2(other m). Hence, comparing with the spherical harmonics decomposition $B_{n,m}=r^n(a_{nm}\cos m\phi + b_{nm}\sin m\phi)P_n^m(\cos\theta)$, the coefficients U_{kq}^{vh} of current density function of each coil unit could be obtained targeting at the desired target SHs setting, so the winding pattern of coils in each subregion could be achieved.

Results and discussion: With N=5 and V=H=5, for the target field SH(1,-1), coil winding with diverse K and Q are optimized as shown in figure1. This could be the fundation of matrix coils optimization for multi target field components. With constrains of the power consumption, current amplitude and current density coefficients, more applicable matrix coils structure for Halbach magnet shimming could be achieved.

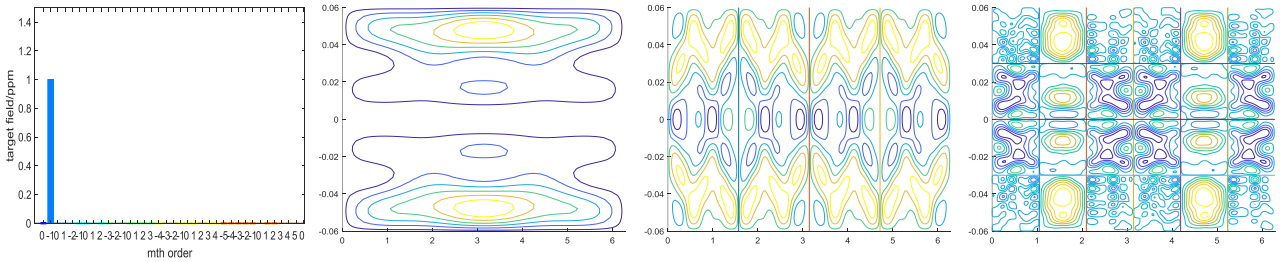

Fig. 1: target field SH(1,-1) in a) and the coil winding result for each subregions with diverse K and Q value: b) K=1, Q=1, c) K=4, Q=1, d) K=6, Q=4,

Conclusion: We proposed a matrix coils optimization algorithm based on target functions method which allows a high weight for specified target field component design to fit the actual shimming requirement. Furthermore this is also applicable for the zeros order RF coils design and traditional shimming coil design for each SHs upon a regular cylindrical surface.

References: [1] Blümich. Encyclopedia of Analytical Chemistry (2016). [2] Juchem. J. Magn. Reson.(2010). [3] While. IEEE Trans. Biomed. Eng. (2014).

An open PXIe based scalable MRI console

A. Ang[a], G. Yang[a], S. Obruchkov[a] and R. Dykstra[a]
[a]Victoria University of Wellington, Wellington, New Zealand,

Introduction: MRI console development is often impeded by high speed requirements and complexity. With PCIe at its core, Peripheral eXtensions for Instrumentation express (PXIe) standard can provide a good solution as it provides significant data bandwidth, and synchronisation capabilities. However, it usually contains proprietary IP. We have developed a modular open source PXIe platform tailored for MRI console development.

Method and Implementation: A PXIe system is typically composed of several modules: system controller board, system timing board and a few peripheral boards that provide specific functionality. These are housed in a PXIe chassis. The system controller board provides a user interface through an operating system (OS), allowing control of any peripheral boards. Synchronisation between multiple boards is carried out by a system timing board.

Field Programmable Gate Array (FPGA) devices and the availability of open-source Linux operating systems made it convenient to develop an open PXIe platform. To overcome the proprietary IP associated with PXIe we developed our own open IP solution [1]. We constructed a general-purpose PXIe system controller board, a rapid prototyping peripheral board, and RF transceiver and gradient controller boards. Development of the platform consisted of hardware and software components for both system controller and peripheral boards. On each peripheral board, FPGA fabric was used to implement a direct memory access (DMA) and programmed input/output (PIO) engine which interfaces with the root complex of the host system controller. In our case, the host system controller was based on the Xilinx Zynq series system-on-chip (SoC). The management of data transfer between the host and an endpoint was provided by a device driver for the host operating system. An API layer was developed to provide a simple method of performing I/O transactions between the host and the endpoint fabric of each peripheral board.

A Eurocard sized PXIe system board was developed based on the Picozed Zynq 7015 module with a 4 lane PCIe root complex [2]. Gigabit ethernet, USB and TTL IO are also provided. Other Eurocard sized PXIe peripheral boards were developed based on the Artix-7 TE0712 module from Trenz Electronics [3]. The FPGA device is used to host the PCIe endpoint and provide programmable logic to support functionality. A multi-channel transceiver peripheral board consisting of a 16bit, quad-channel, 125MSPS Analog-to-Digital Converter (ADC) and a 16bit, dual-channel, 500 MSPS Digital-to-Analog (DAC) was designed. Parallel imaging can be performed as well as multiple transmit channel encoding to enable methods such as TRASE [4].

Conclusion: An open PXIe platform is presented consisting of a system controller and peripheral boards. The DMA/PIO engine allows fast data transactions to be performed at 5GB/s. The software complexity of data transfers was reduced to API functions and hardware complexity was reduced using SoM solutions. Peripheral modules were developed to provide RF and gradient capabilities.

References: [1] Bourne, Proc. Intl. Soc. Mag. Reson. Med. 25 (2017). [2] Avnet, http://zedboard.org/product/picozed, (2017). [3] Te0712, https://www.trenz-electronic.de. [4] Sharp, Mag. Reson. Med, 63(1), (2010).

Q-Switch for Earth-Field NMR Systems

J. Zhen[a], *P. Stanwix*[a], *E. Fridjonsson*[a], *M. Johns*[a]
[a]University of Western Australia, WA, Australia

Introduction: A NMR Q-switch can reduce the RF probe ring-down time and therefore enable earlier signal acquisition. In previous research, we have shown a Q-switch that reduced the acquisition delay of an Earth-field system from 25 ms to 9 ms, which for example increased the velocity range as an NMR flow meter by a factor of 4 [1]. Here we present an improved Q-switch design that further reduces the acquisition delay to 5 ms.

Method and Results: As with the previous design, the Q-switch is external to the spectrometer and no modification to the existing hardware are required. While the previous design used a single resistor to change the Q of the system, the new design uses an isolation method to split the LC components of the tune circuit and discharge them separately. This design is suitable for the Magritek Terranova Earth-field system [2] because the L and C components are accessible from outside the spectrometer box (L is the inductance of the B_1 coil/probe and C is the spectrometer tuning capacitance). Once in isolation, the tuning capacitors can be easily discharge via a resistor. The energy stored in the inductor (RF coil) is also dissipated through a resistor load. To speed up this process, a higher frequency (~50 kHz) series resonance circuit was formed by switching on a capacitor in series with the inductor and the load resistor. A series resonant circuit has a minimum impedance at resonance, therefore delivering the highest circuit current which gives maximum power dissipation on the load resistor. The more energy that is dissipated from the inductor, the shorter the circuit oscillation when it connects back to the original tuning capacitor, resulting in a shorter acquisition delay time. Preliminary test results from the new design have shown the Earth-field system is now able to capture NMR signals of under 9 ms duration, which was not possible previously, sample data is shown in figure 1.

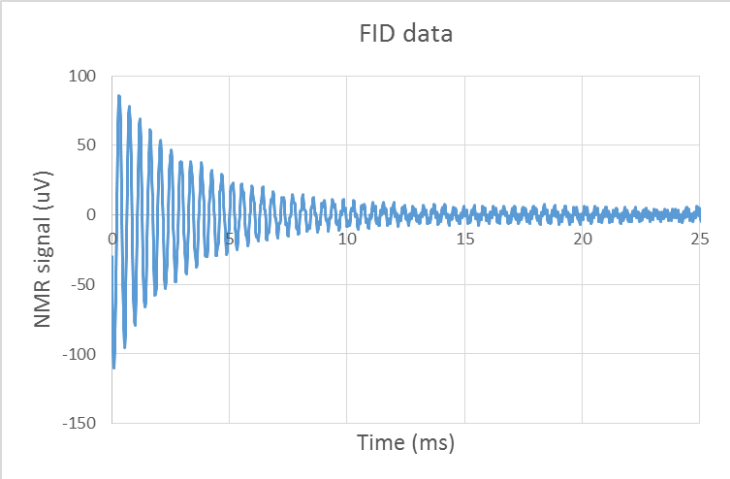

Fig. 1: FID of Iron Oxide solution with concentration of 12.96 mMol/L. The T_2* for this system is 3.7 ms.

Conclusion: An improved Q-switch design was successfully implemented and tested on a commercial Earth-field NMR spectrometer. The reduced acquisition delay of 5 ms broadens the applications of the system, especially in the field of NMR flow metering.

References: [1] Zhen et al., JMR, 287 (2018). [2] http://www.magritek.com/products/terranova/

Inside-out NMR with concentric ring magnets

Shin Utsuzawa, Yi-Qiao Song
Schlumberger-Doll Research, Cambridge, MA 02139, USA

Introduction:

Inside-out NMR can examine samples without regard to sample size. It is also an easy path to mobile NMR as well as inexpensive NMR. One way to accomplish inside-out measurements is to use a saddle point where the derivatives of the B_0 field are nulled, such as the one produced by a barrel magnet [1] or other magnet arrays (for example, [2]). The relatively homogeneous B_0 field of these magnets allows the measurement of rapidly diffusing spins as well as the use of smaller RF amplifiers, which enhances system mobility. In this work, we present a miniature barrel magnet that consists of concentric ring magnets to provide an enlarged sensitive region.

Materials and methods:

We constructed a miniature barrel magnet by using off-the-shelf ring magnets (Fig. 1). The dimensions of the ring magnets are as follows: OD = 50.8 mm, ID = 25.4 mm, H = 25.4 mm (outer magnet); OD = 19.05 mm, ID = 3.175 mm, H = 12.7 mm (inner magnet). Both magnets are N42 grade NdFeB and magnetized in axial direction to produce a saddle point at distances determined by OD and ID. When the size and the position of the inner magnet are appropriately chosen, two magnets create an extended homogeneous region in axial direction.

To generate an oscillating magnetic field B_1, we used a variant of a figure-eight coil that is known for noise immunity [3]. A double-D shaped flat coil (L = 0.3 μH) was mounted on the magnet and tuned to 6.8 MHz. The sensitive region extends 1~7 mm in axial direction and 4~6 mm in radial direction above the coil surface (Fig. 2). Samples can be either scanned while the sensor is hand-held or simply placed on top of the magnet with no preparation.

Results and discussion:

Figure 3 shows CPMG signals obtained with a miniature barrel magnet. It gives excellent sensitivity, which helps to minimize the number of scans to measure long T_1/T_2 samples. For this configuration, the matching of two ring magnets is crucial to get an extended homogeneous region. However, it is straightforward to find off-the-shelf ring magnets with small OD (< ~50 mm) and various ID/height, making it a convenient way to accomplish inside-out NMR with minimal effort.

References:

[1] S. Utsuzawa and E. Fukushima, *J. Magn. Reson.* 282 (2017).
[2] A. E. Marble, I. V. Mastikhin, B. Colpitts and B. Balcom, *J. Magn. Reson.* 186 (2007).
[3] D. Trushkin, O. Shushakov and A. Legchenko, *Geophys. Prospect.* 42 (1994).

Fig. 1. A small inside-out sensor built with a barrel magnet and a double-D coil.

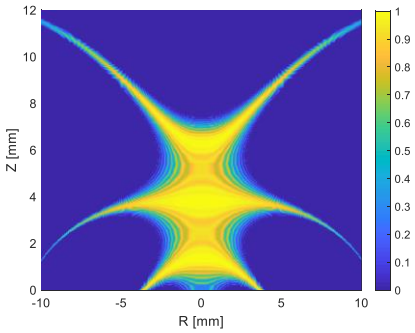

Fig. 2. Sensitivity map assuming t_{180} = 18 μs (requiring < 30 W). The origin of Z is the coil surface.

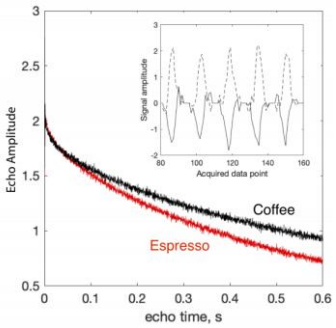

Fig. 3. CPMG signals obtained with the barrel magnet from a cup of coffee (black) and espresso (red). The inset shows the 6-10th echoes after 2 scans.

A radio frequency coil for non-invasive nuclear magnetic resonance detection of human finger blood glucose

Junnan Wang[a,b], *Yi Chen*[a,b], *Yuchen Wu*[a,b], *Zhonghua Ni*[a,b], *Rongsheng Lu*[a,b,*], *Hong Yi**

[a]Jiangsu Key Laboratory for Design and Manufacture of Micro-Nano Biomedical Instruments, Nanjing, China

[b]School of Mechanical Engineering, Southeast University, Nanjing, China

*corresponding author：Rongsheng Lu, lurs@seu.edu.cn or Hong Yi, yihong@seu.edu.cn

Abstract：Nuclear magnetic resonance instruments that can achieve non-invasive detection of human blood glucose are of great significance. However，it is well known that the blood glucose NMR signal in the human finger is very small, and the detection of the signal is prone to be affected by the high dielectric dispersion of the human body. Therefore, this paper designs a radio frequency coil called T coil with low-E field and high radio frequency field uniformity to improve the detection sensitivity of NMR signal from human finger blood glucose. A single-turn wide copper strip with loop-gap in the middle of the T coil is cascaded with two single-turn thin copper strips with loop-gap which are distributed at two ends. The T coil takes on an excellent RF field homogeneity in view of the strong aggregation of the current at both ends of the RF coil. In order to determine the best geometric parameters of the coil, they are simulated and optimized by electromagnetic field finite element analysis method. As a result, the width of the intermediate copper foil is 46mm，and the width of sides copper foil is 1mm. The total length is 50mm, and the inner diameter is 29mm. Subsequently, the T coil proposed in this paper is compared with the conventional solenoid coil and variable width solenoid coil. The simulation results show that the region along the axis where the RF field strength deviate within ± 5% from the center value accounts for 96.44% of the total length of the coil, far superior to the conventional solenoid coil and variable width solenoid coil. In addition, the characterization of the uniformity on the three planes is also optimal. Then, a thin grease layer and a nutation decay experiment were designed to verify the simulation. The experimental results are consistent with the simulation analysis, indicating that the T coil has the best RF field homogeneity and the minimal dielectric loss. Finally, based on this new coil structure, a radio frequency probe was designed and fabricated. Combined with commercial magnets, commercial electronic control system and self-made temperature control system, a human finger nuclear magnetic resonance detection device was built. The dead time of this probe is 40us. The pulse width of 90 degree is 8.4us, and the half-peak width of deionized water is 16.7 ppm. The fluctuation trend of the transverse relaxation time of the human finger before and after the meal was obtained, which was consistent with the trend of the true blood glucose concentration monitored by the Roche blood glucose meter. In conclusion, with the T coil, we has successfully bridged the correlation between the blood glucose concentration and the transverse relaxation time of human fingers, which will advance the development of non-invasive detection of human blood glucose by low-field NMR.

Keywords: Low-field NMR, RF coil, Non-invasive, Blood glucose

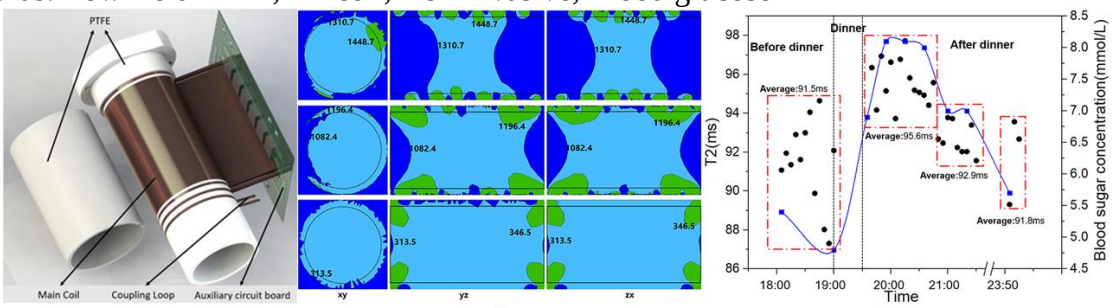

1a 1b 1c

Fig.1:(a)The schematic diagram of the T coil;(b) the RF field distribution of the three coils in xy, yz and zx plane;(c) Variation of transverse magnetic relaxation time T2 of human fingers as blood glucose concentration changes.

Effect of Radial Vibration on LWD NMR T_2 Distribution

Lin Hu, Lizhi Xiao, Guangzhi Liao, Yan Zhang
China University of Petroleum, Beijing, China.

Nuclear magnetic resonance (NMR) logging while drilling (LWD) represents a significant advancement in geosteering and formation-evaluation technology, bringing the benefits of wireline NMR to real time drilling operations. Researches have been made on how vertical motion affects wireline NMR T_2 spectrum [1]. However, there are few work about the influence of radial vibration on LWD NMR measurement. NMR LWD tool works under complex motion, and there are many factors affecting the logging responses. Due to the radial vibration, the magnetic field applied to the sample in the sensitive area is changing all the time, so it is necessary to study the nuclear magnetic resonance response in a non-uniform field [2]. With the knowledge of coherence pathways, the formula for calculating the echo amplitude in the non-uniform field is derived. Since the number of pathways and calculation amount increase sharply as the echo numbers increase, the formula needs to be optimized. With the absence of relaxation and diffusion, the magnetization vector in the non-uniform field will also decay. The echo decay in a non-uniform field is affected not only by T_2 but also by T_1, which is an attenuation factor consisting of $1/T_1$ and $1/T_2$[3].

$$M_{q_1,q_2,..,q_N} = \left(\prod_{k=1}^{N}\Lambda_{q_k,q_{k-1}}\right)\exp\left(i\Delta\omega_0\sum_{k=1}^{N}q_k t_k\right)\exp\left\{-\sum_{k=1}^{N}\left(\left(q_k^2/T_2\right)+\left(1-q_k^2\right)/T_1\right)t_k\right\}\times\left\langle\exp\left\{i\sum_{k=1}^{N}q_k\varphi_k\right\}\right\rangle \quad (1)$$

By establishing a radial vibration model of NMR LWD, the finite element method is used to divide the samples into small voxel, $\Delta\omega_0/\omega_1$ can be calculated by assuming that B_0 in every voxel is a fixed value. Then the total echo signal in each vibration state is obtained. The effects of vibration frequency, vibration amplitude and field gradient on echo signals are discussed separately, and a correction method is also proposed.

$$M_0 = \frac{\int_{z_1}^{z_2}\int_{r_1}^{r_2}\int_0^{2\pi}R_i(r,\varphi,z)rdrd\varphi dz}{V} \quad (2)$$

A shematic diagram of vibration is depicted(Fig. 1 a), where sensitive region is within arc s_1 and s_2. s is recorded by a displacement sansor. And the echo decay caused by vibration is also shown as below (Fig. 1 b).

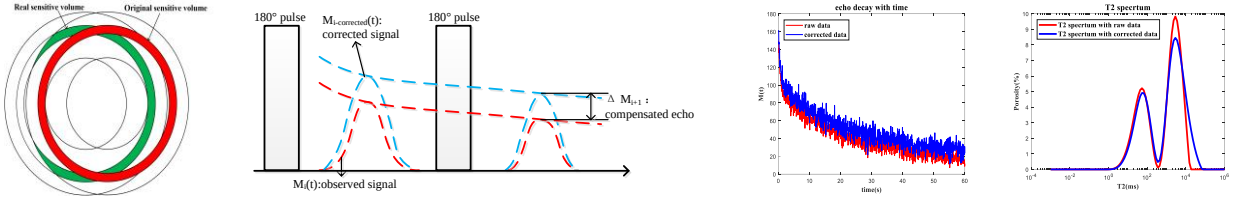

a b c d

Fig. 1 a: Schematic of radial vibration. b: Schematic of echo compensation. c: Decay of raw and correted data. d: T_2 spectrum of raw and correted data.

A correction coefficient $f_i(s)$ which is a function relationship of vibration displacement and field gradient can be derived:

$$M_{i-corrected}(t) = f_i(s)M_i(t) \quad (3)$$

Where s is the displacement, $M_i(t)$ is the ith observed amplitude and $M_{i\text{-}corrected}(t)$ is the corrected amplitude compensated by $f_i(s)$(Fig. 1 c). Next, a T_2 distribution can be inversed by BRD method with two data respectively(Fig. 1 d).

References

[1] Edwards C M. SPWLA 38th Annual Logging Symposium held in Houston(1997).
[2] Hurlimann, M. D., Journal of Magnetic Resonance(2000).
[3] Y.-Q. Song, Journal of Magnetic Resonance(2002).

A Magnet Design of Low Gradient for NMR LWD

Yifan Wang, Lizhi Xiao, Guangzhi Liao, Yan Zhang

State Key Laboratory of Petroleum Resonance and Prospecting, China University of Petroleum, Beijing, China

With the continuous expansion of the exploration and development scale of complex reservoirs and unconventional reservoirs, the nuclear magnetic resonance (NMR) logging technology for high-angle and horizontal wells has been widely used. However, the strong vibration of the instrument during drilling [1] reduces the signal-to-noise ratio (SNR) and produces an invalid signal. The low gradient static magnetic field will reduce the effect of radial vibration.

In this paper, the "Inside-out" [2] structure is the main magnet structure, and then the focusing magnet, the high magnetic permeability material and the combination of the focusing magnet and high magnetic permeability material are added respectively to design four magnet schemes. To obtain the resonance frequency of 500 kHz, the finite element [3] method is used to sequentially change the thickness, height and spacing of the magnetic material to numerically simulate the four magnet schemes and analyze the influence of various parameters on the distribution of static magnetic field. Then the structure of the main magnet, the focusing magnet and the high magnetic permeability material is optimized. Finally the low gradient is achieved. For example, as shown in Fig. 1, a) is the schematic diagram of radial static magnetic field intensity B_0 distribution of option one. b) is the schematic diagram of radial static magnetic field gradient G distribution of option one. D in Fig.1 represents vertical distance from the center of the instrument axis.

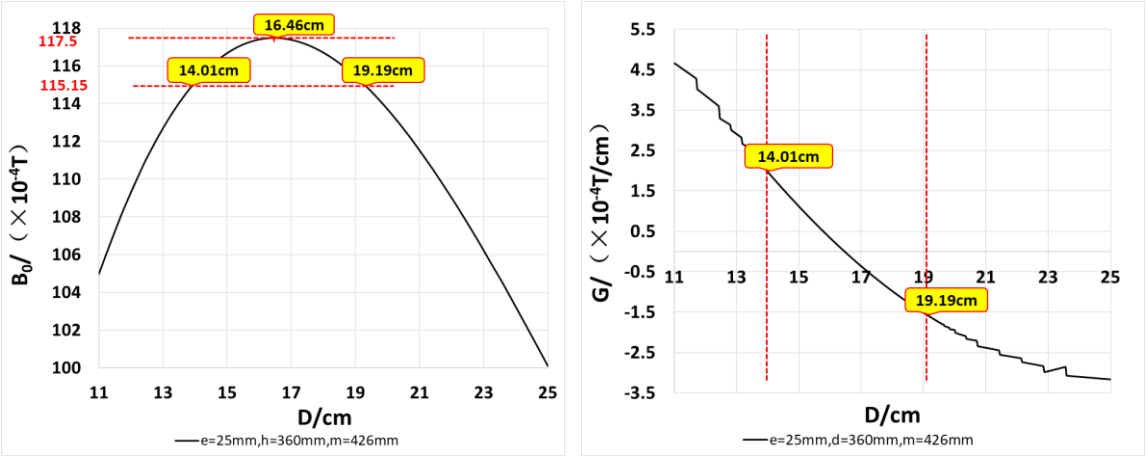

a) b)

Fig. 1: The illustrations of magnetic field simulation results

References:

[1] Morley J, Heidler R, Horkowitz J et al. Field testing of a new nuclear magnetic resonance logging-while-drilling tool. SPE Annual Technical Conference and Exhibition, 2002.

[2] Borghi M, Porrera F, Lyne A et al. Magnetic resonance while drilling streamlines reservoir evaluation. SPWLA 46th Annual Logging Symposium, 2005.

[3] An Ping, Yuzhong Gan, Yating Yu. Finite Element Method: Principle, Modeling and Application [M]. Beijing: National Defense Industry Press, 2004.

Studies of Biofilms in Yellowstone National Park and Violins of the Cremona Masters by Mobile NMR

Denis Jaschtschuk[a], *Christian Rehorn*,[a] *Michael Adams*,[a] *Bernhard Blümich*,[a] *Sarah Codd*,[b] *Catherine Kirkland*,[b] *Brent Peyton*,[b] *Joseph Seymour*[b], *Claudia Invenizzi*[c], *Marco Malagodi*[c], *Valeria Gabrielli*[d]

[a] RWTH Aachen University, Aachen, Germany

[b] Montana State University, Bozeman, Montana, USA

[c] Universita degli Studi di Pavia, Cremona, Italy

[d] Univerity of East Anglia, Norwich UK

Compact NMR instruments have evolved from mobile stray-field sensors to benchtop spectrometers suitable for nondestructive material testing and small-molecule research, respectively [1]. Stray-field relaxometers like the NMR-MOUSE [2] detect the dynamics of small molecules in materials. We have adapted the sensor developed over two decades ago to operate with a car battery and an electric generator in locations without access to the electric power grid. This enabled us to analyze the biofilms in Yellowstone National Park. The biofilm studies were motivated by the challenge to identify biofilms in the protected areas of hot springs, where bacteria proliferate with genetic information that may help to shed more light on the early evolution of life and research in areas such as astrobiology and biotechnology . Moreover, some of the famous master violins of the Amati, Guarneri and Stardivari families were analyzed in the Museo del Violino in Cremona and the Ashmolean Museum in Oxford as part of the MOLAB activities of the IPERION-CH project of the European Community. We found, that in addition to the thin varnish on the outside, thicker layers exist on some violins underneath the varnish and sometimes also the inner surface.

Figure 1. Setting up the measurement of a depth profile through the Cremonese violin made by Antonio Stradivari in 1715.

Figure 2. Setup for measuring a depth profile into a biofilm at a runoff of the octopus hot spring in Yellowstone National Park.

References

[1] B. Blümich, S. Haber-Pohlmeier, W. Zia, Compact NMR, de Gruyter, Berlin, 2014.

[2] G. Eidmann, R. Savelsberg, P. Blümler, B. Blümich, The NMR MOUSE, a Mobile Universal Surface Explorer, J. Magn. Reson. 122 (1996) 104-109.

The Frequency-switchable Transceiver Array with Inductive Decoupling

B. Wu, Y. Ha, C. Rogers III, K. Selvaganesan, G. Galiana, R. T. Constable
Department of Radiology and Biomedical Imaging, Yale University, New Haven, CT 06520, USA

Radiofrequency(RF) encoding using RF coils instead of gradient coils is attractive in developing low-field MRI system. Bloch-Siegert phase shift [1], as a novel RF encoding technique, was developed by Kartäusch for RF fields that generate linear phase modulation [2]. We have recently been working on Bloch-Siegert encoding for arbitrary RF fields for using in a portable tabletop MRI device [3].

In this study a transceiver array was built to generate the Bloch-Siegert fields and receive signal simultaneously. Excitation and refocus pulses were delivered from a volume coil. Off-resonance pulses were played from two coils in the 3x3 array while other coils in the array simultaneously received signal on resonance.

The key challenge is the isolation requirement between transmit elements at 870kHz and receive elements at 1MHz. Inductive decoupling technique [4], except geometric decoupling, was exploited to build the array coils. Coupling was adjusted by inductors for adjacent coils, while small loops were used to reduce coupling between coils that do not overlap. Figure 1 shows a 3x3-element coil array. Each octagonal coil with a 3D-printed structure consists of two turns of AWG16 wire. Cross-diodes were used to passively switch frequency: transmit power at 870kHz will turn on the diodes while diodes will be off when coils receive signal at 1MHz. Figure 2 shows the mutual coupling achieved when each coil was tuned to resonance at 1MHz.

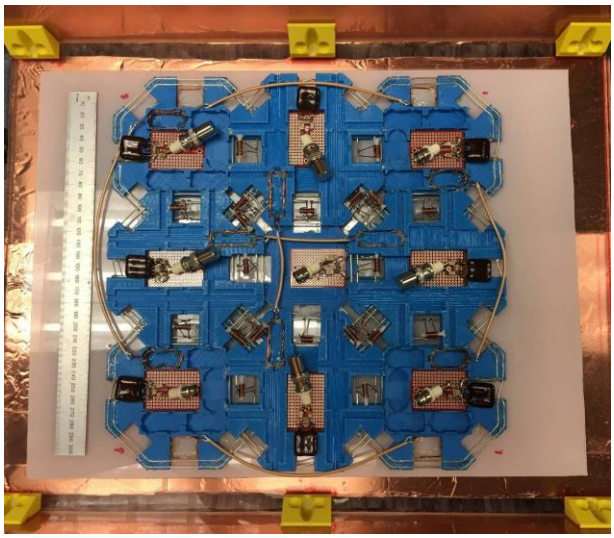

Figure 1 Octagonal structure with 3D-printed support.

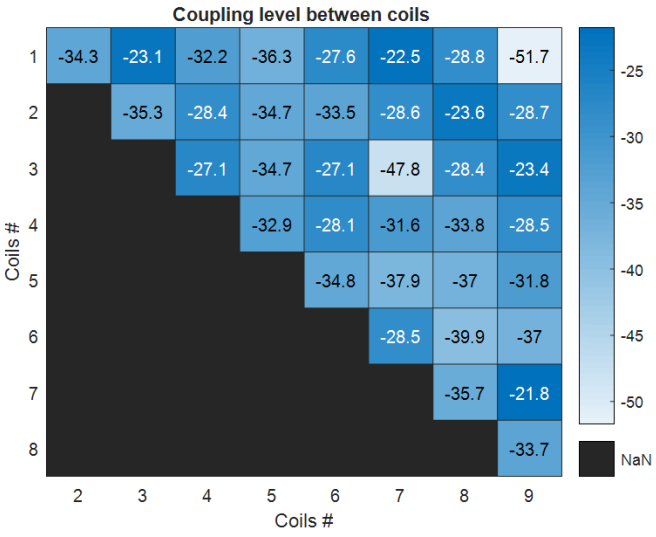

Figure 2 The measured mutual coupling between coils.

References:

[1] F. Bloch, A. Siegert, Phys. Rev. (1940). [2] R. Kartäusch, et al., MAGMA, (2014). [3] B. Wu, et al., ENC (2019). [4] F. E. Terman, Radio engineering (1937).

Mini Inside-Out Nuclear Magnetic Resonance Sensor Design for Soil Moisture Measurements

Jiamin Wu, *Yucheng He*, *Zheng Xu*
State Key Laboratory of Power Transmission Equipment and System Security and New Technology
Chongqing University, Chongqing, China

Introduction: The improvement of water management in agriculture by exactly detecting moisture parameters of soil is crucial. However, investigating such parameters is time-consuming and invasive in many cases. Thus, a fast and noninvasive approach is required to examine the moisture parameters of soils. In order to investigate this problem, a mini sensor was proposed to measure moisture parameters of model soils. We measured the water content of sandy soil with small particle diameter and silica sand with large particle diameter.

Methods: This sensor combines three cylindrical magnets that are magnetized in the axial direction and three arc spiral coils of the same size in series [1,2]. We calculated and optimized the magnet structure by equivalent magnetization to current density. The main magnetic field with constant gradient in toroidal region of interest.

Results: By adjusting the radius and height between the cylinders, a circumferential symmetric constant gradient field (2.28 T/m) was obtained. We selected sandy soil and silica sand with water to prepare an experimental sample, and then we measured them through Carr–Purcell–Meiboom–Gill (CPMG) measurements and weighing analysis to determine the moisture content of this sample. The CPMG decays are analyzed in terms of multiple exponential fitting

$$y(t) = \sum_{j=1}^{m} f(T_{2j}) e^{-t/T_{2j}} + \xi(t) \qquad \text{Eq. 1}$$

where $y(t)$ is amplitude of CPMG signal at t, $f(T_{2j})$ is the amplitude of component with transverse relaxation time T_{2j}, $\xi(t)$ is stochastic noise, m is the number of relaxation components, and T_2 spectrum curve is the relationship between T_2 with $f(T_2)$. The integral area (A_{peak}) of peak in T_2 spectrum curve can be expressed as

$$A_{peak} = \int_{T_{2\min}}^{T_{2\max}} f(T_2) dT_2 \qquad \text{Eq. 2}$$

Moisture content of the sample is positively correlated with the integral area of T_2 spectrum peak (Apeak); T_2 of the water in small pores is shorter than that in large pores, because the movement of water molecules are limited by the inner wall of the pores. The sensor is capable of detecting moisture both content and pore size of the sample. This mini sensor (4.0 cm in diameter and 10 cm in length) is portable, and the lowest measurable humidity is 0.38%. This sensor will allow easy soil moisture measurements on-field in the future.

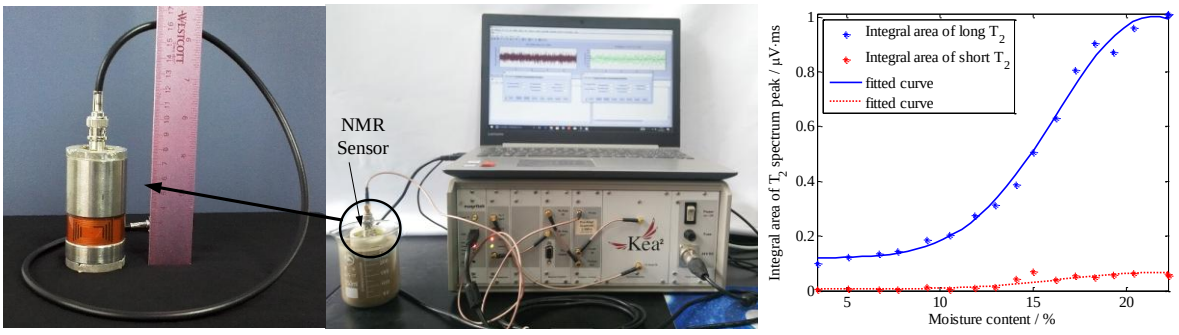

Fig.1 Measurement system (left) and correspondence between the integral area of the T_2 spectrum with the moisture content of the silica sand (right).

References: [1] Guo Pan, Trans. China Electrotech. Soc. (2016). [2] Jiamin Wu, Sensors. (2019).

NMR depth profiling as prerequisite for restauration and conservation of Cultural Heritage

M. Gierth, M. Küppers, B. Blümich
ITMC, RWTH Aachen University, Aachen, Germany

Introduction:

To examine objects of cultural heritage several methods can be applied. Almost all of them return information from a single spot or an image of the surface. Only very few methods offer the possibility to read information of the object from layers below. Less than a handful of those methods is non-destructive and is applicable to objects of arbitrary size. Depth profiling with the NMR-MOUSE® is one of them [1]. The use of this method is demonstrated by example of measurements in the church St. Ayoul in Provins, France, and on treated stone samples.

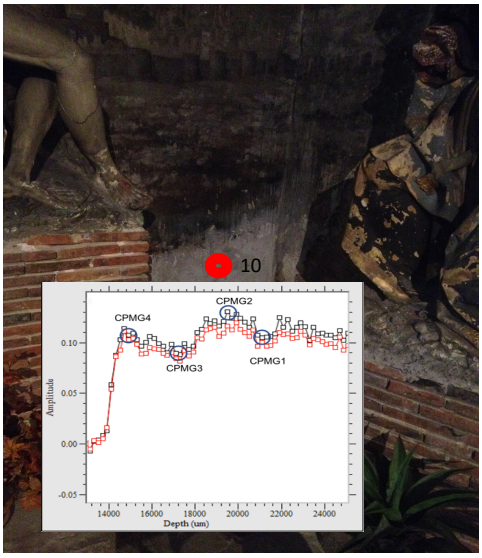

Fig. 1: One of the measurement points in the church of St. Ayoul with the depth profile of the indicated measurement spot. Points of high interest where selected to perform more detailed measurements.

Method:

The stray-field NMR sensor used in this work is the PM25 NMR-MOUSE® by Magritek equipped with a remote-controlled motorized lift and a Kea² spectrometer [2]. The lift allowed automated measurements at different depths. In the church of St. Ayoul in Provins the lift system was also used to focus on layers of high interest at different measurement spots of an altarpiece (Fig. 1). Moreover, mock-up samples of sandstone were treated with different agents of interest in stone consolidation work. Prior to measurement the samples were submerged into water to give good contrast between treated and untreated areas (Fig. 2).

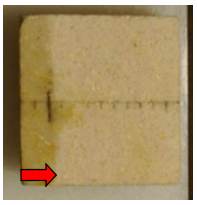

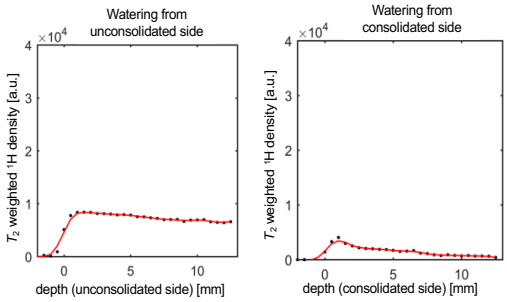

Fig. 2: One of the sandstone mock-up samples measured once form the side with applied consolidant and once from the opposite side without any treatment.

Outlook:

A set of training schools and dissemination events in the frame of the CHARISMA CH project introduced the NMR depth profiling techniques to the cultural community [3], where the demand for use of this analytical technique is increasing. Improvements to the method and instrumentation are needed to simplify the setup, operation and data analysis.

References:

[1] Blümich, Compact NMR (2014).
[2] Perlo, J. Magn. Reson. (2005).
[3] Blümich, in: Batisdas, Cano, eds., Springer Nature (2018), pp. 61-76

Toward Inexpensive Magnetically Compensated Materials

Andrew F. McDowell, *Fred W. McDowell*
NuevoMR, LLC, Albuquerque, NM, USA

Introduction: Designs for achieving high resolution in permanent magnets exist and are actively being commercialized. However, these devices require specialized materials and methods that are out of reach for the low-budget researcher. In recent years we have had success in developing cost effective, space efficient methods for active and passive shimming, leading to magnets with calculated line widths in the 10 ppb range. Now we are focused on probe making methods and materials, for example, low-cost ways to produce magnetically compensated wires and glues. Here, we review recent and on-going work.

Context: Recent Work on Shims: Our active shim design [1] is mainly aimed at reducing the amount of space required by the shims, which in turn allows magnets to have smaller gaps, reducing size, weight, and cost. We have demonstrated 4th order shims built in a space 0.5 mm thick. We use an automated shim adjustment procedure developed by Carl Michal. Our passive shim methods [2] rely on two ideas: utilizing magnetic ink to produce the shims at virtually continuous strength values, and designing the shims by calculating superpositions of large, extended patterns. We have demonstrated correction of magnets from roughly 100ppm to 1-2 ppm total peak to peak variation over large ROIs (~50% of the magnet gap). These passive shims are remarkably thin and can be made rapidly using commonly available materials.

New Work: Compensated materials: Due to its close proximity to the sample and finite length, the NMR detection coil has a substantial negative impact on the field homogeneity across the sample volume. The copper wire used to make the NMR coil has a volume susceptibility of about -10 ppm, as do most adhesives. A solution to these problems can be found in very early NMR patents[3], where the glues were doped with paramagnetic materials and wires were given paramagnetic cores of Pt. Doty [4] has published modern versions of these methods, as well as a well-conceived method for making the required measurements. They also offer compensated wires with aluminum cores at diameters 0.53 mm and up. This is too large for our purposes, and other solutions involving plating of exotic metals are beyond our reach, so we are developing our own methods.

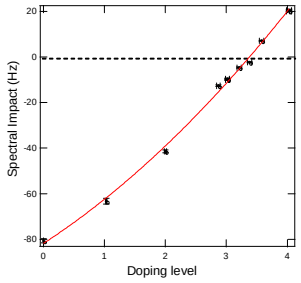

Fig.1: Compensation of glue

For example, we have developed a doped epoxy formulation that is nearly 100% compensated. We determine this level of compensation by inserting glue samples into the interior space of a pair of nested NMR tubes and monitor the effect on the linewidth. The results showing the compensation are in Fig. 1. We have also begun making aluminum-core copper wire in diameters down to 125 μm. The required measurements are challenging, due to the small amount of material in the samples. Fig. 2 shows measurements for 250 μm diameter Al-core wires.

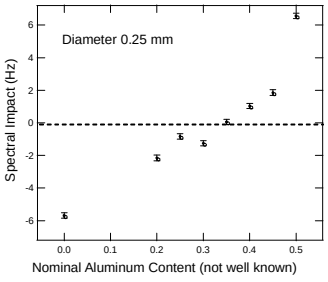

Fig 2. Aluminum-core wire

Conclusion: We are continuing to make progress in developing simplified and cost-effective methods and materials required for the production of high-resolution probes, which should allow us to fully utilize our recent advances in shimming.

References: [1] McDowell and Conradi, *J. Magn. Reson*. **296,** 143 (2018), McDowell, US Patent 9,285,441. [2] McDowell, *J. Magn. Reson*. **296,** 143 (2018). [3] Anderson, US Patent 3,091,732 (1963). [4] Doty, et al, *Concepts Magn. Reson*. **10**, 133 (1998).

A Movable MRI system for brain imaging and its pre-clinical experiments

He Yucheng[1], *Xu Zheng*[1], *Wu Jiamin*[1], *Tan Liang*[2]

[1]Chongqing University, Chongqing, China, [2]Southwest Hospital, The Third Military Medical University, Chongqing, China

Introduction: Cerebrovascular disease is highest mortality rate disease beyond cancer in China [1]. There have effective non-radiative imaging system in the clinical to observe the disease progression of stroke patient. In this paper, we built a movable and lightweight MRI system for brain imaging, and we did a few pre-clinical experiments for the diagnosis of stroke patients. This system has advantages in weight, cost, magnetic shield compare to high field MRI system.

Method: The magnet of MRI system was a H-type permanent magnet shown in Fig. It weighs 300kg. Larmor frequency was 2.167MHz (corresponding 50mT). It was a compromise scheme for weigh and magnetic field strength. SmCo rare earth was chosen as permanent magnet block because its high stability of temperature. Target field method was used to design X/Y/Z gradient coils. The structure of RF transmitting coil was shown in Fig. 1, and particle swarm optimization method was applied to optimize the structure parameters of coil. RF receiver coil was a solenoid coil suited for human head shape.

Considering the low SNR (signal to noise ratio) of this system, T1WI(T1 weighted imaging) was acquired by 3D gradient recalled echo sequence, and T2WI acquired by fast spin echo sequence.

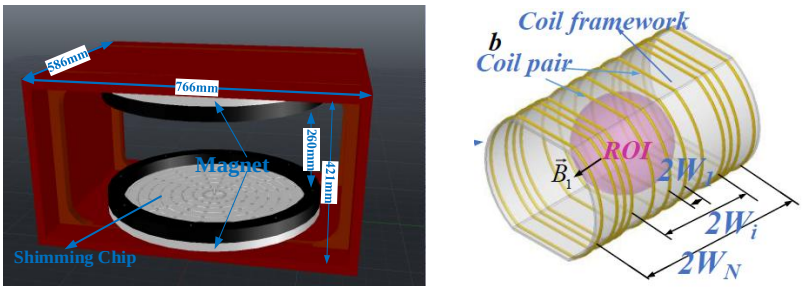

Fig 1: a) the structure of H-type permanent magnet; b) the structure of RF transmit coil

Results and discussion: The lightweight MRI system was set in the sixth floor of the first affiliated hospital of The Third Military Medical University (China). T1WI and T2WI was shown in Fig. 2. The lesion location, size can be observed in T1WI (hemorrhage) and T2WI (cerebral infarction). But the SNR of imaging is not desirable,

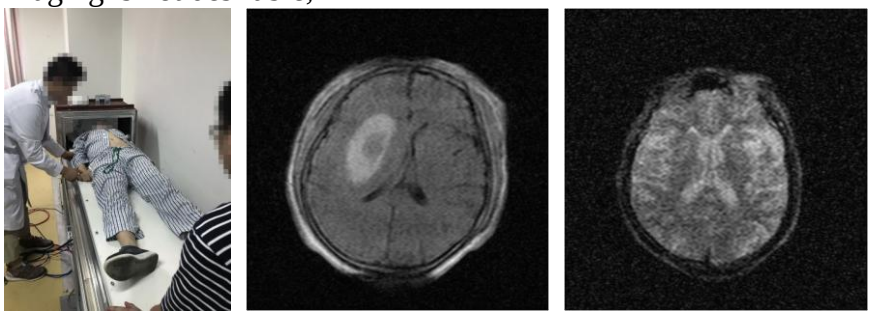

Fig. 2: a) actual condition of pre-clinical experiment in patients; b) the T1WI of hemorrhagic stroke patient (FOV is 260mm, slice thickness 10mm, matrix is 128*176); c) the T2WI of ischemic stroke patient (FOV is 260mm, slice thickness 10mm, matrix is 128*176)

Conclusion: This MRI system can effectively locate the lesion of some brain disease. Also it can be used to the other field which traditional high field MRI cannot reach, such as first aid, remote districts etc.

References: [1] Zhou M, The Lancet (2016). [2] Liu W, J. Phys. D Appl. Phys. (2007).

CPMG measurement under motion

Shin Utsuzawa, Irfan Bulu, Tancredi Botto, Jeffrey Paulsen, Martin Hürlimann, Yi-Qiao Song
Schlumberger-Doll Research, Cambridge, MA 02139, USA

NMR is typically performed with the detector and the sample in a fixed relative position. In NMR well logging, on the other hand, the detector moves continuously with respect to the sample (i.e., rock formation). Fast movement causes the sample to move out of the detector's sensitive volume during a CPMG measurement and thus induce additional signal decay, which can be mitigated by using multiple coils to capture the signal from the escaping portion of the sample [1]. Another source of signal decay is the variation of magnetic fields during a CPMG measurement; motion along the magnetic field gradient introduces fluctuating fields for the spins, resulting in the change of effective rotation for each CPMG cycle [2]. Therefore, it is crucial to understand the behavior of CPMG signal to perform quantitative measurements under motion.

Figure 1 shows a laboratory setup to mimic logging conditions. The sample bottle containing DI water was moved along the magnet at various speeds. Resulting CPMG echo amplitudes were plotted as a function of travel distance to distinguish gradient-induced signal decay from volumetric signal decay. When t_E is small, signal decays at the same rate regardless of motion speed (Fig. 2(a)). This behavior is described by convoluting B_1 profile with the sample profile $\Phi(r)$ over length L:

$$S(L) = (B_1 * \Phi)(L) = \int_0^L B_1(r) \cdot \Phi(L-r)dr$$

When t_E is increased, signal starts to decay faster at some point (Fig. 2(b)). This is caused by a transition from adiabatic (i.e., perfect tracking of field variations) to non-adiabatic regimes and dictated by the instantaneous value of B_0 offset and its temporal derivative [2]. Therefore, the magnet must be designed to comply with these limits to perform quantitative measurements under motion.

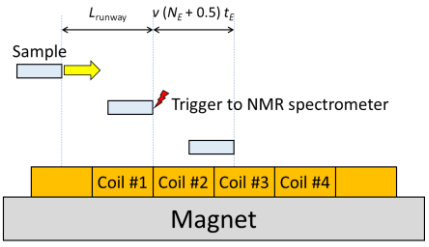

Fig. 1. Laboratory setup to mimic logging conditions. The magnet is 117 cm long and produces B_0 = 425 +/- 1.2 G at the saddle point. Four identical RF coils (17 cm long each) mounted on the magnet produce B_1 = 1.3 +/- 0.15 G. The sample bottle is 12 cm long and mounted on a linear translation stage that moves at a speed v. A trigger signal is generated to initiate a CPMG measurement when the sample reached to the edge of the coil.

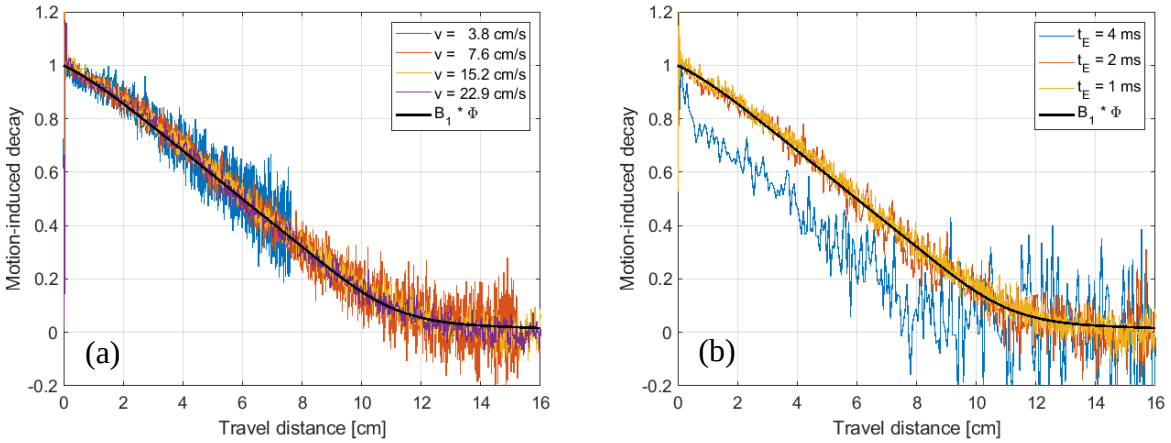

Fig. 2. Motion-induced signal decay observed by Coil #1 at (a) t_E = 1 ms and (b) v = 15 cm/s. The effect of diffusion was removed by dividing the data obtained under motion with that under static conditions (v = 0) with the same t_E.

References:

[1] Y.-Q. Song et al., "NMR with a fast-moving coil array", 15th ICMRM (2019).
[2] M. D. Hürlimann, S. Utsuzawa, C.-Y. Hou, arXiv:1903.08006 (2019).

Profiling the temperature dependent frequency of a MOUSE® for outlab MRI

A. Traore, R. Alouissi, A Benmoussa, G. Pagès, JM Bonny
AgroResonance, UR0370 QuaPA, INRA, Saint-Genès Champanelle, France

Introduction: The open geometry of the single-sided NMRMOUSE® (Magritek®, Aachen, Germany) sensor results in a powerful spectrometer to characterize arbitrarily sized samples. This inhomogeneous magnet is designed in such a way that generates a highly flat sensitive volume, i.e. the measurement volume, parallel to the scanner surface [1]. It is well known that low field magnets have a strong dependence between the magnetic field and the magnet temperature, resulting for the NMR MOUSE® in a dependence between the (magnet) temperature and the position (depth) of the measurement volume [2]. As our aim is to use this portable device *in-situ* to study plants in their living environment, we anticipate seasonal temperature variation of the working environment. This study aimed at characterizing the temperature dependence of the magnetic field, and hence the shift in the prescribed measurement depth.

Methods:
All the experiments were conducted in a climatic room allowing precise control of the temperature in the 10-25°C range with the NMR MOUSE® PM25 -corresponding to the measurement volume at 25 mm of magnet surface- inside. A fiber optic temperature control unit (Lumashield, LumasensInc®) was used to record temperatures each 2 min. Three sensors were used: one in the room at the immediate vicinity of the NMR MOUSE®, one between the magnet blocks and one in the sample. Two temperature cycles, namely from 10°C to 25°C and from 25°C to 10°C were used. The protocol consisted in continuously acquiring the signal profile of the doped-water in the Petri dish from 6000 to 0 µm (from the surface of the spectrometer) with a resolution (measuring volume) of 50 µm. This resulted in a total of 121 points per profile and 8 min of acquisition time. With a gap of 2 min between successive profiles, each profile then corresponded to five temperature points. Taking into account the dish thickness, the shift in the measurement depth was measured by the depth at which the signal disappeared. Correlating this variation with the temperature changes allowed correlating the temperature variation with the magnetic field.

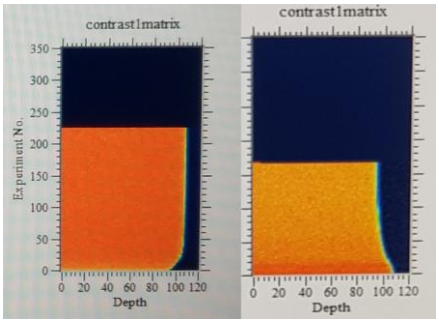

Fig. 1: Cumulative profiles recorded for 25°C -> 10°C (left) and for 10°C -> 25°C (right) showing the temperature dependence of the measurement depth

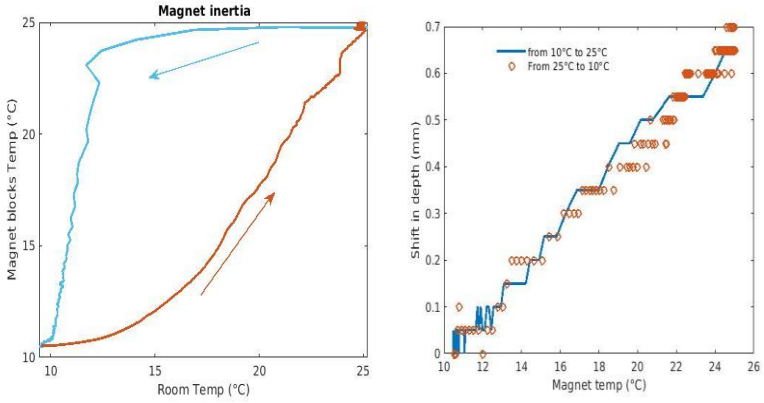

Fig. 2: (Left) the evolution of the magnet temperature in the function of room temperature during the two cycles. (Right) Temperature dependence of the position of the sensitive volume for the two cycles

Results and discussion:
Fig. 1 shows the cumulative profiles recorded for 25°C to 10°C (left) and for 10°C to 25°C (right). These figures clearly show the displacement of the measurement depth at the beginning of each temperature cycle. The great thermal inertia of the magnet blocks is clearly shown in the Fig 2 left by the decorrelation of their temperature evolution to those of the room. A linear variation of position of the sensitive volume is observed with a net displacement of 650 µm when comparing the two temperature bounds (Fig 2 right). The temperature compensation tacking into account this linear dependence along with the magnet inertia is then being developed.

Conclusion: Despite the noticeable thermal inertia of the magnet, the observed linear displacement of the measured volume has to be take into account when considering measurements outside the lab.

References: [1] J. Perlo, et al. J. Magn. Reson. 176 (2005)

Magnetic Particle Spectroscopy – MObile Universal Surface Explorer

P. Vogel [a], *M.A. Rückert* [a], *T. Kampf* [b], *V.C. Behr* [a]

[a] Experimental Physics 5 (Biophysics) Universität of Würzburg, Germany

[b] Diagnostic and Interventional Neuroradiology, University Hospital Würzburg, Germany

Introduction: Magnetic Particle Spectroscopy (MPS) is a modality to extract specific parameters from superparamagnetic iron-oxide nanoparticles (SPIONs) samples. It is based on the nonlinear magnetization response to time-varying magnetic fields. MPS can be utilized to study the dynamic behavior of SPIONs [1], and to extract SPION-specific parameters, such as the Néel- or Brown-relaxation times, which can be used to enhance the quality of reconstruction results in Magnetic Particle Imaging (MPI) [2, 3]. The MPS MOUSE (MObile Universal Surface Explorer) is a handheld device that will provide MPS access to many researchers through its ease of use, robust design and mobility as well as its flexibility.

Methods: MPS devices typically consists of a transmit coil (tx) for generating a strong alternating magnetic field, a receive coil (rx), an amplifier and a control and evaluation unit. The MPS MOUSE (Fig. 1 a, b) provides a tx-rx system, which can be used for multiple applications offering different sensitive areas simultaneously. E.g. measuring Eppendorf tubes with field of view I (FOV) and/or petri-dishes with FOV II. The tx-rx system consists of a planar transmit coil and several receive coils assembled in a gradiometer design (Fig. 1 c). A novel pulse amplifier based on a resonant circuit design is used to produce a short strong magnetic field up to 50 mT and stronger at the top of the scanner. For control and data acquisition, a microcontroller (PSoC 5LP, Cypress, USA) is used, which can be controlled via Bluetooth by a mobile computer [4]. For a higher sensitivity, an active cancellation technique is used to suppress residual excitation signals. The host software offers several measurement modes such as single-measurements as well as point-by-point surface scanning to obtain spatially resolved spectroscopic information.

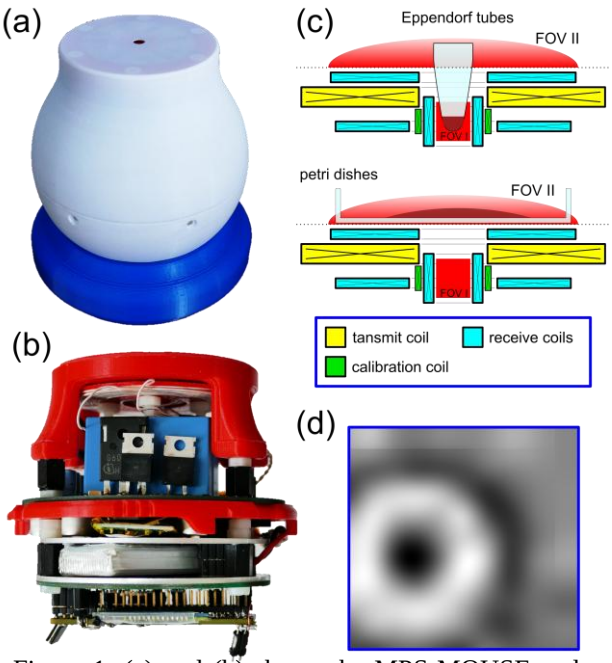

Figure 1: (a) and (b) shows the MPS-MOUSE and the hardware components inside. (c) Sketch of the tx-rx system offering two measurement areas (FOV I and FOV II). (d) Image of a point-by-point scanned 2D ferromagnetic sample.

Results and Discussion: In Fig. 1 d an initial experiment with the MPS-MOUSE prototype is shown demonstrating a scanned 2D surface containing a circular-shaped ferromagnetic sample (diameter 10 cm). The magnetic field strength is 29.5 mT at a frequency of 20.3 kHz, the acquisition time is 1 ms for each step (10×10 gridsize) at a sampling rate of 2 MS/s. The image shows the magnitude distribution of the third harmonic.

Conclusion: The presented prototype of the MPS MOUSE demonstrates the functionality (pulse operation for magnetic field generation, data acquisition, data transfer, evaluation routines, etc.), robustness and stability of the proposed system and is used as test bed for validation and further system integration and development. In first experiments, the flexibility measuring small samples as well as spatially resolved larger 2D distributions of SPIONs could be demonstrated.

References: [1] Biederer, J Phys D (2009). [2] Gleich & Weizenecker, Nature (2005). [3] Knopp, PMB (2017). [4] Rückert, Proc on IWMPI #8 (2018).

Low-field Magnet Assemblies for *in operando* NMR Studies

R. de Oliveira-Silva[a], J. Marreiros[a], A. G. Araujo-Ferreira[b], E. Lucas-Oliveira[b], P. Judeinstein[c,d], W. A. Trevizan[e], J-M. Zanotti[c], T. J. Bonagamba[b], R. Ameloot[a] and D. Sakellariou[a]

[a]cMACS, Department of Microbial and Molecular Systems (M²S), KU Leuven, Leuven, Belgium.
[b]São Carlos Institute of Physics, University of São Paulo, São Carlos, SP, Brazil.
[c]Laboratoire Léon Brillouin, CEA Saclay, Université Paris-Saclay, Gif-sur-Yvette, France.
[d]Laboratoire de Physique des Solides, Université Paris-Sud, Université Paris-Saclay, Orsay, France.
[e]Cenpes/Petrobras, Rio de Janeiro, Brazil.

Introduction: High-field NMR is an extremely powerful characterization technique, which cannot be trivially adapted to perform in *in operando* and *in situ* studies on technological materials like porous solids. Limitations regarding space, radio-frequency compatibility, transportability and maintenance are some of the difficulties that one has to overcome. On the other hand, low-field NMR makes use of permanent magnets which are more versatile in size and design, circumventing some of the abovementioned issues.

Methods: Using a general magnet design methodology [1,2] we present a variety of new permanent magnet assemblies, which offer innovative opportunities for material characterization *in operando*. Small and large single-sided systems having unique field profiles simulating NMR logging tools were designed and built. We have also built new enclosed ultra-light pseudo-Halbach magnets producing highly homogeneous sweet-spots, offering excellent portability. Experimental characterization of the sweet-spot and use of adiabatic pulses provide a high-definition localization [3] which, combined with temperature stabilization, produces robust and experimentally reproducible systems.

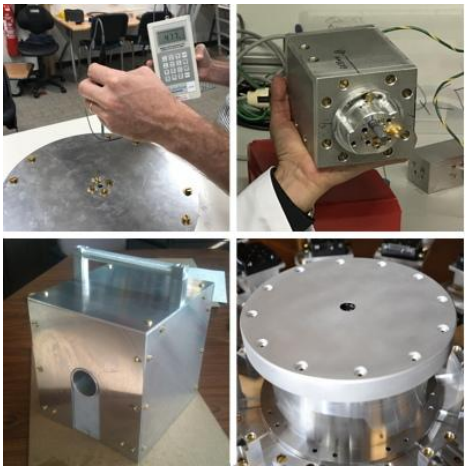

Fig. 1: New permanent low field NMR magnet assemblies for *in situ*, *in operando* hyphenated applications.

Results and discussion: These NMR systems have been used as standalone desktop analyzers for the study of pore size distributions in rock analysis, or as single-point imaging systems. Here we have used them also simultaneously with other characterization modalities (physisorption devices, neutron scattering and imaging stations), in hyphenated low-field NMR approaches for *in operando* and *in situ* physico-chemical characterization of solid materials [4]. Applications on microporous materials (metal organic frameworks - MOFs, zeolites) are demonstrated, where sorption of vapors of small molecules in natural abundance are monitored *in operando*, recording relaxometric information as a function of loading pressures. This information shows the complementarity of NMR to the sorption experiments, revealing its dynamics in a direct and totally new manner. Finally, we will show some initial results in heteronuclear magnetic resonance of metals at low magnetic field using our home-made NMR sensors. This effort can potentially offer great benefits especially in NMR of metals in materials such as batteries and catalysts.

Conclusion: Low-field hyphenated NMR instrumentation demonstrates sufficient generality and practicality, confirming their potential for dedicated industrial applications.

References: [1] Hugon *et al.*, J Magn Reson. (2012), [2] P. Judeinstein *et al.*, J. Magn. Reson. (2017), [3] Oliveira-Silva *et al.* in preparation (2019), [4] Oliveira-Silva *et al.* in preparation (2019).

Utilization of Time Domain (TD) and Fast Field Cycling NMR Relaxometry To Quantify Crystallization and Corn Syrup Adulteration on Honey

Berkay Berk[a], Mecit Halil Oztop[a], Ioan Ardelean[b], Leonid Grunin[c], Sirvan Sultan Uguz[a], Eda Ceren Kaya[a] , Selen Guner[a]

[a]Middle East Technical University, Ankara, Turkey
[b]Technical University of Cluj-Napoca, Cluj-Napoca, Romania
[c]Volga State University of Technology, Dept. of Phys., Yoshkar-Ola, Mari El, Russian Federation

As consumers are paying more attention to reduce calorie intake from sugar sources such as corn syrup or beet/cane sugar, use of honey in diets increased due to its additional benefits in addition the sweetening effects. Consequently, honey prices have risen and that lead manufacturers to adulterate honey to produce more at a cheaper price [1]. Corn syrup which is obtained by hydrolysis of starch is the main adulterating agent used in honey. One of the important features of corn syrup addition to honey is that it would prevent crystallization of glucose (an important component of honey ~31%) as it contains some hydrolysis remnants which would inhibit crystallization. Since the crystallization tendency of corn-syrup adulterated honey is expected to be lower, comparing this behavior of honey samples could predict the adulteration. In this study, different NMR Relaxometry approaches were tested for this purpose. First of all, as the conventional TD-NMR techniques T_1 and T_2 relaxation times were measured with a 20.35 MHz system (Spin Track, Resonance Systems, Germany) with respect to different corn syrup concentrations at a range of (2%-50%). A biexponential fitting was applied to the data. Seeding from an already crystallized honey was also applied to fasten crystallization and crystallization was monitored for 96 hrs. Secondly, for the same samples a modified Solid Fat Content (SFC) experiment was conducted by using a magic sandwich echo (MSE) pulse sequence to determine the amount of crystals present in honey during storage at 14 ^{o}C and during crystallization with seeding. This solid echo sequence was confirmed to be used to follow the crystallization kinetics in sucrose samples without using an F factor or an K inhomogeneity factor as described by other researchers [2]. Moreover Magic Sandwich Echo (MSE) sequence was recently shown to predict the crystallinity in powder sugar samples and thus similar approach was followed on honey samples [3]. And as the last technique in the study, FFC NMR Relaxometry was performed by measuring relaxation rates ($1/T_1$) with an FFC- Relaxometer working at a frequency range of 10 kHz-10 MHz (Smart Tracer, Stellar, Italy). NMRD dispersion profiles showed different behavior with corn syrup addition. Data were further analyzed with different models to explain the relaxation behavior of adulterated honey samples. Results showed that FFC NMR Relaxometry could be a tool for identifying the presence of corn syrup in honey samples. In addition, TD NMR results showed that, T_1 and T_2 were also changing wrt corn syrup addition and MSE sequence further quantified the presence of crystals with storage time. Thus, MSE based SFC sequence could be proposed as method to quantify crystallization and indirectly predict adulteration of honey samples.

References:

[1] R. de O. R. Ribeiro, E. T. Mársico, C. da S. Carneiro, M. L. G. Monteiro, C. C. Júnior, and E. F. O. de Jesus, J. Food Eng. **135**, 39 (2014).
[2] A. E. Dejong and R. W. Hartel, J. Food Eng. **178**, 117 (2016).
[3] L. Grunin, M. H. Oztop, S. Guner, and S. F. Baltaci, Magn. Reson. Chem. (2019).

Acknowledgment: This study was funded by The Scientific and Technological Research Council of Turkey (TUBITAK) with grant # 217O089. Moreover Sirvan Sultan Uguz and Eda Ceren Kaya got travel funding from the Short Term Scientific Mission (STSM) program under COST action : CA15209 EURELAX - European Network on NMR Relaxometry - (http://www.cost.eu/COST_Actions/ca/CA15209) to conduct FFC Relaxometry experiments at the Technical University of Cluj-Napoca, Romania.

Should we still fit quantitative MRI data to mathematical models in the age of AI?: A case study comparison of deep learning versus the Tofts model

Peter Q. Lee[2], Alessandro Guida, Steve Patterson, Thomas Trappenberg, Chris Bowen, Steven Beyea[1], Jennifer Merrimen, Cheng Wang, Sharon Clarke

[1]Faculty of Computer Science, Dalhousie University, Halifax, NS, Canada,

[2]Biomedical Translational Imaging Centre, IWK Health Centre, Halifax, NS, Canada

[2]Department of Diagnostic Radiology, Dalhousie University, Halifax, NS, Canada

Introduction:

We showcase a study that compares two deep learning models tasked to perform prostate tumor (PCa) segmentation. One model is trained end-to-end using Dynamic Contrast Enhanced (DCE) Magnetic Resonance Imaging [1]. The concentration of contrast agent within the bloodstream throughout time may behave differently in abnormal tissue [2]. The second model is instead trained with the Tofts pharmacokinetic model [3], one method for analyzing DCE that fits scalar parameters, such as K_{trans}, to the time-series [2]. We hypothesize that a fully end-to-end machine learning models that spatially and temporally interpret the raw DCE time-series will segment PCa better than baseline models that use K_{trans}.

Methods:

The training dataset is composed of 16 patients that were referred for prostate MRI and subsequently underwent radical prostatectomy. An abdominal radiologist manually annotated tumor regions according to PIRADS v2. Annotated DCE images from patients were sequentially transformed into K_{trans} maps. Two experiments are performed, both tasked with segmenting the tumor regions from non-tumor regions in PCa images. The first one uses U-net [4] and K_{trans}. The second uses a novel architecture that combines U-net and convGRU architectures (named UconvGRU) to perform the segmentation in both spatial and temporal domain. The latter model is designed to process the DCE time-series images. The models were trained using DICE score [5]. Model evaluation was performed using leave-one-out-cross-validation and the overall score calculated through averaging. Significance was tested with exact one-sided Wilcoxon test.

Results and discussion:

The results of the tumor versus non-tumor segmentation task can be visualized as prediction heatmaps. The model trained with DCE images (F1 score 0.22) significantly outperforms (p-value 0.042) the model trained with Ktrans maps (F1 score 0.18).

Conclusions:

Deep learning is changing the way models are built in the biomedical field. The results from the work presented, indicate that an end-to-end approach, without any previous pharmacokinetic physiological knowledge, can outperform models that rely on well studied mathematically engineered features. This presents the main advantage that, with enough data, features can be learned directly from the raw data. Feature engineering will still find many applications, especially when the problem complexity is very high and data availability is a limiting factor; but will eventually be taken over by fully end-to-end approaches.

References:

1. O'Connor, J. P. B. *et al.* Dynamic contrast-enhanced imaging techniques: CT and MRI. *Br. J. Radiol.* **84**, S112–S120 (2011).

2. Weinreb, J. C. *et al.* PI-RADS Prostate Imaging – Reporting and Data System: 2015, Version 2. *Eur. Urol.* **69**, 16–40 (2016).

3. Ronneberger, O., Fischer, P. & Brox, T. U-Net: Convolutional Networks for Biomedical Image Segmentation. *ArXiv150504597 Cs* (2015).

4. Tofts, P. S. T1-weighted DCE Imaging Concepts: Modelling, Acquisition and Analysis.

5. Milletari, F., Navab, N. & Ahmadi, S.-A. V-Net: Fully Convolutional Neural Networks for Volumetric Medical Image Segmentation. *arXiv:1606.04797 [cs]* (2016).

An Image Quality Metric Based Heuristic for Accurate Pharmacokinetic Parameter Recovery using Quantitative MRI

A. Mason[1], N. Murtha[2], J. Rioux[1,3], S. Clarke[1,3], C. Bowen[1,3], and S.D. Beyea[1,3]
[1]Dalhousie University, Halifax, Canada, [2]Carleton University, Ottawa, Canada, Biomedical Translational Imaging Centre (BIOTIC), Halifax, Canada

Introduction – Dynamic Contrast Enhanced (DCE) MRI is a useful tool for measuring physiological parameters using a pharmacokinetic (PK) model such as the Tofts model [1]. A fundamental problem when imaging dynamics is the trade-off between image quality and temporal resolution – i.e. under-sampled images exhibit high artifact/noise levels, and fully sampled images exhibit contrast washout due to temporal averaging over the acquisition window. Objective image quality metrics (IQMs), such as structural similarity (SSIM [2]) allow for the automatic assessment of image quality. We hypothesize that IQMs of golden-angle sampled dynamic data reconstructed with varying under-sampling factors will exhibit a relationship with the Tofts PK parameter accuracy determined from the images.

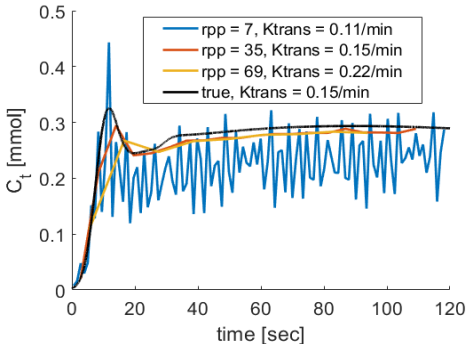

Fig. 1: DCE Time courses for three temporal resolutions defined by the number of rays per phase (rpp) with the recovered K^{trans} value.

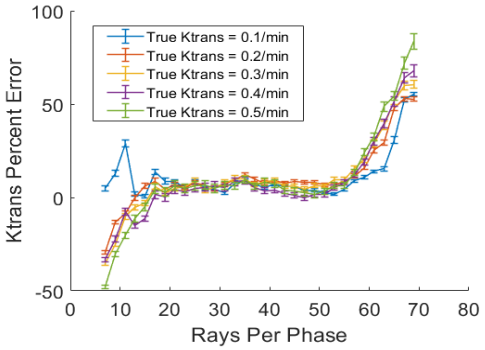

Fig. 2: Relationship between rays per phase and the percent error of the recovered Ktrans

Methods – To test this hypothesis, a 3D numerical phantom was generated in MATLAB (R2018B, MathWorks, MA, USA) [3], consisting of cylinders of varying sizes to model regions of tissue/vessels. For each cylinder, PK parameters (K^{trans}, v_e, and v_p) were defined and a contrast agent concentration time course, C_t, was calculated from the Tofts model. A 2-minute scan was simulated using a golden angle stack of stars sampling pattern, which generates images with an arbitrary temporal resolution determined by the rays per phase. Images were reconstructed using compressed sensing [4,5]. Recovered PK values were found from nonlinear least squares fitting of the recovered C_t series [6]. IQM reference was generated from the last 30 seconds of data (when the time course is stable).

Results and Discussion – As more rays per phase are added the aliasing noise level of the recovered C_t decreases at the expense of temporal resolution (Fig. 1). There is a broad range of rays per phase for which the accurate K^{trans} values can be recovered (Fig. 2). Above this range, the K^{trans} is overestimated due to poor temporal sampling and below this range it is underestimated due to poor image quality. We found that the plateau can be located using the SSIM of the reconstructed images relative to the reference by moving down the vertical asymptote at SSIM = 1, by iteratively increasing the temporal resolution (Fig. 3).

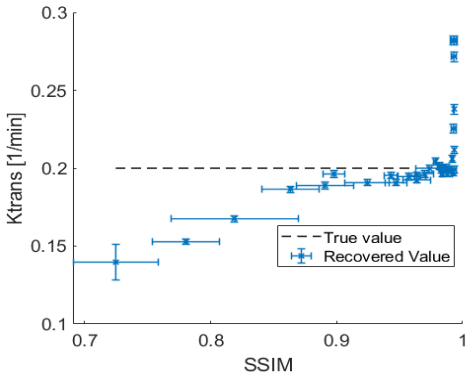

Fig. 3: Value of the recovered Ktrans value for a variety of temporal resolutions versus the SSIM of the recovered image volume.

Conclusions – We demonstrate an IQM based heuristic for accurately calculating PK parameters by determining appropriate temporal resolution in synthetically derived DCE data.

References - [1] Tofts, Mag. Res. Med. (1997). [2] Wang, IEEE Trans. Imag. Proc. (2004). [3] Murtha, Proc. ISMRM. (2017). [4] Uecker Proc. ISMRM (2015). [5] Lustig, Mag. Res. Med. (2007). [6] Barnes, BMC Med. Imag. (2015).

Study on Electrical Properties under Magnetic Resonance with High Field

X. Li[a], S. Zhao[a,b], X.K. Li[a,c], G. Liu[a,c], Z. Yuan[d], J. Qiu[e]

[1]Institute of Electrical Engineering, C. A. S., Beijing, China, [2] Hebei University of Technology, Tianjin, China, [3]University of Chinese Academy of Sciences, Beijing, China, [4]Hubei Cancer Hospital, Wuhan, China, [5]Taishan Medical University, Taian, China

Introduction: Traditional biomedical imaging can have a good imaging effect on the biological tissue structure. But for diseases such as the early stage of cancer, the structure image may not change obviously. Studies on Magnetic Resonance Electrical Properties Tomography (MREPT) have found that the conductivity will change significantly in the early pathological state [1-3]. This paper researched the imaging of Radio Frequency (RF) field and as a result the electrical properties under 3T and 7T MRI.

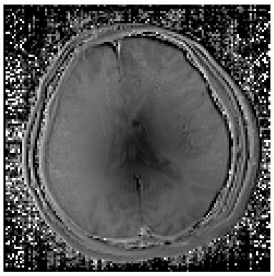

Fig. 1: Brain B_1 phase map of human subject under 3T.

Methods: The conductivity and dielectric constant of tissue can be solved from the magnetic field of RF coil (B_1^+), while the latter can be mapped from the proton density image [4]. Based on the Ampere's and Faraday's laws, the B_1 field and its relationship with tissue properties can be expressed as follows:

$$B_1^+(\mathbf{x}) = \frac{\mu}{2}\left(H_x(\mathbf{x}) + jH_y(\mathbf{x})\right) \quad \text{Eq. 1}$$

$$\varepsilon_r = -\frac{1}{\mu_0\varepsilon_0\omega^2}\mathrm{Re}\left(\frac{\nabla^2 B_1^+}{B_1^+}\right) \quad \text{Eq. 2}$$

$$\sigma = \frac{1}{\mu_0\omega}\mathrm{Im}\left(\frac{\nabla^2 B_1^+}{B_1^+}\right) \quad \text{Eq. 3}$$

where μ is the magnetic permeability, ε_r relative dielectric constant, σ conductivity and ω angular frequency. With formulating the above equations for discrete data, the image on interesting slice can be constructed with aid of adjacent 3 slices. The experiments were based on spin echo sequence and the parameters as, FOV 240×240mm^2, resolution 256×256, 5 slices, thickness 2mm, excitation and refocusing flip angles of 60/120^0 and 120/240^0, respectively.

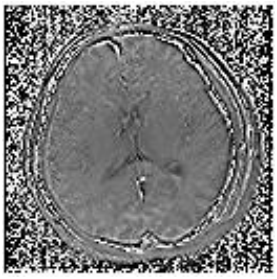

Fig. 2: Dielec. constant map derived from B_1 phases and MRI k space in sequence.

Results and discussion: Two human subjects were studied in accordance with institutional review board guidelines. The magnitude of B_1 was achieved with the double-angle method. And the phase of B_1 was approximated to half of that of MRI. For accurate calculation of B_1 mapping, this condition should be satisfied, TR>>T_1>>TE, where TR repetitive time, T_1 longitudinal relaxation time and TE echo time. The resultant B_1 magnitude map and the derived dielectric constant distribution are shown in Fig. 1 and 2, respectively. Note that for calculating B_1 magnitude, the phase of MRI magnetization should be unwrapped firstly. Currently the principle of double-angle method is simple but the scanning time was quite long. Bloch-Siegert Shift based method for B_1 mapping would be used in further experiments at Bruker 7T [5].

Conclusion: With the MRI experiments at high magnetic fields, the RF magnetic field were mapped and in-vivo tissue electrical properties reconstructed. With the increase of the strength of main magnetic field, the frequency-related dielectric constant was remarkable as shown in the image. MREPT is a good tool for estimating SAR when operating in long-term scanning condition.

References: [1] Balidemaj, IEEE Trans. M. I.(2015). [2] Wang, M. R. M. (2005). [3] He, IEEE Trans.B.E. (2017). [4] Bulumulla, Concept in M.R. (2012). [5] Sacolick, M.R.M. (2010).

Sub-10μm Resolution μMRI Study of Rabbit Cartilage

S. Batool, Y. Xia
Dept of Physics, Oakland University, Rochester, Michigan 48309, USA

Introduction Articular cartilage is a thin layer of load bearing tissue that covers the articulating ends of bone in joints. The gradual degradation of cartilage leads to osteoarthritis (OA), a major musculoskeletal disease that contributes to the number one cause of disability in adults. In recent years, the use of rabbits in OA research has increased due to its closer phylogenetical and genetic resemblance to humans than small rodents. Since the thickness of rabbit cartilage is less than 400μm, high resolution imaging is a must in order to resolve the depth-dependent molecular compositions and structure. This work aims to characterize the molecular and morphological structures in rabbit cartilage, using μMRI quantitatively and at sub-10μm resolution. Polarized light microscopy (PLM) at 1μm resolution is also used for complementary verification.

Methods Five shoulder joints were obtained from 12-14 weeks old healthy rabbits. The intact joints were imaged on a Bruker AVANCE II 300MHz system at 70μm transverse resolution with the MSME (multi-slice multi-echo) sequence. Subsequently, two cartilage-bone plugs (each about 3×1.5×2mm) were obtained from the central part of the joint. Quantitative T2 and T1ρ imaging were carried out with the magnetization-prepared spin-echo sequence at 9.75μm transverse resolution. After μMRI, multiple thin sections were obtained histologically from each cartilage sample, which were imaged under PLM to generate two optical parameter images (angle and retardation).

Results and Discussion Articular cartilage in the low-resolution images (a) are visible. The rectangular shape in (a) marks the region where the tissue blocks were harvested, which were imaged at high resolution (b-c). The magic angle effect is clear in these high-resolution images. The profile comparison between the low- and high-resolution T2 images (d) shows clearly the critical consequence of the resolution deficiency in cartilage imaging – where the two surface zones are averaged together in low resolution images that causes the missing of the most important feature of T2 anisotropy in cartilage. A number of T2 images were also acquired at different orientations (e), which further enables the study of depth-dependent T2 anisotropy. Quantitative T1ρ-weighted images appeared more homogenous and without a clear laminar appearance at any orientation. Quantitative PLM images support the findings in μMRI.

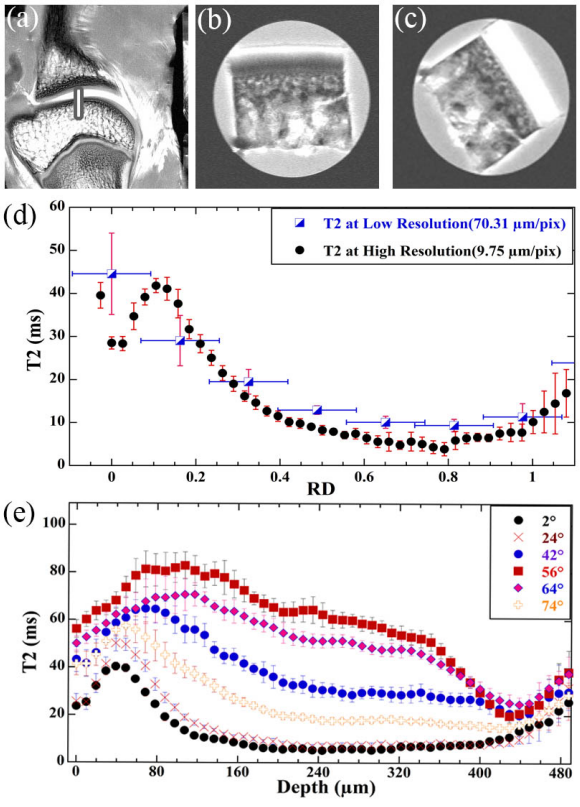

Conclusion Quantitative μMRI combined with quantitative PLM verification of rabbit cartilage can be used to better understand cartilage degradation (1). To the best of our knowledge, our in-plane 9.75 μm/pixel is the highest resolution ever obtained in any quantitative MRI study of cartilage.

References 1. Xia & Momot, Eds., *Biophysics and Biochemistry of Cartilage by NMR and MRI*, the Royal Society of Chemistry, Cambridge, UK (2016).

Acknowledgement Rohit Mahar and Farid Badar for technical help, and NIH R01 grant (AR69047).

Spatially resolved relaxation analysis in bovine and human articular cartilage

A. Creţu, O.V. Petrov, C. Mattea, S. Stapf
Dept. Technical Physics II, TU Ilmenau, Germany

Introduction: Osteoarthritis (OA) as a degenerative disease of articular cartilage is well known to affect a number of parameters accessible by NMR methods, such as relaxation times, diffusion coefficient and its anisotropy, dipolar order and spectral properties. Among these, the rather large variation of relaxation times at low magnetic field strengths hold the best potential for a non-invasive early diagnosis of OA. We have found that T_1 not only varies significantly between the cartilage layers, but is also non-exponential on a microscopic scale due to multicomponent proton pools [1]. Earlier research has addressed the origin of this complex behavior by systematic drying [2] and deuteron replacement [3]. In this study, we extend these approaches towards frequency-dependent relaxation (NMRD) in order to develop models for the molecular reorientation dynamics of water and macromolecules in cartilage.

Methods: Low-field MR experiments employing the NMR-MOUSE with a one-dimensional spatial resolution of 100 µm or better were carried out to benefit from the enhanced contrast in relaxation times towards lower magnetic field strengths. Depth-dependent averaged T_1 and T_2 maps are obtained and are compared to different measures of the relaxation times distribution and their width. These data are complemented by volume-averaged T_1-T_2 correlation maps as well as relaxation times distributions as a function of magnetic field strength (field-cycling relaxometry). A particular focus was put on variation of relaxation properties under drying and rehydration using either H_2O or D_2O brine, comparing T_1 dispersion of residual protons with that of deuterons.

Results and discussion: Following proteoglycan depletion during OA, the water content in cartilage is known to increase locally, leading to longer T_1 of the main component while bound water and the contribution of macromolecules retain their shorter T_1 essentially unaltered, thus generating an increase of the width of the T_1 distribution function. Using spatially resolved averaged values, however, the spread of T_1 across the tissue tends to become smaller. Two-dimensional T_1-T_2 methods have been employed to elucidate this controversial behavior, and we have successfully detected the full range of water environments by combining FID and CPMG signal acquisition. The observed trend upon drying, and the finding that ^{2}H relaxation in cartilage follows a field dependence similar to that of ^{1}H, allows for an improved assignment of the individual relaxation components to different water environments.

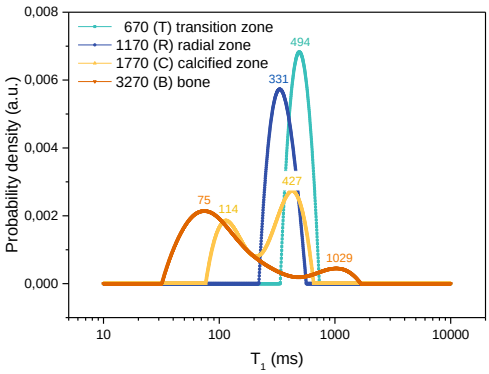

Fig. 1: ^{1}H T_1 distributions within the four principal layers (670 to 3270 µm from the surface) of a healthy bovine articular cartilage sample obtained at 0.27 T.

Conclusions: Determining relaxation distributions at low field and variable field supports the development of models for molecular mobility in cartilage as a simple tissue model without vessels and low cell content. At the same time, methods have been developed to unambiguously quantify relaxation times distribution widths which can be correlated to the disease state in order to assess OA severity in low-field MRI scanners with insufficient spatial resolution.

References: [1] O.V.Petrov, S.Stapf, Magn. Reson Med. **81**, 2158 (2019). [2] R.A.Damion *et al.*, Osteoarthritis Cartilage **20**, 184 (2012). [3] S.Tadimalla, K.I.Momot, PLOS One **9**, e115288 (2014).

MRI characterization of long-term brain damage induced by low dose irradiation at two different exposure ages in the mouse.

L. Mouton[1,2], *O. Etienne*[2], *D.A. Barrière*[1], *E.A. Pérès*[3], *F. Boumezbeur*[1], *F.D. Boussin*[2], *D. Le Bihan*[1]
[1] NeuroSpin, CEA, Gif-sur-Yvette, France, [2] UMR Genetic Stability, CEA, INSERM, Fontenay-aux-roses, France, [3] UMR 6030, GIP CYCERON, Caen, France

Introduction: In mammals, brain development starts *in utero* and extends beyond birth. Therefore post-natal as *in utero* irradiation are likely to impair neurogenesis[1]. While the effects of high doses of radiation on the brain have been studied, the brain's responses to low doses of radiation remain rather obscure. In this context, it is relevant to evaluate the low dose radio-induced effects on the brain at different exposure ages. This study aims at investigating, by anatomical and diffusion MRI, cerebral damage following *in utero* and post-natal low dose irradiation in mice.

Methods: C57Bl/6N gestant mice (and their fetuses) were irradiated on the 14.5th day of gestation or young male mice were irradiated on their postnatal day 10 (PN 10). For both exposure, a low dose of 100mGy for the whole body was delivered from a ^{137}Cs source. At 3 months-old, irradiated ($N_{IRR,PN10}$ = 23, $N_{IRR,E14.5}$ =25) and non-irradiated (N_{Sham} = 21) mice were imaged using an 11.7 T MR scanner. The MRI protocol consisted in the acquisition of: (i) a whole-brain 3D T2*-weighted anatomical images and (ii) a diffusion MRI (20 b-values: 0-3000 s/mm2 along 6 directions). The ROIs-based pipeline analysis was performed on: (i) the anatomical images and (ii) the diffusion parametric maps (ADC, K, FA, S-index [2]) to evaluate respectively volumetric and microstructural changes [3]. Statistical significances between the three groups were assessed using ANOVA and Tukey post-hoc tests.

Results and discussion: No significant volumetric changes were observed whatever stage of brain development during irradiation. However, significant microstructural alterations were detected in mice irradiated at E14.5 in comparison to the Sham and PN10 mice (Fig 1). While paradoxical at first glance, the subtle changes observed in E14.5 mice could reflect compensatory mechanisms leading to cellular proliferation (eventually linked to an upregulated neurogenesis) and an original organization of the brain in absence of atrophy. Moreover, this absence of significant atrophy is not unexpected considering the modest dose of ionizing radiation (100 mGy), especially for PN10 mice [4].

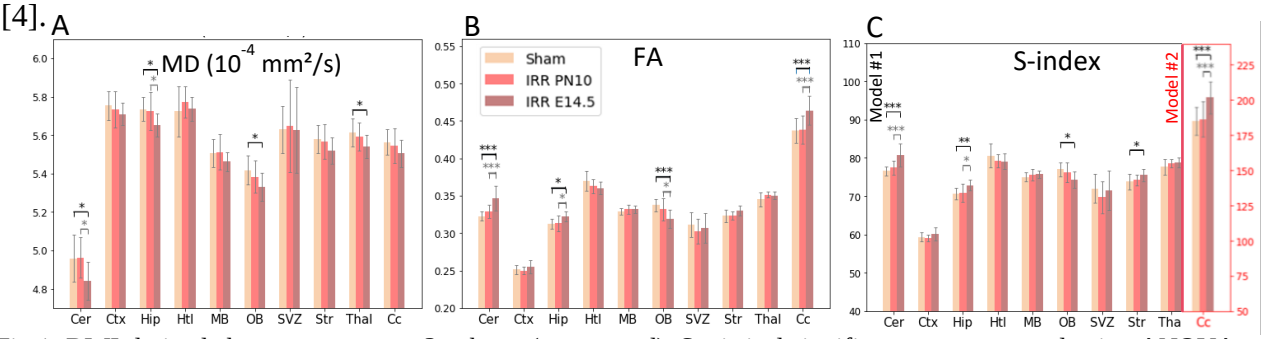

Fig 1: DWI-derived changes across our 3 cohorts (mean ± std). Statistical significance was assessed using ANOVA and Tukey post-hoc tests: *** p<0.005; ** p<0.01; * p<0.05. A. Mean Diffusivity; B. Fractional Anisotropy;
C. S-index in GM (model #1) and WM (model #2) ROIs. Cer: Cerebellum; Ctx: cortex; Hip: Hippocampus; Htl: Hypothalamus; MB: MidBrain; OB: Olfactory Bulb; SVZ: Subventricular zone; Str: Striatum; Thal: Thalamus; Cc: Corpus callosum

Conclusion: *In utero* irradiation manifests in subtle ways through microstructural variations mainly in the Cc, the Cer and in neurogenic areas like the Hip and the OB. As shown previously [3], S-index is the most sensitive diffusion metric to detect radiation-induced brain damage. In the future, diffusion MRI could be used to explore radio-sensitivity across exposed human populations.

References: [1] Nieman, Int J Radiat Oncol Biol Phys (2015). [2] Iima M, Radiology (2016). [3] Pérès, Int J Radiat Oncol Biol Phys (2018); [4] Verreet, Front Behav Neurosci (2016).

Estimates of Blood Plasma Water Content Using Portable NMR Relaxometry

S. N. Fricke, J. Pourtabib, J. Madsen, S. Chizari, J. Phan, N. K. Tran, M. P. Augustine
University of California, Davis, CA 95616, USA

Introduction: Although blood plasma water content (PWC) is a relevant metric for many medical diagnostic procedures, the routine clinical measurement of PWC has remained elusive. Portable nuclear magnetic resonance (NMR) offers one way to nondestructively and quickly measure PWC in clinical settings.[1] The societal impact of this seemingly obvious work is quite significant. A large percentage of medical decisions are based on laboratory tests, many of which are blood chemistry assays. However, the accuracy of blood tests can depend on blood water content, which is not typically measured in clinical laboratories. This is because the current gold standard method for measuring PWC is lyophilization, which is a time-intensive process that requires about 24 hours. The delays from this procedure are prohibitive in a clinical laboratory that must process thousands of samples daily, and are unacceptable in situations that require urgent treatment decisions. Consequently, blood test results are based on an assumption of a standard value of 93% PWC.[2] However, variance in PWC between patients can influence many test results, with blood electrolyte and metabolite measurements being perhaps the most notable.[3] Thus, the development of a rapid test to measure PWC will provide clinicians with a means to improve the accuracy of blood chemistry assays and diagnostic tests, which will improve patient care and reduce waste.[4]

Methods: Contrived pseudoplasma samples that mimic blood while also allowing rigorous control over water content are used to demonstrate the role of NMR in this work. Calibration curves relating measured NMR relaxation time constants (T_2 and T_1) to gravimetric PWC values for a set of human lyophilized plasma samples are used to predict the PWC in porcine and model human blood from respective NMR T_2 and T_1 values.

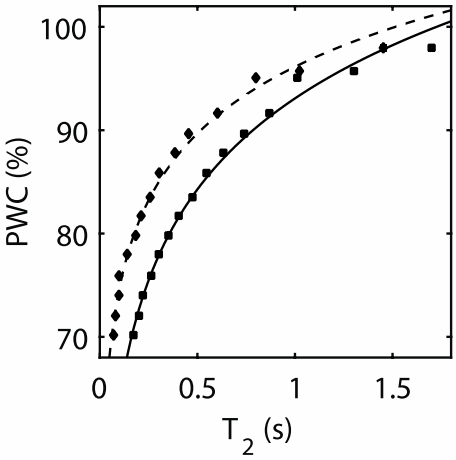

Fig. 1: Correlation of gravimetric PWC with NMR-determined T_2 value for pseudoplasma and human lyophilized plasma sample sets as solid squares and diamonds respectively. The solid and dashed lines for the respective pseudoplasma and human lyophilized plasma samples were calculated by fitting the data to a shifted log function. The error bars largely obscured by the data markers indicate 95% confidence.

Results and Discussion: It is shown that the T_2 and T_1 decay constants measured with low field NMR relaxometry correlate with the PWC values for pseudoplasma and human lyophilized plasma samples. Statistical testing of the NMR-PWC correlation model demonstrated prediction accuracy exceeding 98%. The PWC obtained in this way was used to correct sodium cation concentrations reported from direct ion-selective electrode tests.

Conclusion: The accuracy of PWC determination with NMR is comparable to that of the gravimetric method that requires sample lyophilization. The rapid turnaround time, non-destructive nature, and portable footprint of the NMR-PWC measurement makes rapid, point-of-care clinical electrolyte estimates possible.

References: [1] Cistola, D. P., Robinson, M. D., *Trends Analyt. Chem., 83*, 53–64. (2016). [2] Fogh-Andersen, N., D'Orazio, P., *Clin. Chem., 44(3)*, 655. (1998). [3] Nguyen, M. K., Ornekian, V., Butch, A. W., Kurtz, I., *AJP: Renal Physiology.* (2007). [4] Zhi, M., Ding, E. L., Theisen-Toupal, J., Whelan, J., Arnaout, R., *PLOS ONE, 8(11)*, e78962. (2013).

PVA Phantom for MRI Study of Myocardial Viability

V.V. Rodin[1], *T. Anderson*[3], *M.A. Jansen*[2,3], *G.A. Gray*[3], *W.M. Holmes*[1]

[1]Glasgow Experimental MRI Centre, Institute of Neuroscience and Psychology, College of Medicine, Veterinary and Life Sciences, University of Glasgow, Glasgow, UK, [2]Edinburgh Preclinical Imaging, University of Edinburgh, Edinburgh, UK, [3]Centre for Cardiovascular Science, University of Edinburgh, Edinburgh, UK

Introduction: The wide spread use of rodent models in diseases studies stimulates the development of pre-clinical imaging techniques. The present work describes the construction and testing of a novel type of pre-clinical MRI cardiac phantom fabricated from poly vinyl alcohol (PVA) [1]. The use of this PVA cardiac phantom allows new cardiac MRI methods to be developed [2,3], thus reducing the number of live animals used. This is in accordance with the UK's policy of reduction, refinement and replacement [1]

Fig.1. *MRI cardiac phantom*: the actuator coil with the attached motion sense coil and linkage to the syringe. The syringe and tubing provide a means to fill the chamber with water/lubricant prior to scanning.

Materials and Methods: Aqueous solutions of 10 or 15 wt% PVA (PVA powder with molecular weight of 85,000-124,000, 99+% hydrolized) were used to prepare flexible solid polymer "cardiac chambers" (the tube diameter was comparable with the size of a rat heart, ~10 mm) by 2-3 repeated cycles of 12-20 hr freezing at -20ºC and 16-24 hr of 3 steps thawing (0ºC, +7ºC and +22ºC). The phantom applies the coil actuation technique and avoids the need for remote pumps and the problems with long pipes typically found in previous cardiac phantoms [1, 2]. ^{1}H MRI scans (7T) were acquired of the "cardiac chamber" at different pulsation rates (1-6 Hz). T_1-(FAIR_EPI) and T_2-(MSME) mapping resulted in T_1=3.02 s, T_2=586 ms (water) and T_1=1.82 s, T_2=125 ms (polymer wall). MSME, RARE, FLASH cine sequences have been tested with different triggering conditions and pulsation rates on "PVA-chamber" filled by water / FOMBLIN lubricant (Fig.2) (to remove water motion artefacts and image distortions).

Results and discussion The cardiac phantom was used to test and optimize a number of cardiac MRI sequences, including an MSME scan (10 echoes, triggering at 80 ms delay), which gave images without motion artefacts at a 6-Hz frequency, which is comparable to rat heart pulsation rates (Fig.3).

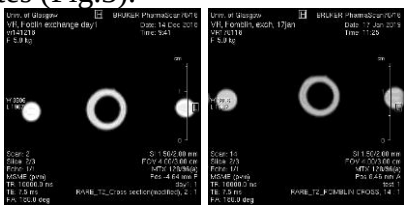

Fig.2: Image of PVA-chamber in Fomblin: original (left), after 2 weeks (right) storage

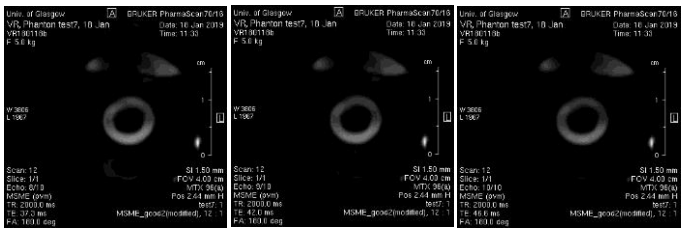

Fig.3: PVA-chamber in Fomblin: TE=37; 42 and 47 ms in MSME

Conclusion: The compact design of the phantom with PVA "cardiac chambers" allows fast setup and is suitable for MRI studies. Changes in the PVA structure and in cross-linking process result in flexible solids with different permeability and deformation properties as reliable alternatives to animal subjects to develop and test new cardiac MRI pulse sequences.

References: [1] Fortune S, Jansen MA, Anderson T, Gray GA et al. *Magn Reson Imaging* (2012) 30(8),1186-1191. [2] Holmes WM et al. NMR in Biomedicine. (2011), 25, 295-304.
[3] Holmes WM, McCabe C, Mullin JM et al. NMR in Biomedicine (2009), 22, 745-752.

Toward in vivo pH Sensing using Hyperpolarized ^{129}Xe MRI

P. Berthault[a], *E. Léonce*[a], *J.-P.Dognon*[a], *D. Pitrat*[b], *J.-C. Mulatier*[b], *T. Brotin*[b]

[a] NIMBE, CEA, CNRS, Université Paris Saclay, CEA Saclay, 91191 Gif-sur-Yvette, France

[b] Laboratoire de Chimie de l'Ecole Normale Supérieure de Lyon, 46, Allée d'Italie, 69364 Lyon Cedex 07, France

Introduction: Monitoring of extracellular pH in living organisms is pivotal as it affects many important biological processes. Because fluorescence spectroscopy suffers from low penetration depth (few mm), MRI can be a powerful tool provided that its intrinsic lack of sensitivity is avoided. Here as a proof-of-concept we show that hyperpolarized xenon encapsulated in dedicated cage-molecules can be used in this purpose.

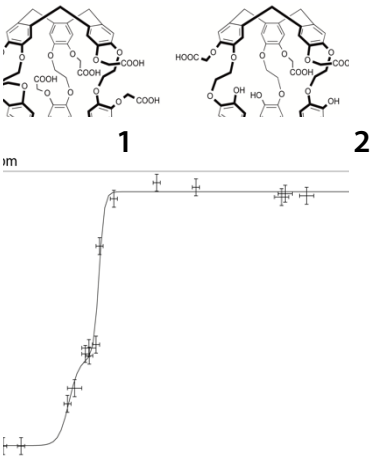

Fig. 1: Two cage-molecules used in this study, and plot of the xenon chemical shift difference $\Delta\delta_{12} = \delta_{(Xe@2)} - \delta_{(Xe@1)}$.

Methods: The in-out exchange dynamics of xenon for cryptophane cages is fast; moreover, xenon inside theses hosts experiences a strong upfield shift (from ca. 200 ppm to 60 ppm). The idea is to perform a differential measurement by using a pair of pH-sensitive ^{129}Xe NMR-based sensors, instead of only one as in ref. [1]. The difference between the chemical shifts of xenon encapsulated in both molecular sensors (Fig. 1) gives access to pH.[2] The method is rendered very sensitive to pH *via* the choice of two xenon host molecules in which the frequencies of the noble gas signals vary in opposite manner with the H^+ concentration.

Results and discussion: The method can be used *in vivo*. It is simple, robust against temperature, ionic strength and solvent effects. As an example, $\Delta\delta_{12}$ decreases by only 0.01 ppm for a temperature change of 10°. As the introduction of xenon is fully decorrelated from that of the cryptophane mixture, it means that i) the quantity of xenon host introduced can be very low, reducing the risks of toxicity, ii) the xenon relaxation time is not as crucial as for other hyperpolarized species; there is no limitation to one-shot experiments: the cryptophane mixture can be delivered once, then many NMR experiments can be performed with different xenon batches.

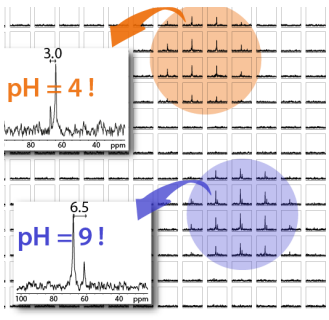

Fig. 2: ^{129}Xe chemical shift imaging for pH sensing. Two tubes of inner diameter 2.3 mm contain a mixture of cryptophanes **1** and **2** at pH 4 (orange) and pH 9 (purple). The concentrations range between 150 and 250 µM.

Conclusion: Obviously, the pH range that can be probed with the current cryptophane pair cannot be used for biomedical applications. But this concept can be extended to other cryptophane pairs. For instance, cage-molecules decorated with citric acid or diethylmalonic acid functions of pk_a values close to the physiological pH are promising. This work is underway in our laboratories. It is noteworthy that these cryptophanes may present different solubilities in tissues or different bio-distribution in tissues thus impeding the simultaneous detection of two caged xenon signals at the same location. This problem could be overcome by linking cryptophanes to each other. Bis-cryptophanes, whose synthesis is already mastered by us could be a solution to have in one molecule the expected differential pH probe.

References: [1] P. Berthault *et al.* Chem. Eur. J. (2010) 16, 12941.
[2] E. Léonce *et al.* Chem. Eur. J. (2018) 24, 6534.

Dual Modality Imaging of Powdered Diamond: Optics and Room Temperature Hyperpolarized MRI

Xudong Lv[1]; Fei Wang[1]; Danila Barskiy[1]; Emanuel Druga[1]; Alessandra Aguilar[1]; Benjamin Safvati[1]; Priyanka Raghavan[1]; Tommy Mcknelly[1]; Raffi Nazaryan[1]; Ben Han[1]; Carlos A. Meriles[2]; Jeffrey A. Reimer[1]; Dieter Suter[3]; Jeffrey H. Walton[4]; Ashok Ajoy[1]; Alexander Pines[1]

[1]UC Berkeley, Berkeley, CA, USA, [2]The City College of New York, New York City, NY, USA, [3]Technische Universit at Dortmund, Dortmund, Germany, [4]UC Davis, Davis, CA, USA

Introduction: Functionalized diamond nanoparticles hold immense promise for biomedical applications such as targeting, sub-cellular tracking, and non-toxic therapy. Diamond hosts a variety of remarkable properties that make it suitable as nontoxic substrates for targeted drug delivery and as highly biocompatible fluorescent markers for cellular tracking. Fluorescence from defects in diamond affords optical detection and this modality is widely used in sensing and imaging. A non-invasive methodology for diamond particle tracking in deep tissue has yet to emerge with diamond, hence considerable efforts are aimed at developed Magnetic Resonance Imaging (MRI) methods for doing so. The long spin-lattice relaxation time of diamond and enhanced signal will allow diamond to be well distinguished and traced with MRI, and will open up possibilities in using diamond as a targeting and tracking agent.

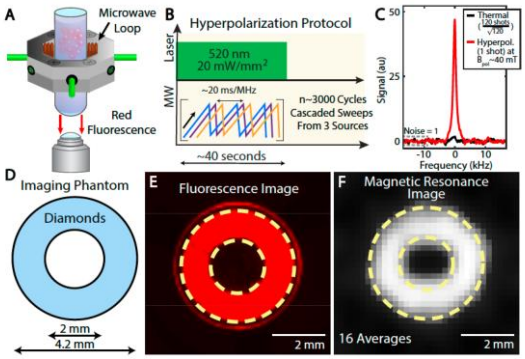

Figure 1. Images of same phantom with two modalities.

Methods: The laser beams guided by optical fibers coming from 4 different directions excite the sample, and the red fluorescence is collected by a CMOS detector (Figure 1A). ^{13}C in diamond is polarized by laser excitation and microwave irradiation at low field (Figure 1B). Subsequently the sample is shuttled to high field to perform NMR spectroscopy or MR imaging. A FLASH imaging sequence (TR/TE=500/0.6ms, NEX = 16, pixel = 0.16 mm^2) was used to reduce the echo time in order to overcome the short T_2 of ^{13}C nuclei in diamonds. The fluorescence image was captured by a CMOS camera with 532nm laser excitation.

Results and discussion: The hyperpolarized ^{13}C signal (Figure 1C) has an enhancement of 277 compared with thermal signal at 9.4 T, which corresponds to 5 orders of magnitude of measurement time gain. A 'ring' shaped phantom is filled with 40 mg of diamond particles and used in both optical imaging (Figure 1E) and magnetic resonance imaging (Figure 1F). The ^{13}C MRI was performed in a 9.4 T magnet at room temperature. Figure 2A demonstrates the sign of the polarization is determined by the direction of the microwave sweep. The magnetic field dependent energy levels of NV center make it possible to modulate optical image of diamonds (B). The photo luminescence reduced by about 7% at 400 G vs. 0 field. Positive and negative images of diamond particles are in Figure 2 C and D. Figure 2 E and F show brighter and darker image of the phantom with diamond particles. Brighter image was taken without additional magnetic field and darker image was with ~400 G magnetic field.

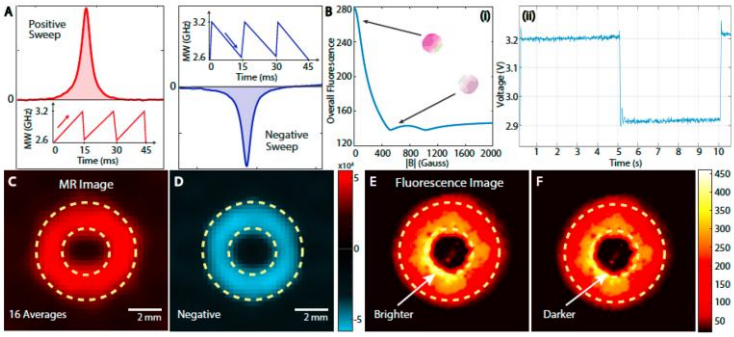

Figure 2. Image modulation

Conclusion:
Hyperpolarized nano-diamonds show promise as dual modality imaging agents.

A new method to correct the effect of saturated hydrocarbon to nuclear magnetic resonance (NMR) T2 distribution in tight porous media

Liang Xiao[a], *Wei Zhang*[b], *Xiuhong Xie*[a]
[a]China University of Geosciences, Beijing, China, [b]COSL, Sanhe, China

Nuclear magnetic resonance (NMR) data is considered to be the most valuable in characterizing rock pore size and distribution at present. However, theory and field applications in China illustrate that the NMR data is not always usable in hydrocarbon-bearing formations, because the shapes of the NMR distributions are heavily affected by the bulk relaxation of hydrocarbon. In this study, to understand the effect of hydrocarbon to NMR T2 spectrum, the kerosene and transformer oil are used to simulate formation crude oils with different viscosity. 20 core samples, which were drilled from three different types of formations, are saturated with four conditions (irreducible water saturation, fully saturated with brine, hydrocarbon bearing condition and residual oil saturated) to apply for lab NMR measurements. Meanwhile, the bulk relaxations of brine, kerosene and transformer oil were measured. The residual oil saturated condition is used to simulate field NMR logging due to the shallow investigation depth. Comparisons of the NMR spectra under 4 saturated conditions and the bulk relaxation T2 distribution of experimental used oil illustrate that hydrocarbon has little effect to the NMR T2 spectra in conventional and tight sands. However, in medium to low permeability sands, the shapes of T2 distributions are heavily affected. In this condition, the NMR T2 spectra need to be first corrected to remove the effect of hydrocarbon before they are used for pore structure characterization. Based on the lab NMR measurements of fully brine saturation and residual oil condition for 9 core samples drilled from medium to low permeability sands, a new method, which is used to correct the effect of hydrocarbon to NMR T2 spectrum, is proposed. This method is proposed based on the pore components percentage compositions, which is extracted from NMR T2 distribution saturated with residual oil. The reliability of this method is verified by the comparing the corrected results and the lab NMR measurements. This method is well applied in field application in the Cretaceous of Shinan area of Junggar Basin, northwest China, fully water saturated T2 distributions are acquired from field NMR logging, and they are well used for formation pore structure evaluation.

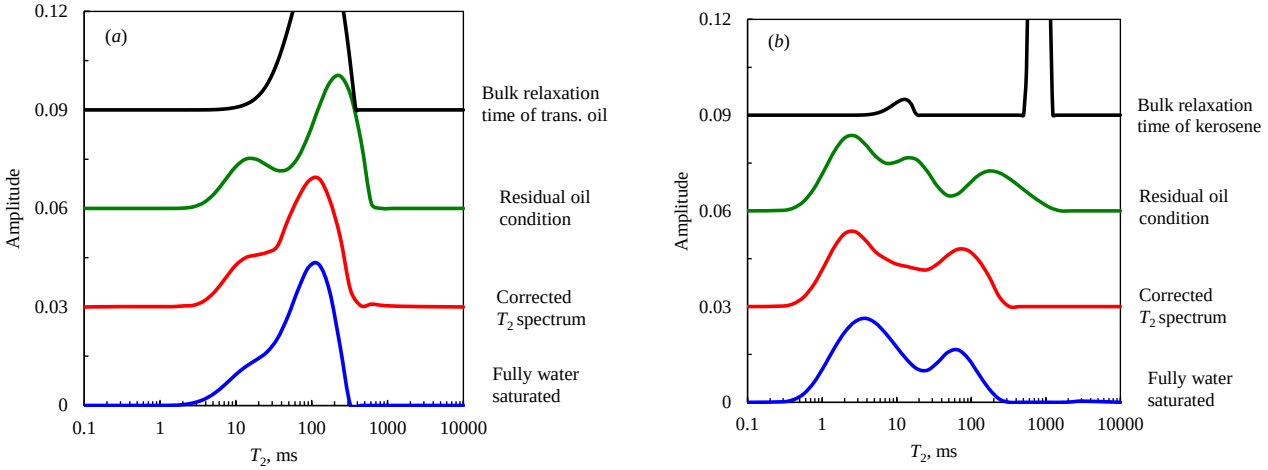

Fig. 1 Comparisons of corrected NMR T2 distributions with lab measured results under fully brine saturation verify the reliability of our proposed model.

References: [1] Xiao, L., Journal of Petroleum Science and Engineering (2016). [2] Mao, Z.Q., the 47th SPWLA Annual Logging Symposium (2007).

Analysis of 3-site T_2- T_2 exchange NMR

Y. Gao [a,b], B. Blümich [b]
[a] College of Science, China University of Petroleum, Beijing, China 102249
[b] Institute of Technical and Macromolecular Chemistry, RWTH Aachen University, Aachen, Germany, 52056

2D T_2-T_2 exchange NMR: T_2-T_2 exchange NMR is a unique method to investigate the pore space and fluid dynamics in porous media. The pulse sequence of the T_2-T_2 exchange NMR experiment is described in Fig. 1. During the detection period at time $t_2+t_m+t_1$ the transverse magnetization is $\boldsymbol{M}(t_2+t_m+t_1)=\exp[-(\mathbf{R}^{(2)}+\mathbf{K})t_2]\{\exp[-(\mathbf{R}^{(1)}+\mathbf{K})t_m][\exp[-(\mathbf{R}^{(2)}+\mathbf{K})t_1]\boldsymbol{M}^{\mathrm{eq}}-\boldsymbol{M}^{\mathrm{eq}}]+\boldsymbol{M}^{\mathrm{eq}}\}$, where $t_1=n_1t_{\mathrm{E1}}$ and $t_2=n_2t_{\mathrm{E2}}$. The measured signal obtained from the sum of the magnetization components with phase cycling is $\bar{s}(t_1,t_2)=(1,1,1)\exp[-(\mathbf{R}^{(2)}+\mathbf{K})t_2]\exp[-(\mathbf{R}^{(1)}+\mathbf{K})t_m]\exp[-(\mathbf{R}^{(2)}+\mathbf{K})t_1]\boldsymbol{M}^{\mathrm{eq}}$. Upon further evaluation, $\bar{s}(t_1,t_2)=\boldsymbol{\alpha}(t_2)\mathbf{P}\boldsymbol{\alpha}(t_1)^{\mathrm{T}}$ where $\boldsymbol{\alpha}(t)=\left(e^{-\lambda_1 t}\quad e^{-\lambda_2 t}\quad e^{-\lambda_3 t}\right)$ with the T_2-T_2 exchange map $\mathbf{P}=(P_{ij})$ and $P_{ij}=(1,1,1)\,\boldsymbol{q}_j\boldsymbol{w}_j^{\mathrm{T}}\exp[-(\mathbf{R}^{(1)}+\mathbf{K})t_m]\boldsymbol{q}_i\boldsymbol{w}_i^{\mathrm{T}}\boldsymbol{M}(t_0)$ being the amplitude of $e^{-\lambda_i t_1}e^{-\lambda_j t_2}$.

Asymmetric exchange maps: The map is symmetric if and only if $k_{ij}\,M_j = k_{ji}\,M_i$, for i, j = 1,2,3. It means that the number of molecules that travel from site i to site j is equal to the number of molecules that travel from site j to site i for all sites i and j. The net exchanged magnetization is zero for each site. For an asymmetric map, the net exchanged magnetization is not zero. So the asymmetric map reports cyclic flow in the sample.

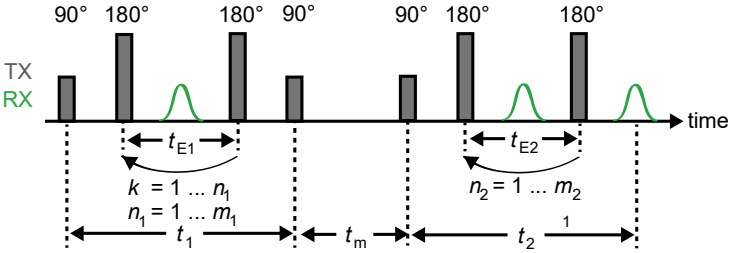

Fig. 1: Pulse sequence of 2D T_2-T_2 exchange NMR.

Table 1. Asymmetric map

	$T_{2,1}^*$=0.2438	$T_{2,2}^*$=1.0819	$T_{2,3}^*$=3.3969
$T_{2,1}^*$	10.5014	1.3352	3.4811
$T_{2,2}^*$	2.7117	43.7640	4.0478
$T_{2,3}^*$	1.7598	7.5079	92.5360

Complex eigenvalues: The eigenvalues of $\mathbf{R}^{(1)}+\mathbf{K}$ and $\mathbf{R}^{(2)}+\mathbf{K}$ could contain complex values. This means the apparent relaxation times could be complex. However, the signal is real. If the apparent T_2 is complex, the three-site exchange map coalesces to a two-site exchange map with oscillations in the time domain. In many cases, there are peak shifts in a 2D two-site T_2-T_2 exchange map. There is another reason for the shifts when the shorter T_2^* is less than expected: the map derives from three-site exchange with two complex conjugate T_2^* and a real T_2^* which coalesces to an apparent two-site exchange map.

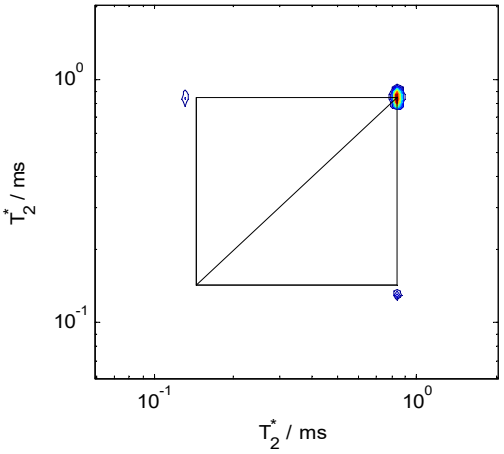

Fig.2: Inverted map with complex eigenvalues. The left vertical line is T_2^* =1/a and the right one is T_2^* =1/ λ_3.

Negative peaks: There exists a symmetric map with negative peaks. A negative peak amplitude means that more molecules move from one site to the other in the evolution period or detection period than in the mixing period.

Table 2. Negative peaks

	$T_{2,1}^*$=0.7542	$T_{2,2}^*$=1. 0515	$T_{2,3}^*$=4.7943
$T_{2,1}^*$	11.8939	-1.1588	16.5986
$T_{2,2}^*$	-1.1588	11.5957	5.4740
$T_{2,3}^*$	16.5986	5.4740	143.8918

References:

[1] Landeghem, Concepts Magn. Reson. A (2010).
[2] Song, J. Magn. Reson. (2016).
[3] Monteilhet, Phys. Rev. E (2006).
[4] Venkataramanan, IEEE Trans. Signal Process. (2002)

In-situ CH_4-CO_2 Dispersion Measurements in Rock Cores

Ming Li, Sarah J. Vogt, Eric F. May and Michael L. Johns
Department of Chemical Engineering, University of Western Australia, Crawley, Western Australia, Australia

Injection of carbon dioxide (CO_2) into a natural gas reservoir is an emerging technology for enhanced natural gas recovery (EGR) realizing increased natural gas production whilst sequestering the injected CO_2. However given that CO_2 and natural gas are completely miscible, simulation of potential EGR scenarios is required to determine when breakthrough of CO_2 will occur at the natural gas production wells. For such reservoir simulations to be reliable, accurate dispersion data between CO_2 and natural gas at relevant reservoir conditions are required. To this end we apply one dimensional (1D) magnetic resonance imaging (MRI) to quantify this dispersion process *in-situ* in both sandstone and carbonate rock cores. Specifically we apply the SPRITE MRI sequence [1] to facilitate quantitative axial profiles of methane (CH_4) content during core flooding processes between CO_2 and CH_4. Simultaneously we measure, using infrared (IR), the effluent CO_2 and CH_4 concentrations enabling *ex-situ* dispersion measurements. Via comparison with the corresponding MRI data, the erroneous contributions to dispersion from entry/exit effects and mixing in piping to and from the rock core holder are quantified. Furthermore, we demonstrate how nuclear magnetic resonance (NMR) T_2 measurements can be uniquely used to probe the pore size occupancy of the CH_4 during the core flooding process.

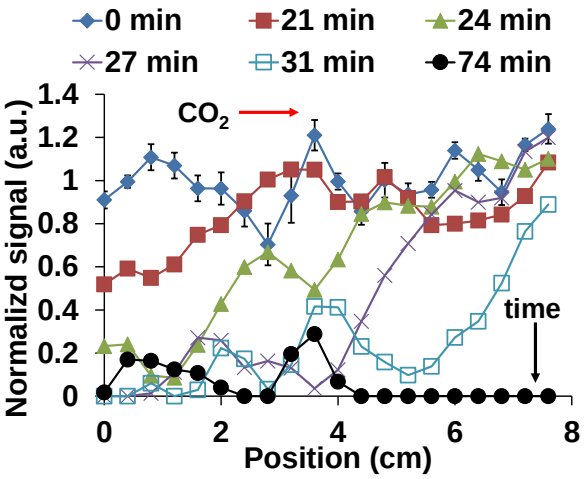

Fig. 1: SPRITE MRI determined CH_4 profiles along a Berea rock core plug during CO_2 flooding to displace CH_4 at a flooding rate of 0.5 ml/min.

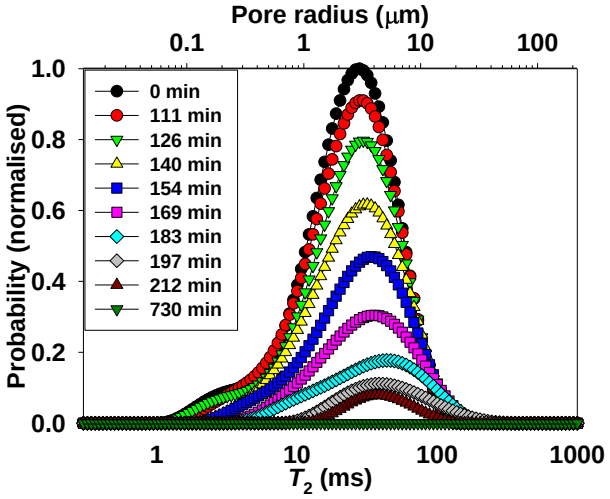

Fig. 2: CPMG determined T_2 distribution of CH_4 in a Berea rock core plug during CO_2 flooding to displace CH_4 at a flooding rate of 0.1 ml/min.

References: [1] Balcom et al., J. Magn. Reson., Ser. A 123(1), 131-134 (1996).

Using NMR to determine gas storage in shale formation

Boqin Sun

Chevron Energy Technology Company, Houston, Texas

Gas in shale reservoirs have become high value hydrocarbon resources recently due to technology breakthrough in hydraulic fracturing. Evaluation of gas storage in shale remains a challenge. Adsorption is one of the main storage mechanisms that could account for up to 20% of total gas reserves in shale. The adsorption capacity of shale formation is normally characterized by adsorption isotherms, which measure the amount of adsorbate on the adsorbent as a function of externally applied gas pressure at constant temperature. The experimentally-measured relationship between adsorbate (V_i) and gas pressure (P_i) is normally characterized by the linear Langmuir pressure (P_L) and volume (V_L) relation:

$$\frac{P_i}{V_i} = \frac{P_i}{V_L} + \frac{P_L}{V_L}. \qquad \text{(Eq 1)}$$

Based on the assumptions used in the Langmuir equation, such characterization only describes physical and monolayer gas adsorption behavior on uniform surfaces of adsorbent. Gas storage characterized by this linear equation is normally shown large uncertainty because the high degree of heterogeneity in shale formation. By generalizing the Langmuir adsorption for inhomogeneous samples, we introduced an isotherm Langmuir adsorption distribution (ILAPD) and then applied a Laplace inversion algorithm on isotherm data to obtain ILAPD (see, reference 1):

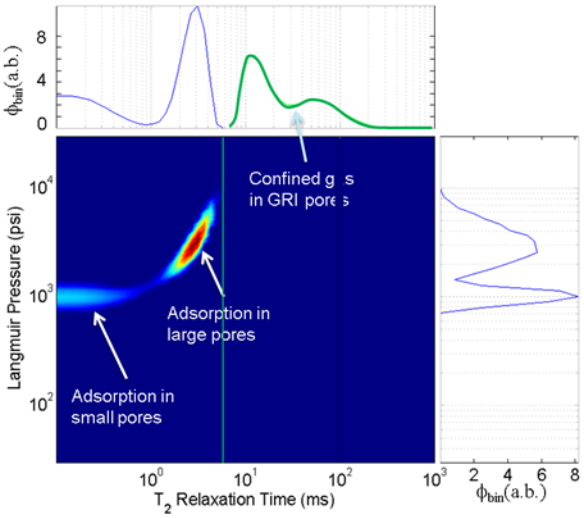

$$V_i = V_c P_i + \sum_{j=1}^{N_P} V_{L,j} \frac{P_i / P_{L,j}}{1 + P_i / P_{L,j}}, \qquad \text{(Eq. 2)}$$

where $V_{L,j}$ and $P_{L,j}$ are Langmuir volume and pressure of the jth component, and N_P is the number of Langmuir pressure components in the ILAPD distribution.

To further enhance the ability to distinguish adsorption from different sites and types, we combined the Langmuir adsorption with NMR T_2 measurement using CPMG echo train sequence to obtain a 2D ILAP-T_2 distribution represented by

$$V_i(nT_E) = V_c P_i + \sum_{j=1}^{N_P} \sum_{k=1}^{N_R} V_{L,jk}(P_{L,j}, T_{2,k}) \frac{P_i/P_{L,j}}{1+P_i/P_{L,j}} e^{-nT_E/T_{2,k}}, \qquad \text{(Eq 3)}$$

where T_E is the echo spacing, N_R is the number of T_2 relaxation time components. Figure 1 shows an example of 2D ILAP-T_2 distribution of a shale sample from which different types of gas stored in different types of pores are separated and their Langmuir pressures can be clearly identified. With this new ILAPD and ILAP-T_2 2D distribution, gas storage mechanism and capacity can be accurately quantified.

Reference

1. B.Q. Sun, H. Wang, S. Gidcumb, Y. Wu, *SPWLA 57th Annual Logging Symposium*, paper DD, Reykjavik, Iceland, June 25-29, 2016.

Characterization of fluid flow through wormholes created by acidification of carbonate rocks: a phase contrast imaging study

B.U. Foerster[a], M.B. Andreeta[a], E.T. Montrazi[a], C. Speglich[b], T.J. Bonagamba[a], F.F. Paiva[a]

[a]São Carlos Institute of Physics, University of São Paulo, CP 369, 13566-590, São Carlos, SP, Brazil; [b]Centro de Pesquisas Leopoldo Américo Miguez de Mello, Av. Horácio Macedo, 950, 21941-915, Rio de Janeiro, Rio de Janeiro, Brazil

Introduction: Acidification is a commonly applied procedure to prepare exploration of new oil wells to potentially improve production rates and/or to recover preexisting wells to better explore the remaining reservoir. As a possible result of the acidification process, preferential flow pathways can be created which are commonly denominated "wormholes". Systematical investigations of the acidification results require reproducible and robust techniques to evaluate and quantify its efficacy. The well-known MR technique of Phase Contrast (PC) Imaging [1] can contribute significantly to this question. In this work, we present the first results of volumetric images characterizing flow patterns through wormholes created by acidification of Indiana limestone core plugs.

Methods: The acidification process was performed at the Petrobras research facility CENPES (Rio de Janeiro, Brazil) using 1.5% hydrochloric acid with a flow rate of 1 ml/min. For MR Imaging, the samples were enclosed in a fluorinated ethylene propylene (FEP) heat-shrink tube and saturated with deionized water by first submitting them to a low vacuum (~60 Torr) and then abruptly breaking the vacuum with inflowing water. During the PC acquisition, a constant flow rate of 50 ml/min was applied. To increase sensibility over a large dynamic range of velocities we applied a multiple velocity encoding (venc) approach [2] with *vencs* of 90, 60, 40, 25, 15, 10 and 6 cm/s. Other acquisition parameters: TE/TR=5.5/14 ms, flip angle 8°, an isotropic spatial resolution of 300 μm^3, a field of view of 38.4x115.2x38.4 mm^3, bandwidth 20 kHz, time per acquisition 1h:30m, total acquisition time of all 7 velocity encodings 10h:30m. Images were acquired on a Bruker Biospin Avance III spectrometer at 2 Tesla.

Results and discussion: This multi-venc PC methodology results in high resolution three-dimensional volumetric maps of the velocity vector field which can be visualized using the open-source software "ParaView". In figure 1a, we show a rendering of streamlines that depict the flow 3D directionality as lines and the flow velocity in color coding ranging from dark blue (0 cm/s) to red (70 cm/s). Integration of measured velocity values perpendicular to the main flow direction yields an average flow rate of 48 ml/min. For comparison, figure 1b shows a velocity map obtained by finite element simulation of the Stokes equation executed with the commercial software "PerGeos" (ThermoFischer Scientific).

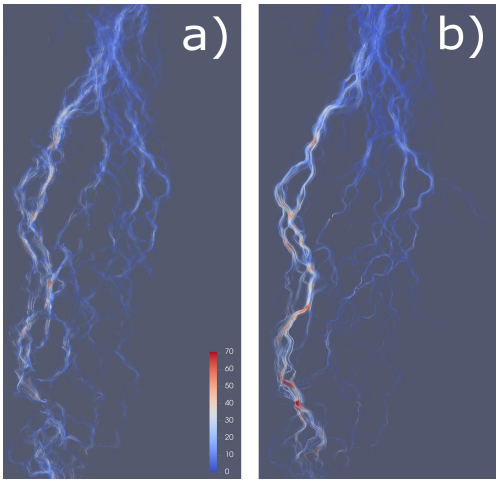

Fig. 1: Representative flow streamlines a) of our multi-venc PC acquisition, compared to b) finite element simulations; colors represent velocity magnitude ranging from 0 (dark blue) to 70cm/s (red).

Conclusions: Estimation of the flow rate from MR measured velocity data (48 ml/min) is in excellent agreement with the physically applied flow rate (50 ml/min). Flow characteristics in velocity maps of MR measured and numerically simulated data show consistent flow pathways. Thus, our results suggest that PC Imaging can be a useful tool for characterizing flow patterns through wormholes.

References: [1] Dumoulin, J Magn Reson Imaging. 1:4 (1991) 399-404. [2] Ha, Magn Reson Med. 75:5 (2016) 1909-1919

Studying molecular diffusion in heterogeneous catalysts on different length scales simultaneously

E. Thompson [1], *N. Nestle* [1], *M. Kellermeier* [1], *K. Graf* [1], *M. Pokrandt* [1] *and H. Schreyer* [2]

[1] BASF SE Materials Physics and Analytics, Ludwigshafen, Germany, [2] BASF SE Zeolite Catalysts, Ludwigshafen, Germany.

Introduction: Molecular diffusion in catalytic systems is important when developing new catalytic processes and can be studied using various different methods.[1] Two such methods are inverse gas chromatography (iGC) and diffusion NMR. iGC is a chromatographic method, similar to the zero length column technique (ZLC), where a known gaseous mobile phase is used to investigate an unknown solid stationary phase. [2] Diffusion NMR and iGC methods look at diffusion processes on different length scales and under different conditions. While NMR focuses on diffusion on the microscale under equilibrium conditions [1], iGC looks at transport resistivities on the mesoscale under non-equilibrium conditions.[2] Additionally, iGC provides many other insights into porous systems, such as adsorption energies.[2] By directly coupling these two methods (Figure 1), a catalytic system can be studied on different length scales, under variable conditions; simultaneously.

Methods and Results: Coupling these two techniques provided many challenges. For example, the information available from iGC depends on the gas reaching the detector only being affected by the catalyst of interest. This is normally achieved by using short steel transfer lines inside a isothermal oven to minimize extraneous interactions. When coupling this technique to NMR, this is not possible due to the static magnetic field. Thorough testing showed that, by carefully selecting the materials used in the setup, it is possible to build an NMR compatible iGC cell and use long transfer lines avoiding the issues with the magnetic field. Furthermore, a major challenge in performing diffusion NMR studies of catalytic systems is controlling the catalyst loading. Using the iGC set up a constant partial pressure of probe molecule can be supplied. This can provide highly controlled loading conditions. The catalyst loading may also be varied allowing the diffusion of alkanes at different loadings to be studied in catalytic systems.

Conclusion: Combining these two techniques enables diffusion of probe molecules in heterogeneous catalysts to be studied on different length scales simultaneously. The coupling of these techniques will also broaden the applicability of diffusion NMR to study porous systems in an industrial setting by providing the possibility of easily controllable catalytic loading with sample sizes which provide useable NMR signal-to-noise ratios.[3]

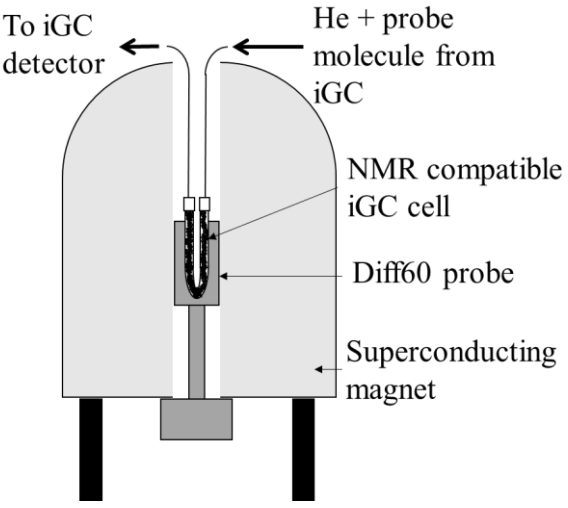

Figure 1: Schematic diagram of coupled iGC and diffusion NMR setups.

References: [1] Kärger, J. , Ruthven, D. M. and Theodorou, D. N. (2012). Medium- Pore (Ten- Ring) Zeolites. In Diffusion in Nanoporous Materials (eds J. Kärger, D. M. Ruthven and D. N. Theodorou).
[2] S. Mohammadi-Jam and K.E. Waters, Adv. Colloid Interface Sci., (2014), [212], 21-44.
[3] K. Banas, F. Brandani, D.M. Ruthven, F. Stallmach and J. Kärger, Magn. Res. Img., (2005), [23], 227-232.

Field-dependent effect of clays on NMR T_2 relaxation of sedimentary rocks by direct two-scale simulation

Yingzhi Cui, Igor Shikhov, Christoph Arns
School of Minerals and Energy Resources Engineering
University of New South Wales, Sydney, Australia

Introduction: Nuclear magnetic resonance (NMR) is an efficient, non-invasive technology for prediction of petrophysical properties on sedimentary rocks. Complex mineralogy of reservoir rocks and specifically clay minerals often result in unaccounted relaxation effects through the diffusion in internal magnetic field gradients and inaccurate relaxation regimes, while the standard interpretation assumes fast diffusion relaxation regime irrespective to the actual composition. We aim to improve existing NMR relaxation techniques by incorporating a direct simulation on artificial clay models into digital core approaches to evaluate effective diffusion and surface relaxivity at a given field strength.

Methods: The transverse relaxation responses are simulated using a random walk technique on 3-phase segmentations of micro-CT images of sandstone rock as a macro-scale morphology and a developed representation of kaolinite clay, which mimics morphology, porosity and characteristic scales deduced from SEM images as a microscale input. We firstly consider two phases, solid and saturated water. For three phases sample, we assign $T_{2,eff}$ of clay at different field strength to analyse clay effect over the magnetic field range of 2MHz to 80MHz. Discretization effects on calculated surface relaxivity and distribution of internal gradients were minimized by utilizing a set of images with different voxels size.

Results: The proposed model enables meaningful petrophysical interpretation of T_2 responses obtained at various field strength in situations when the localization regime becomes significant. The results show that the effect of clays on transverse relaxation of water saturated rocks is dominated by its micro structure and decrease with increase of the field strength. The higher discretization of the integral rock model enables to separate relaxation because of "true" surface relaxivity from contributions due to the high near-surface internal gradients and evaluate the effects of these gradients.

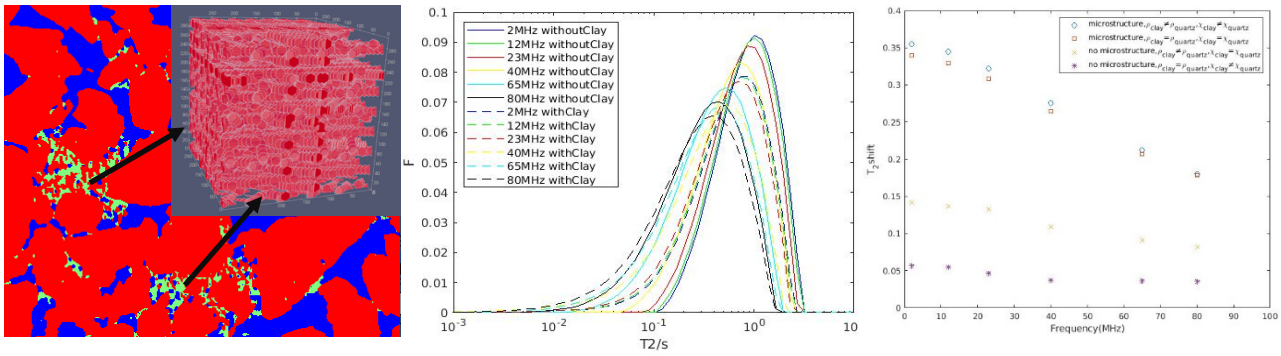

Fig. 1 (left): Bentheimer segmentation, blue is the pore space, red is the solid and green is clay. The inside window shows the kaolinite model witch mimic the clay micro structure. Fig. 2 (middle): Transverse Relaxation time in different field strength. Fig. 3 (right): Clay effects in different conditions under different field strength.

References:

[1] Hürlimann M D, J. Magn. Reson. (1997).
[2] Mitchell J, Phys. Rev. E (2010).
[3] Arns C, NJP. (2011). [4] Valckenborg R M E, Phys. Rev. E (2002).

Identification of physical properties governing relaxation process in saturated rocks by matching experimental T2 distributions and CT-image based NMR simulation through surrogate-assisted particle swarm optimization

Rupeng Li[1], Igor Shikhov[1], Christoph Arns[1]
[1]University of New South Wales, Sydney, Australia

Introduction: Petrophysical interpretation of NMR relaxation responses can be enhanced by extracting phase specific physical properties such as surface relaxivity, susceptibility, effective diffusion coefficient, etc., from CT-image based NMR random walk simulation, when both produce the same magnetization decay or T2 distribution [1]. A typical routine to handle this inverse problem when observations are available is via simulation-based optimization [2]. However, the number of decision variables may exceed 10 or 20 depending on image segmentation, and it is less practical to optimize for even 10 decision variables simultaneously with standard evolutionary algorithm when thousands of computationally expensive simulations are required.

The Optimization Framework: In this work, we propose a numerical approach to identify those properties by minimizing the mean square error (MSE) between the T2 distribution of that inverted from NMR and that from NMR measurement using surrogate-assisted evolutionary algorithms (SAEAs). The parallelized surrogate-assisted particle swarm optimization with committee-based active learning (CAL-SAPSO) estimates the fitness of the candidate solutions using ensemble-based surrogates consisting of a polynomial response model (PR), a radial base function network (RBF) and a Kriging model approximated from real simulation dataset and it queries for the evaluations of both solutions with the most uncertainty and promising fitness to update the surrogates iteratively, which significantly reduce 90% of the required realizations and thus making computationally determining physical properties practical [3]. A local surrogate model is incorporated to exploit the optimum in the area constrained by the solutions with top 10% best fitness leading to further reduced MSE with better matching and parameter identification.

Implementation: The NMR random walk simulation is initialized in the scenarios the same with the experiments except for the unknown physical parameters of interest: surface relaxivities, effective diffusion coefficients, and susceptibility for each phase, i.e., pore, quartz, clay, etc. The unknown physical properties are optimized using CAL-SAPSO in a limited computational budget and that the MSE converges to a minimum efficiently. We investigate the surface relaxivities and diffusion coefficient of both sandstones and carbonates: Bentheimer sandstones, Leopard sandstones, Berea sandstones and Indiana Limestone, with 3-10 unknowns each.

Results & Conclusion: Results show that by employing CAL-SAPSO a good agreement between simulated and observational T2 distributions are achieved with the corresponding MSE on average reaching a level of 10^{-2}, when a range of parameters are subsequently identified. It is concluded that when the observation is available, the CAL-SAPSO is capable of extracting physical properties by matching experiments closely, enhancing the petrophysical interpretation of NMR relaxation responses.

References:

[1] Arns, C. H., AlGhamdi, T., & Arns, J. Y. (2011). New J. Phys. 13.1 (2011) 015004.
[2] Gosavi, A. Simulation-based optimization. Berlin: Springer, 2015.
[3] Wang, H., Jin, Y., & Doherty, J. IEEE Trans. Cybern. 47.9 (2017) 2664-2677.

Spatially-resolved T2 distribution mapping in heterogeneous rock model with phase encode MRI

Yushi.Cui, Lizhi.Xiao, Guangzhi.Liao, Yan.Zhang, Jie.Wang
China University of Petroleum, Beijing, China

With the development of Magnetic Resonance Imaging (MRI) technology, it has been one of the important methods to study pore structure of porous media. Different from the T_2 distribution of the whole rock sample obtained by traditional Nuclear Magnetic Resonance (NMR) core analyzer, MRI can obtain the spatially-resolved T_2 distribution of rock samples, which can better guide the NMR response characteristics of heterogeneous rock model.

The most common methods for measuring spatially-resolved T_2 distribution are frequency encoding method[1] and phase encoding method[2]. In order to aviod image artifacts and difficulty in observing and quantifying short T_2 lifetime species caused by frequency encoding method[3], we use phase enchoding method for experimental measurements(Fig.1). The phase-encoded imaging pulse is implemented by applying a linear gradient based on the CPMG pulse sequence, That is, a set of gradient magnetic fields of different amplitudes are applied within a fixed time period δ after applying the 90° pulse. The acquired MRI signal contains a set of experimental results with different phases, and the spatially-resolved T_2 distribution is obtained by inversion of Fourier Transform(FT) and Inverse Laplace Transform inversion(ILT)[4].

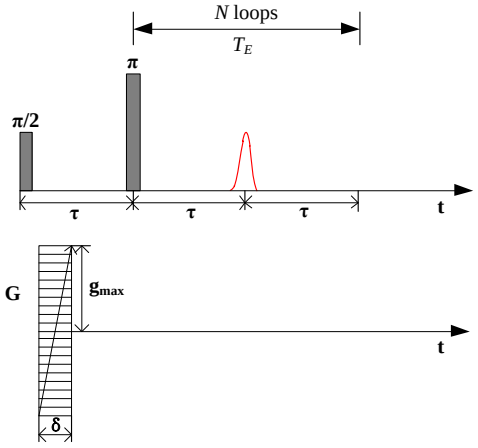

Fig. 1: One-dimensional phase-encoded pulse sequence

4 types of heterogeneous glass bead models were measured them with Oxford GepSpec NMR Rock Core Analyzer instrument. After inversing the data, the NMR spatial response characteristics of different heterogeneity models were observed. Combined with the response characteristics, the dolomite sample and conglomerate sample were also measured and analyzed, and the analysis results were consistent with the CT scan results. In addition, the method is better consistent with the logging instrument. While improving the resolution, it also avoids the influence of instrument motion on the measurement. It has good practicability for studying the low field NMR response of the rock heterogeneity model.

References:

[1] Haacke E M, Magnetic Resonance Imaging. (1999).
[2] Petrov O V, Journal of Magnetic Resonance. (2011).
[3] Vashaee S, Measurement Science & Technology. (2015).
[4] Huabin Liu, Doctor of Philosophy. (2015)

Data Processing and Software Research of Nuclear Magnetic Resonance Logging While Drilling

Y. Dong[a], G.Z. Liao[a], L.Z. Xiao[a]

a. State Key Laboratory of Petroleum Resources and Prospecting, China University of Petroleum, Beijing, China

Nuclear magnetic resonance logging while drilling(LWDNMR) [1-2]can obtain the information of undisturbed formation in real time while drilling, due to the influence of instrument motion and the limit of data transmission rate, LWDNMR data processing is very different from wireline logging. In order to design the LWDNMR data processing flow, the characteristics of LWDNMR data is researched and studied, it is of great significance for accurately acquiring the formation information and improving the logging quality.

Based on the differences between wireline nuclear NMR logging[3] and LWDNMR, this paper proposes and implements three data compression algorithms that can be applied to downhole for the problem that the LWDNMR data is large and difficult to transmit in real time[4]. At the same time, the effects of compression algorithm, signal-to-noise ratio, inversion algorithm and compression point on the inversion results are compared and analyzed. Then, according to the characteristics of the LWDNMR data, comparing the differences between the wireline NMR data processing and LWDNMR data processing, the data processing flow suitable for LWDNMR is designed.

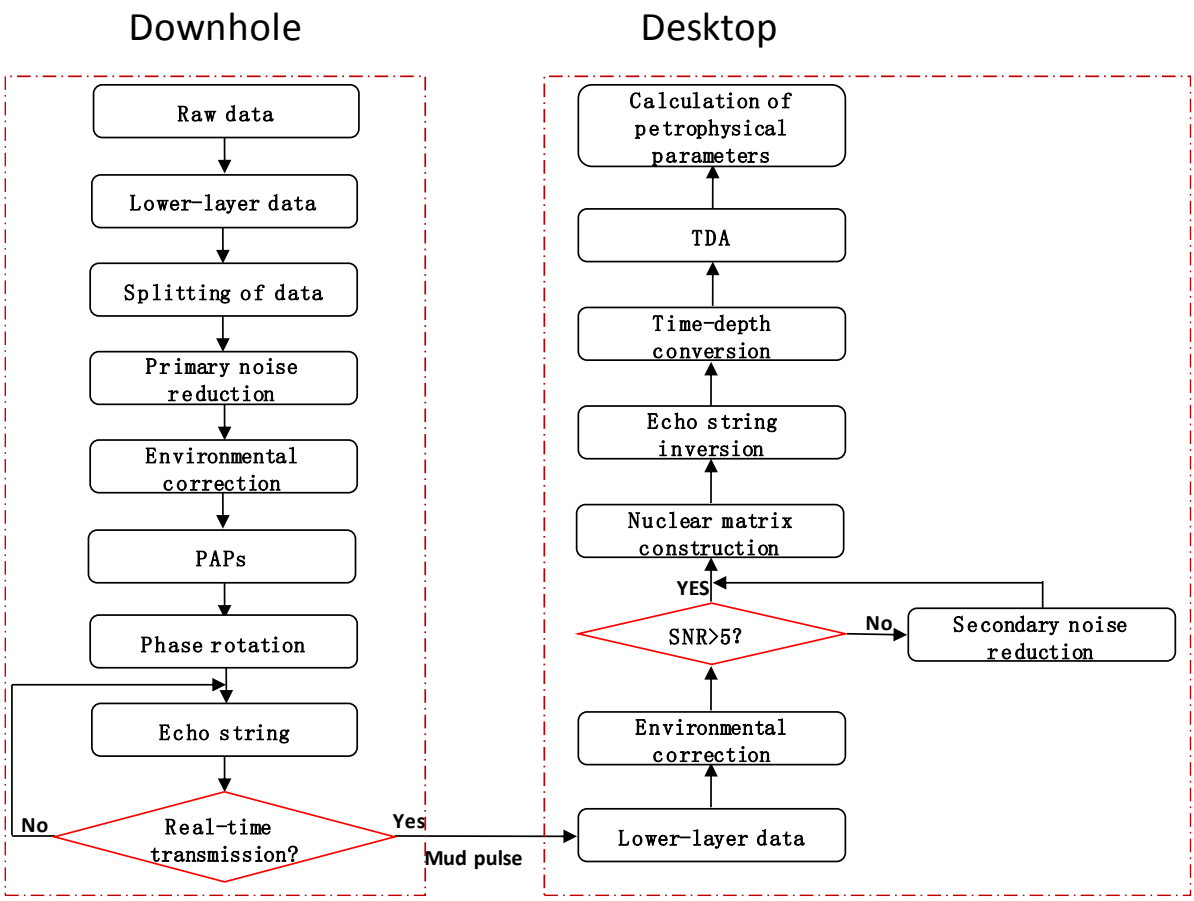

Figure 1- Flow chart of LWDNMR Logging data processing

Finally, Based on the above compression algorithm and data processing flow, a data processing software for LWDNMR is designed. The software relies on MATLAB as the system platform to integrate various algorithms into nine functions: data management, preprocessing, data compression, data inversion and output, et al. for third-party users to use, The software is simple to operate, friendly interface, and short in data processing time. The entire operation process only needs to input several key parameters to complete the refinement processing of LWDNMR. At the same time, the numerical simulation is used to construct the LWDNMR mode to verify the reliability of the software, the data processing results are consistent with the stratigraphic model and the intended design is achieved.

References:

[1] BARGACH S, FALCONER I, MAESO C, et al. Real-time LWD: logging for drilling[J]. Oilfield Review, 2000, 12(3): 58-78.

[2] ALVARADO R J, DAMGAARD A, HANSEN P, et al. Nuclear magnetic resonance logging while drilling[J]. Oilfield Rev, 2003, 15(2): 40-51.

[3] DEPAVIA L, HEATON N, AYERS D et al. A next-generation wireline NMR logging tool. SPE Annual Technical Conference and Exhibition, Denver, Colorado, USA, 2003, SPE 84482.

[4] DRACK E D, PRAMMER M G, ZANNONI S et al. Advances in LWD nuclear magnetic resonance.SPE Annual Technical Conference and Exhibition, New Orleans, Louisiana, 2001, SPE 71730-MS.

Characterization of porous media in intermediate diffusion regime by spherical pore structure

Zhou Yu, Yan Zhang, Lizhi Xiao, Guangzhi Liao
China University of Petroleum, Beijing, China

Nuclear magnetic resonance measurements (NMR) of spin relaxation and diffusion have been used extensively to determine pore size distribution and molecular exchange in porous media [1, 2]. Generally, various 1D and 2D Laplace NMR methods were applied to extract pore information under the validity of fast diffusion regime. For instance, the pore length scale, surface-to-volume ratio (S/V) of porous materials can be obtained by measuring the spin relaxation [3]. However, there are also conditions that the intermediate or slow diffusions regimes are applied, such as large pores or strong surface relaxation [4]. Consequently, the equation derived based on the fast diffusion assumption cannot be used to obtain pore structure and fluid information in these cases. Therefore, the average pore size of outside the fast diffusion regime were estimated by cylindrical pore structure [5].

Here a new method is used to characterize porous media in intermediate diffusion regime. First, the T_2-T_2 signals of spherical pores in different diffusion regimes are calculated according to the eigenmode formalism, and the T_2-T_2 signal coefficient matrix is obtained. Given the T_2-T_2 signals of a spherical pore calculated in eigenmode formalism, the pore size-surface relaxivity correlation maps in intermediate diffusion regimes are obtained by non-negative least squares inversion. Then, in order to characterize the more complex three-dimensional porous media, the T_2-T_2 signals of periodic stacked pore and randomly stacked pore models in intermediate diffusion regime are simulated by the random walk algorithm, and the pore size-surface relaxivity maps are respectively inverted, in which the characterization results are all good. Finally, the pore size and surface relaxivity of the sample are estimated by inversion after measuring the T_2-T_2 signal of the uniform particle size glass bead samples. Here are some a-ρ correlation maps results: Fig. 1(a) shows result of spherical pore with pore size of 200 μm and surface relaxivity of 25 μm/s. Fig. 1(b) shows result of periodic stacked pore with sphere radius of 200 μm and surface relaxivity of 25 μm/s. Fig. 1(c) shows result of randomly stacked pore with sphere radius of 200 μm and surface relaxivity of 25 μm/s. Fig. 1(d) shows result of glass bead sample with particle diameter of 400 μm. In general, this method can roughly characterize porous media in intermediate diffusion regime with a relatively uniform pore size distribution.

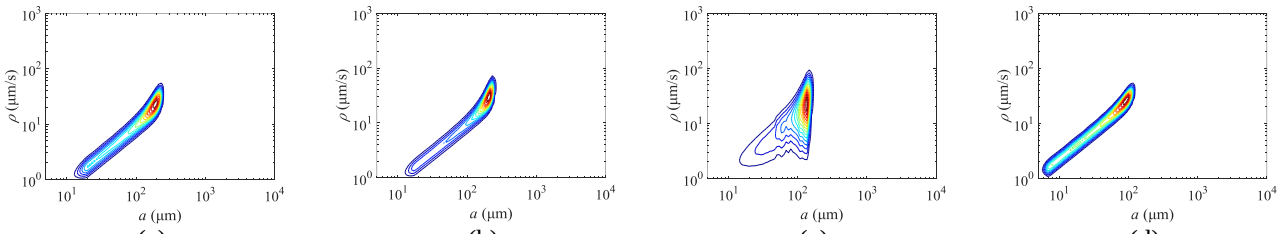

Fig. 1. (a) a-ρ correlation map of spherical pore. (b) a-ρ correlation map of periodic stacked pore. (c) a-ρ correlation map of randomly stacked pore. (d) a-ρ correlation map of glass bead sample

References:

[1] Brownstein, Phys. Rev. (1979).
[2] Washburn, Callaghan, Phys. Rev. (2006).
[3] Keating, Knight, Geophysics. (2012).
[4] Valfouskaya, Adler, Thovert, Fleury, J Colloid Interf Sci. (2006).
[5] Müller-Petke, Dlugosch, Lehmann-Horn, Ronczka, Geophysics. (2015).

Correlation of magnetic resonance imaging and high-resolution X-ray tomography to characterise pore size distributions in polymeric open – cell sponges

G. M. Cimmarusti [1], A. Shastry [2], M. N. Boone [2], V. Cnudde[2], M. M. Britton [1].
[1]School Of Chemistry, University of Birmingham, Birmingham, UK
[2] Department of Physics and Astronomy, Ghent University, Gent, Belgium;

Introduction: Applications of polymeric sponges are extensive, ranging from cleaning [1] and filtration [2], to applications in medical procedures [3]. The specific properties of such foams, such as pore size and connectivity, are dependent on material and production methods. Magnetic resonance imaging (MRI) and high resolution X-ray computed tomography (μCT) offer complementary information about the structure and properties of porous media [4, 5]. While μCT can directly map the 3D structure of a porous media [5], MRI probes the 3D pore structure indirectly, through the fluid contained within [6,7]. Additionally, MRI is able to measure the diffusion of the fluid within the system, providing an understanding of transport within the pore network [8, 9]. Thus, the use of μCT and MRI, allows the characterization of the foam structure heterogeneity and provide a better understanding on how this can influence the behaviour of such foams in different applications. In this study, we have employed MRI, in combination with μCt, to characterize the structure of polymeric open–cell foam and to determine how it changes upon compression. The distribution of T_2 nuclear magnetic resonance (NMR) relaxation times for water, within a range of open-cell sponges, have been measured and correlated with the average pore size distribution determined by μCT, as a function of compression.

Methods: A total of nine cylindrical cores of 1.53 cm diameter and 4 cm length were extracted from three separate sponges. Micro – CT and MRI analysis were performed on each core, both compressed and uncompressed. For the μCT experiments, 2401 projections were acquired over the full 360° rotation. For the MRI, each core was saturated with 7 dh water, and T_2 relaxation maps were acquired using a RARE pulse sequence.

Results and Discussion: Micro – CT data show a range of pore sizes within each core (from 40 to 2000 μm), and a variation of the pore size distribution between cores. MRI results display a difference in the T_2 relaxation time distribution between cores that corresponds with μCT. In particular, when the average pore size is larger, the average T_2 relaxation time is higher. Upon compression, μCT and MRI results show a shift of the pore size and T_2 distributions towards lower values, respectively.

Conclusion: This work demonstrates that information from μCt and MRI can be combined to characterize pore structure in polymeric open – cell foams. Furthermore, this study shows that there is a variation of the average pore size within single sponges, as well as between sponges.

References: [1] Starry, *US patent No. 3345669* (1967). [2] Q. Ma et al., *Small* 12 (2016) 2186. [3] Itoh ,*Us patent No. 5368590* (1994).[5] Cnudde and Boone, *Earth Sci. Rev.* 123 (2013)1. [6] Szayna at al.,*Solid State Nucl Magn Reson* 118 (1999) 99. [7] Kose, *J Magn Reson A* 118 (1996) 195 [8] M.M Britton, *eMagRes* (2011). [9] Vallatos et al., *Ind. Eng. Chem. Res.*, 54(2015) 6825.

Study on the molecular interaction of pore surface in tight sandstone by NMR

Hanlin Liu[1], *Guangzhi Liao*[1], *Lizhi Xiao*[1], *Yan Zhang*[1]
[1]China University of Petroleum, Beijing, China

With the increase of economic benefits brought by the exploitation of unconventional resources, the study of tight sandstone has been paid more and more attention. However, there are still serious water production problem in the process of producing gas after fracturing in the high-quality tight sandstone reservoir showed by Well-logging reservoir evaluation.

Low-field NMR method can play a crucial role in tight sandstone evaluation, because it can provide important information such as the distribution of water in rock. The majority of the measurements have been standard transverse (T_2) relaxation experiments, because the majority of dipolar interactions in conventional, arising from heteronuclear dipolar coupling between fluid molecules and paramagnetic impurities on the pore, can be refocused by a spin echo. However, tight sandstones have only a few percent porosity and millidarcy permeabilities, the pore sizes are typically in the micro-nanometer range, leading to very short relaxation times. In addition, a significant amount of the porosity in tight sandstone resides in micro-nano pores, giving rise to the homonuclear dipolar coupling that cannot refocused by a spin echo. In this paper, we present a new approach using solid echoes in the measurement of T_2 that addresses some of the challenges encountered. Combining these methods with T_2-spin echo measurements provides a more complete assessment of the tight sandstones. The T_2-solid echo measurements produce additional signal in the tight sandstone samples compared to the standard methodology, indicating the presence of the homonuclear dipole coupling. By establishing the molecular model of bound water and the interaction in the magnetic field, shown in Fig. 1, the mechanism of the homonuclear dipole coupling can be better understood. The additional signal in the tight sandstone sample, shown in Fig. 2, can provide the clay and the irreducible water saturation information in the rock, shown in Fig. 3. Although this study focused on low-field, this technique will also have great significance for the angiography in medical imaging.

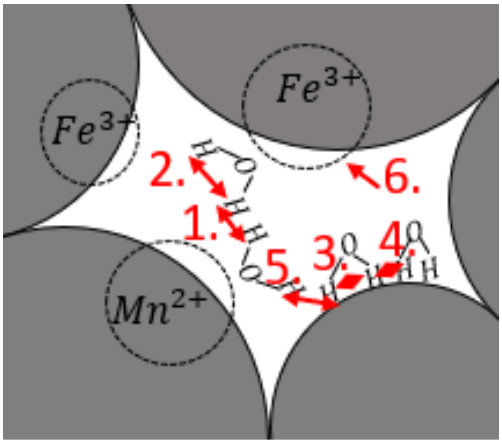

Fig. 1: The interaction of hydrogen atoms in a magnetic field in a pore. (1. Unrestricted inter molecular dipole coupling, 2. Unrestricted intramolecular dipole coupling, 3. Restricted intramolecular dipole coupling, 4. Restricted inter molecular dipole coupling, 5. A dipole coupling between a restricted and a unrestricted molecule, 6. the effect of paramagnetic ions.)

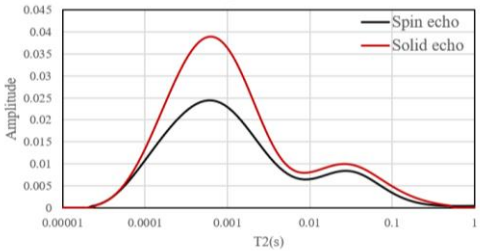

Fig. 2: tight sandstone T_2-Spin echo and T_2-Solid echo.

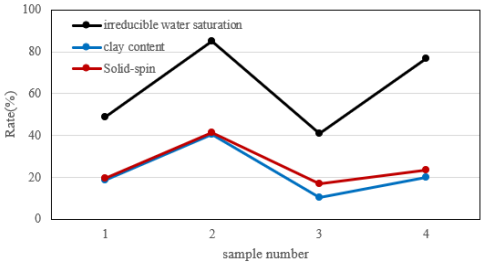

Fig. 3: Relationship among the difference between solid echo and spin echo, clay content and irreducible water saturation.

References:

[1] Peng, INT J MIN MET MATER. (2005).
[2] Washburn, CONCEPT MAGN RESON A. (2015).
[3] Birdwell, ENERG FUEL. (2015).

2.5D spatially resolved 3D Laplace NMR for porous media

Yan Zhang[a], *Lizhi Xiao*[a,b]
[a] State Key Laboratory of Petroleum Resources and Prospecting,
China University of Petroleum, Beijing, 102249, China
[b] Harvard SEAS-CUPB Joint Laboratory on Petroleum Science, Cambridge, MA 02138, USA

Spatially resolved NMR refers to measurements that extract information from a sample within a certain region, which can be obtained by NMR imaging. It is well known that multidimensional Laplace NMR is a powerful method to characterize porous sample but only integral information is obtained. Combining multidimensional Laplace NMR and MRI can extract abundant information in a local region of the sample. Zhang et al. obtained spatially resolved D–T_2, $G_{\text{int}}{}^2D$–T_2 and pore size – T_2correlation of porous media with back-projection imaging method to accelerate the experiments [1-3]. More detailed information can be obtained by extending such experiments to higher dimension (whether in Laplace or Fourier domain) with proper accelerated methods.

In this research, compressed sensing (CS) was used for shortening measurement times. We combined 3D Laplace NMR (D–T_1–T_2) and 2.5D MRI methods to extract local information of porous media in detail. The CS is applied both in Laplace and Fourier domain. Two kinds of samples were measured: glass-bead model sample and sandstone sample, which are saturated with water and two kinds of oil. The pulse sequence is shown below in Figure 1. The results show heterogeneous oil/water distribution and pore structure information in different region of the sample.

Reference

[1] Y. Zhang, B. Blümich, Spatially resolved D-T2 correlation NMR of porous media, J. Magn. Reson. 242 (2014) 41-48.
[2] Y. Zhang, B. Blümich，Gint2D - T2 correlation NMR of Porous Media，J. Magn. Reson. 252 (2015) 176-186.
[3] Y. Zhang, L. Xiao, G. Liao, Spatially resolved pore-size - T2 correlations for low-field NMR, Microporous and Mesoporous Materials 269 (2018), 142-147.

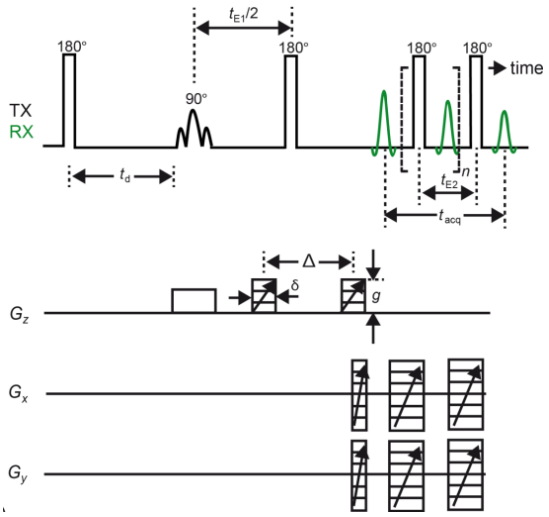

Investigation of high-permeability channels using computational fluid dynamics and magnetic resonance imaging

G. Solcia[a], B.U. Foerster[a], M.B. Andreeta[a], T.J. Bonagamba[a] and F.F. Paiva[a]

[a]São Carlos Institute of Physics, University of São Paulo, CP 369, 13560-970, São Carlos, SP, Brazil

Introduction: Acidification is a technique applied to increase the productivity of a well in a carbonate reservoir. It creates high-permeability transport channels denominated wormholes [1]. To investigate the outcome geometry of these channels, a non-invasive and systematic method is required. Besides the resolution limitation of Magnetic Resonance Imaging (MRI), it can provide robust structural information about these wormholes, with the additional advantage of allowing fluid flow studies. This can provide complementary information to Computational Fluid Dynamics (CFD) studies. In this work, we present the first results of CFD simulations using an OpenFoam [2] incompressible and laminar flow solver in an MRI-based mesh of a wormhole.

Methods: The acidification process was performed at the Petrobras research facility CENPES (Rio de Janeiro, Brazil) using 1.5% hydrochloric acid with a flow rate of 1 ml/min. Samples were saturated with deionized water and images were acquired on a Bruker Biospin Avance III spectrometer at 2 Tesla. Atropos [3], distributed with Advanced Normalization Tools (ANTs) was used to assemble the wormhole in combination with the Computational Geometry Algorithms Library (CGAL) for triangulated surfaces generation. The snappyHexMesh was used to generate a 3D mesh in OpenFoam from a Stereolithography format. A simpleFoam for an incompressible, Newtonian and laminar flow solution was used in a pressure gradient boundary condition.

Results and discussion: Figure 1 shows a flow simulation obtained with a pressure gradient of 0.2 Bar between outlet and inlet in laboratory conditions. Velocity drop in ramifications was expected due to their closed boundary, representing a zero permeability surrounding media. It can be also noted the velocity increase with the radius reduction as predicted by Hagen-Poiseuille solution, although in a complex geometry restriction. Through the scalar velocity field, an average flow rate of 28 ml/min was obtained.

Conclusion: We show that the simulation of incompressible and laminar flow in wormholes is possible using MRI data and OpenFoam. Direct visualization of velocity fields allows the analyses of different boundary conditions for flow rate. This preliminary study presents the perspective of CFD and MRI integration for flow analysis in more realistic conditions. The perspective includes direct measurement of fluid flow in the wormhole using MRI and the comparison of the patterns obtained with MRI and CFD.

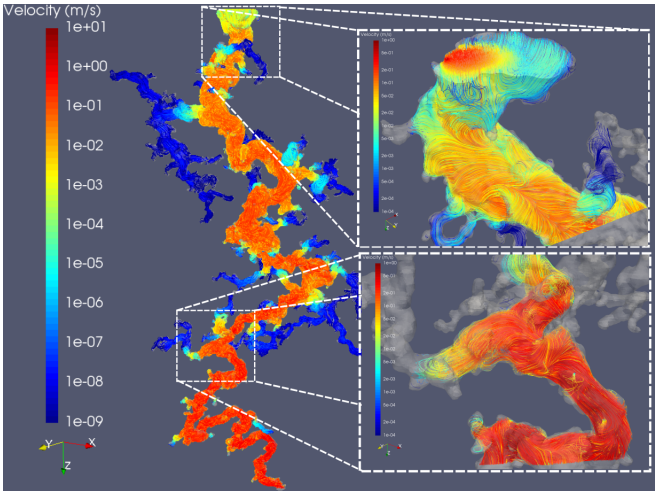

Fig. 1: Steady state streamlines of fluid velocity in a representative wormhole. Expanded regions have a modified colormap range of $1e^{-4}$ to 1 m/s.

References: [1] C. N. Fredd and H. S. Fogler, SPE J., 3:34-41. (1998). [2] H. G. Weller et al., 12(6):620-631. (1998). [3] B.B. Avants et al., 9(4):381-400. (2011).

MRI and NMR Studies of a Seawater Spray Ice Formation

G. Wilbur, B. MacMillan, I.V.Mastikhin[a]

[a]MRI Centre, Department of Physics, University of New Brunswick, Fredericton, NB, Canada

Introduction: Seawater spray and precipitation are two main sources of icing and ice accumulation in cold ocean regions, presenting a major challenge for shipping and operating maritime equipment (oil rigs, wind turbines, etc) [1]. Despite its importance, there is a limited number of analytical techniques to study seawater spray ice formation. MRI is known for its non-invasive capabilities in measurements of a solid ice [2,3]. In this work, we investigate the potential of MRI as an analytical measurement technique for studies of the seawater spray ice by performing series of 3D MRI and T1-T2 mapping measurements for three different freezing regimes characterized by different initial freezing temperatures and the temperature range.

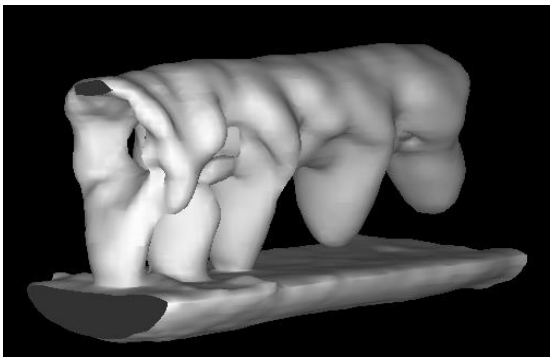

Fig. 1: A surface-rendered MR image of seawater spray ice (high initial t°) with water flowing below.

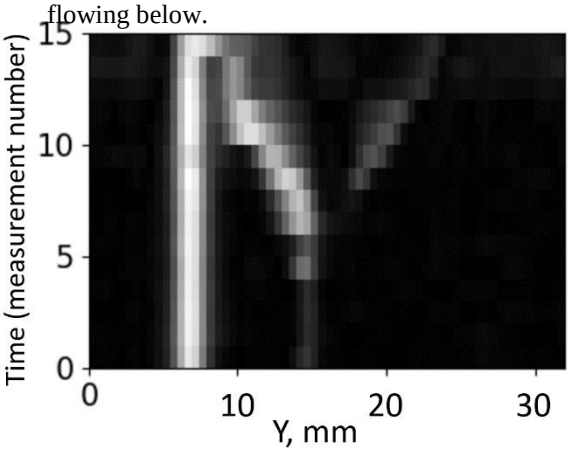

Fig. 2: Vertical 1D-profiles through the sample centre vs time (high initial t° regime).

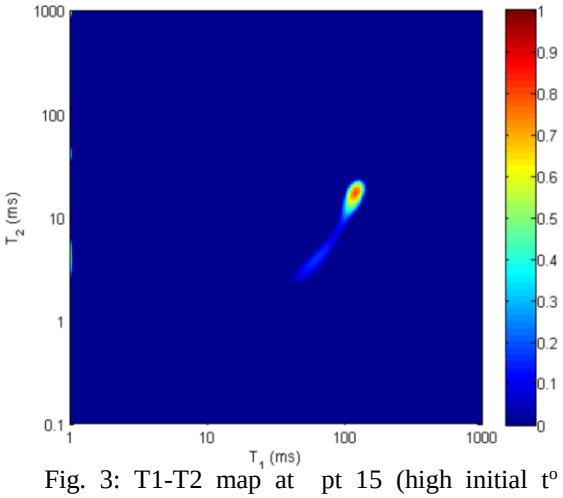

Fig. 3: T1-T2 map at pt 15 (high initial t° regime). The strong peak at longer T1/T2 is from the unfrozen water, the weaker one is from the brine in the ice

Methods: 3D Conical SPRITE for imaging (6x6x12 cm XYZ FOV), IR-CPMG sequence for T1-T2, diffusion and FID sequences, with the total measurement time of 6 min per temperature point. A prechilled artificial seawater was sprayed upon a cylindrical glass tube cooled down with cold nitrogen. The temperature changed from +5 to -35°C.

Results and Discussion: The signal detected with MRI/NMR comes from the pockets of brine in the forming ice, and the unfrozen water, with the brine signal decreasing as the temperature drops. 3D MRI show different freezing patterns and temperature gradients depending on the initial freezing temperature and the surface geometry (up vs down, Fig.2). T1-T2 maps show strong changes in relaxation parameters as the freezing progresses, indicating changing environment for the brine in the growing ice (Fig.3).

Conclusion: MRI can be employed as a reliable analytical tool for laboratory studies of the seawater spray ice formation, permitting data collection non-invasively both on the temporal and spatial changes during freezing. FID and T1-T2 measurements provide relaxation information on the conditions of brine in the ice pockets during the ice formation. This information can be further utilized for applications of portable NMR instruments in in-situ studies of the freezing phenomena.

Acknowledgements: Natural Sciences and Engineering Research Council of Canada (I.M.).

References:

[1]A.R. Dehghani-Sanij, S.R. Dehghani, G.F. Naterer, Y.S. Muzychka, Ocean Eng. 143 (2017) 1–23.

[2]M.W. Hunter, R. Dykstra, M.H. Lim, T.G. Haskell, P.T. Callaghan, Appl. Magn. Reson. 36 (2009) 1–8.

[3]J.R. Brown, T.I. Brox, S.J. Vogt, J.D. Seymour, M.L. Skidmore, S.L. Codd, J. Magn. Reson. 225 (2012) 17–24.

Water diffusion pore imaging on a 14.1 T spectrometer using glass capillary phantoms and strong gradients

D. Ludwig[1], F.B. Laun[2], K.D. Klika[1], P. Bachert[1], T.A. Kuder[1]
[1] German Cancer Research Center (DKFZ), Heidelberg, Germany
[2] Institute of Radiology, University Hospital Erlangen, Friedrich-Alexander-Universität Erlangen-Nürnberg (FAU), Erlangen, Germany

Introduction: Diffusion pore imaging (DPI) enables direct measurements of arbitrarily shaped closed pores filled with an NMR-detectable medium [1–3]. The first implementation of DPI [1] made use of the long–narrow approach [4] in order to retrieve the phase information necessary for reconstruction of the pore space function. The main factor limiting DPI applications is the available gradient strength. In this study, we used a Bruker Diff30 Probe with $G_{\max} = 18$ T/m in the z-direction.

Methods: Glass capillaries of 3.5 mm length and inner diameter 25 µm were stacked horizontally inside a 5-mm NMR tube, i.e. with orthogonal orientation to the main magnetic field. The capillaries were filled with a saturated aqueous NaCl solution – necessary to weaken the susceptibility effects introduced by the glass capillaries – resulting in a free diffusion coefficient D = 1.48 µm²/ms for the water inside the capillaries. In order to disperse any residual NaCl solution on the outside of the capillaries, the NMR tube was filled with Flourinert. Also, it was necessary to split the long gradient of the long–narrow approach into a CPMG-like gradient pulse train separated by 180° pulses. The long gradient was split into 39 segments of 10.221 ms each yielding a total time of 400 ms. The narrow gradient had a duration of 1.9 ms. We used $G_{\max} = 2.7$ T/m resulting in $q_{\max} = 1370$ 1/mm. A schematic representation of the pulse sequence is presented in Figure 1A. q-Values were selected in order to match the available raster points of the gradient amplifier.

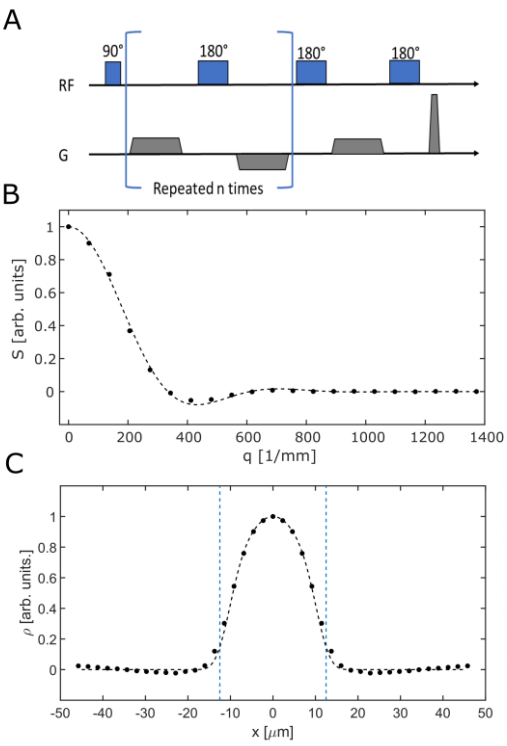

Figure 1: (A) Schematic representation of the CPMG-like long–narrow approach. (B) Signal and simulation as a function of the q-value. The experimental results are in good agreement with theory (dotted line). (C) The corresponding pore-space function and theory (dotted line) are again in good agreement.

Results and Discussion: Figure 1B shows the signal as a function of the q-value together with simulated data wherein it is seen that the experimental result agrees well with the simulation. Figure 1C shows the pore space function, which is the Fourier transform of Figure 1B. The pore space function clearly yields a diameter of 25 µm, though it is slightly smeared out at the edges.

Conclusion: The need for strong gradients is the main limiting factor of DPI. Nevertheless, we were able demonstrate the feasibility of DPI with an ultra-high gradient system using 25 µm capillaries without exploiting the full gradient strength available. This work may therefore pave the way to actual applications with µm-sized objects such as living cells.

References: [1] Hertel, PRE 87.3 (2013). [2] Hertel, PRE 92.1 (2015). [3] Bertleff, JMR 278 (2017). [4] Laun, PRL 107.4 (2011)

The bending of 17th century panel paintings induced by moisture

L. Pel, T. Arends
Eindhoven University of Technology, Eindhoven, The Netherlands

Wooden boards, joined together by glue, dowels, and crosspieces were the most extensively used supports for portable paintings until the early 17th century. Typically, some layers of gesso and/or fabric were added to serve as a carrier for the paint layer. Well-known masterpieces have been constructed accordingly, e.g., by da Vinci, Rubens, or Rembrandt, and as such they form an important part of our cultural heritage.
Since paint is much less permeable than wood, a panel painting can conceptually be approached as a board with an impermeable layer on one surface. Due to the hygroscopic nature of wood, a panel will exchange moisture with the ambient air upon changes in the relative humidity (RH). Consequently, the moisture content will be unevenly distributed throughout the thickness of the board which will result in differential expansion across the thickness, causing the wooden board to bend. This bending should be proportional to the asymmetry in the moisture distribution. This bending can give rise to permanent deformation or even failure, manifested, e.g., as cracks in a painting. Using a special Nuclear Magnetic Resonance (NMR) setup, which makes use of the magnet of a 1.5T whole body MRI scanner, we have studied simultaneously both the moisture distribution in an oak board during changing RH and the expansion and deflection. These results show that the asymmetry in the moisture distribution can be directly related to the deflection. In addition we have looked at the response of panel paintings to sinusoidal RH changes with different frequencies The material will have different behavior as function of the frequency, reflecting day/night or summer/winter cycles. Our goal is to come up with environmental criteria for panels paintings for fluctuation frequency, and amplitude in RH which are safe or potentially harmful.

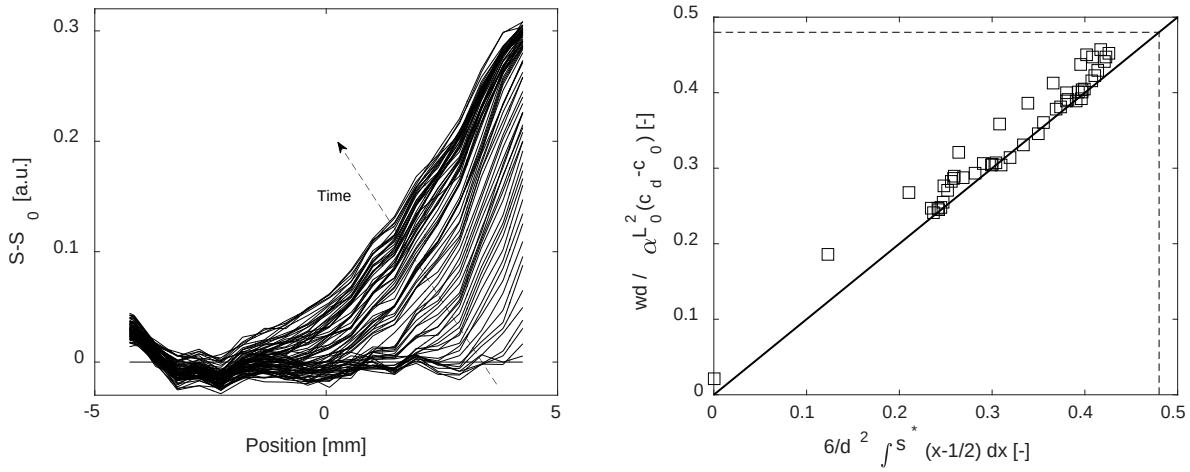

Figure 1: (Left) The measured moisture distribution profiles for a coated oak board and (right) the corresponding measured scaled deflection of its free end as a function of the asymmetry in the measured moisture content distribution

T_2 Analysis Using Artificial Neural Networks

T. Parasram, D. Xiao
University of Windsor, Windsor ON, Canada

Introduction: MRI is widely used as a non-invasive diagnostic technique to visualize the internal structure of biological systems. Quantitative analysis of the T_2 relaxation times will reveal molecular scale information. Conventional methods to extract such information require a large number of data points with high signal-to-noise ratio (SNR), which is not readily available in many applications [1-3].
Artificial neural networks (ANN) are a series of densely connected, simple information processing nodes which cumulatively map a set of inputs to several features, such as the coefficients of a function, which are to be predicted. They have proven to be powerful tools for solving complex nonlinear problems. We propose to use ANN's for the T_2 relaxation time analysis.

Methods: The general signal equation for *n* decay components is

$$S(t) = \sum_{i=1}^{n} a_i e^{-\frac{t}{T_{2i}}}, \quad \text{Eq. 1}$$

where $S(t)$ is the signal at time t, a_i and T_{2i} are the amplitude and T_2 relaxation time of the *i*th component.
Numerous signal decay curves were generated by simulation. These decay curves were employed as the inputs to the ANN's, and the a_i's and T_{2i}'s were the outputs from the ANN's.

Results and discussion: The ANN's were trained on 25 sets of 7000 simulated decay curves with 5 different SNR's, and with 5 different input sizes, to recover the amplitude coefficients and T_2 relaxation times, for a two-component signal model. The traditional least squares fitting (LSF) method was employed as a comparison. ANN outperformed LSF in all the simulation datasets. In particular, with very low input data SNR, ANN produced reliable results while LSF failed, as shown in Figure 1 below.

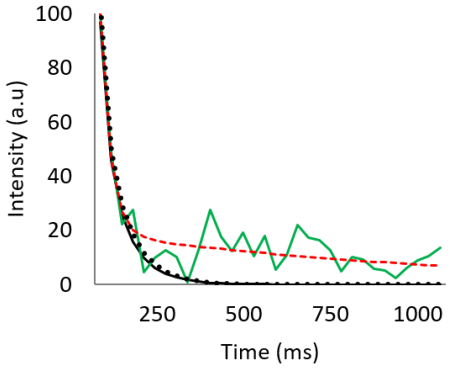

Fig. 1: A two-component signal decay (——) with high noise level (SNR = 15, ——) was processed with LSF (-------) and ANN (·····) to recover the signal. ANN yielded a reliable result, while LSF lead to large error.

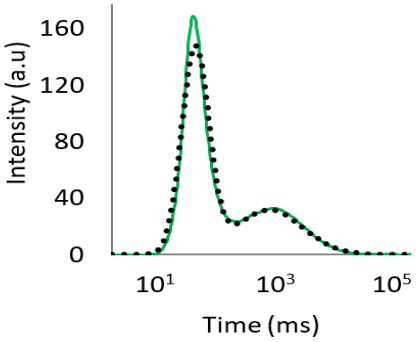

Fig. 2: T_2 distribution curve (——) generated by ANN, which agrees well with the original distribution data (·····).

ANN's were also trained to generate T_2 distributions, with high accuracy, as shown in Figure 2.

Conclusion: In this work, ANN's have been trained for T_2 relaxation time analysis. Discrete T_2 components and continuous T_2 distributions were considered. Results have shown increased accuracy compared to conventional methods, especially when the SNR is sub-optimal.

References: [1] Lamanna, Concepts Magn. Reson. Part A (2005). [2] Koay, J. Magn. Reson. (2009). [3] Berman, Concepts Magn. Reson. Part A, (2013).

Setting of geopolymer binders studied by NMR

N. Nestle[a], *J.P. Merkl*[b] *G.H. Nguyen*[c], *J.B. d'Espinose*[c]

[a]BASF SE Materials Physics and Analytics, Ludwigshafen, Germany, [b]BASF Construction Chemicals, Trostberg, Germany, [c]École Supérieure de Physique et de Chimie Industrielles | ESPCI Paris, France.

Introduction: Geopolymer binders have received increasing attention as a construction material in recent years. Reasons for this are diverse and include the lower CO2 footprint and better transport barrier performance for many substances compared to standard cementitious binders. In contrast to cement-based materials which have been studied quite intensively by a wide range of NMR methods over the last decades, geopolymeric materials have received much less attention in this field. Most published work is on Al NMR [1-3], while proton NMR relaxometry is even more scarce [4]. One reason for this might be the occurrence of some surprising apparent relaxation effects which are due to the large internal magnetic field gradients in these materials [5]. In some recent work, we have decided to revisit this matter using model systems without such artifacts and based on these results also to explore more complex, real systems.

Experiments: The main experimental tool used in our study were T2-measurements using the SE-PCMG method [6]. Selected samples were studied over extended periods of time and the effects of ambient drying of the samples at different points in time were studied as well. In the metakaolin model systems, also the effect of different Si/Na ratios was studied. While data quality and representativity of the NMR signal for the whole proton population contained in the samples proved to be excellent in the case of the model systems, the more realistic mortar formulations came with pronounced artifacts resulting from the diffusion effect in internal magnetic field gradients already described in [5].

Key learnings: Over the course of the setting process, a separation of the water population into increasingly heterogeneous sub-populations can be observed for most samples. This tendency includes both a complete expulsion of small amounts of water into macropores with almost free-water-like behavior (a few percent of the overall water population) and a broadening of the distribution of relaxation times for the water inside the rest of the pore system. The effects are observed in the model systems as well as in the real mortar systems with moderate internal gradient effects. Both effects are more pronounced in the systems with lower Si/Na ratio.

References: [1] Brus et al., Ann. Rep. NMR Spect. (2016), [2] Benavent et al. Cem. Conc. Res. (2016), [3] Favier et al. Cem. Conc. Res. (2013), [4] Xia et al., Mat. Lett. (2014), [5] Nestle et al. J. Appl. Phys. (2000); [6] Nestle et al. Anal. Chem. Act. (2009).

Homogenisation in high-level radioactive waste bentonites probed at sub-microscopic length-scales using ^{2}D μ-MRI.

Galina E. Pavlovskaya[1], Frank Scotti[2], Sean P Rigby[2], Thomas Meersmann[1], Katherine A. Daniels[3], Anthony Milodowski[3], Jon F. Harrington[3]

[1]Sir Peter Mansfield Imaging Centre, School of Medicine, University of Nottingham, Nottingham, NG7 2RD, UK; [2]School of Engineering, University of Nottingham, Nottingham, NG7 2RD, UK UK; [3]British Geological Survey, Keyworth, Nottingham, NG12 5GG, UK

Introduction: Concepts for geological disposal of high-level radioactive waste usually include bentonite buffer materials [1]. However, the long-term performance of the bentonites for the containment of the nuclear waste is being increasingly questioned due to specific issues associated with "homogenisation" occurring in these materials. Homogenisation is driven by erosion, variations in density and development of swelling pressure. However, the role of porewater pressure, it's spatial development and impact on swelling potential, self-sealing and permeability have yet to be adequately explored. We have developed novel ^{2}D μ-MRI methods to demonstrate that these governing hydration processes are indeed both complex and non-uniform in bentonites and natural materials homogenised in the laboratory setting and used for containment of radioactive waste in many European countries.

Experimental: Bentonites and natural materials used in this study were homogenized with D_2O. ^{2}D NMR imaging, combined with ^{2}D spin-echo T_2 spectroscopy was used to map out T_2 relaxation in these samples. Surface relaxivity of deuterium oxide was determined using beads with different diameters soaked in D_2O.

Results and Discussion: We have shown that T_2s in these materials are non-uniform and the distributions change as deuterium oxide progress toward the end of a core during homogenization as shown in Figure 1. Obtained values of T_2 were indicative of high structural heterogeneity. We further converted T_2 maps to pore size distribution maps to probe length scales of structural heterogeneities that occur in bentonites and natural materials during homogenization. Example of these maps are displayed in Figure 2 and demonstrate that the method captures structural irregularities that are lower than 2500 nm. These structural irregularities are not visible in high resolution X-CT images of these cores.

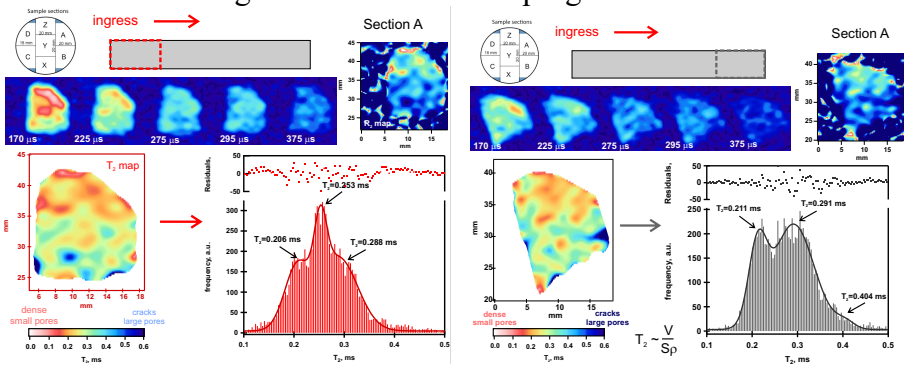

Figure 1. ^{2}D T_2 maps for a few values of spin-echo delays in bentonite. Note, that the T_2 distributions change obtained from T_2 maps change towards the end of the core in the direction of ingress.

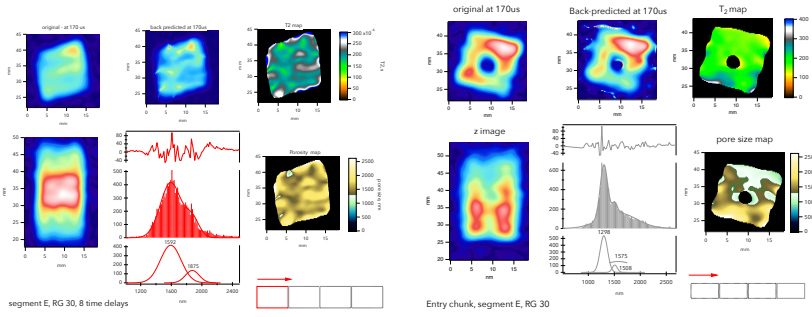

Figure 2. Pore size maps obtained from T_2 maps. Note, pore sizes a vary spatially and with ingress as expected from the changes in T_2.

Conclusions: ^{2}D MRI has a great potential to assess heterogeneity in man-made and natural clays. The information is vital for a proper choice of materials used in containment of the nuclear waste.

References: [1] Bao, *Caly Minerals*. **51** (2016) 237

Liquid specific changes in magnetic susceptibility induced internal gradients during displacement experiments in porous media.

Henrik Nicolay Sørgård, John Georg Seland.

University of Bergen, Department of Chemistry, Allegaten 41, N-5007 Bergen, Norway.

Introduction: Paramagnetic impurities present in several types of sandstones are responsible for the devastating line broadening observed in high field NMR [1]. Therefore, we have created a core sample model appropriate for high field measurements performed on a vertical bore Bruker Ascend 500 MHz spectrometer with a commercial 25 mm magnetic resonance microscopy (MRM) probe.

Methods: The sandstone model consists of pure quartz sand, with a heterogeneous particle size, compressed in a cell. The cell functions as a core sample holder and is equipped with inlet and outlet tubing, thus allowing for drainage and imbibition experiments without extracting the sample from the magnet. Here we study the liquid specific changes in magnetic susceptibility induced internal gradients (G_0) during drainage and imbibition experiments in samples with varying wettability. Using this model system reduces the line broadening so that the oil and water signals are actually directly distinguishable as seen in Figure 1A.

Results and discussion: We present spatially resolved G_0 distributions, from the water and the oil, obtained with a recently published pulse sequence [2]. Figure 1B shows an example of G_0 distributions around the imbibition front in an oil-wet sample. Oil and water distribution in a porous sample can be interpreted based on the internal gradient values in the separate fluids.

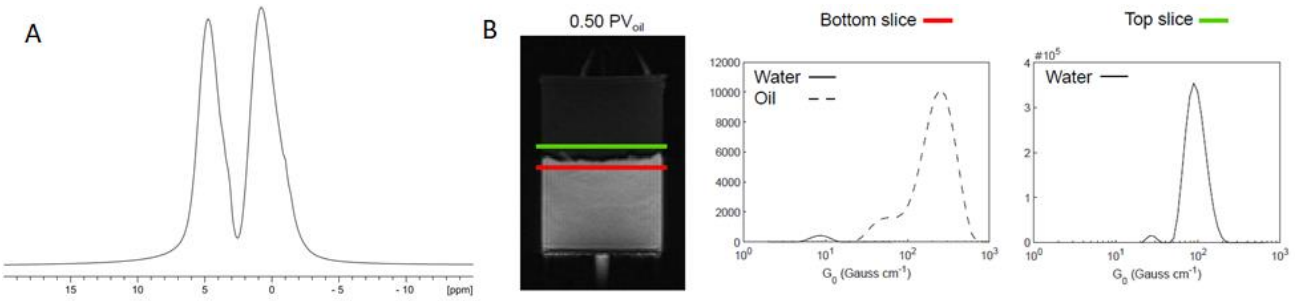

Fig. 1: (A) ^{1}H NMR spectrum, averaged over the entire sample after injecting 0.5 pore volumes of oil, acquired with a 90-degree single-pulse sequence. This shows that oil and water are distinguishable in the porous sample due to differences in chemical shift. (B) Spatially resolved G_0 distributions acquired from the water and the oil signal during oil imbibition in an oil-wet sample. The bottom slice (red) is located in the iso-center and the top slice (green) is located 4 mm above the iso-center.

Conclusions: We were successful in using liquid specific measurements of internal gradient, during drainage and imbibition experiments, to predict wettability in porous samples.

References [1] J. Mitchell, T. C. Chandrasekera, D. J. Holland, L. F. Gladden, E. J. Fordham, *Phys. Rep.*, (2013) [2] H. N. Sørgård and J. G. Seland, *J. Magn. Reson.*, (2019)

Investigation of the Structure of Geopolymer Based Cements with NMR Cryoporometry and Relaxation Exchange Spectroscopy

S. Mailhiot[1], J. Li[1], H.N. Sreenivasan[1], A. Kantola[1], P. Kinnunen[1], V.-V. Telkki[1]
[1]University of Oulu, Oulu, Finland

Introduction: Geopolymer cement is an alternative for Portland Cement that utilizes minimally processed materials or industrial byproducts to reduce the carbon footprint of concreate usage. Geopolymer cement is an aluminum silicate material in comparison to Portland cement which contains alumina and iron oxide. Two-dimensional (2D) relaxation correlation and exchange NMR have previously been used to characterize cement [1] but so far have not used to quantify the exchange rate in cement. Equations and methods for time domain fitting of T_1-T_2 data have been introduced and utilized in model systems [2]. In this work, we utilize the time domain fitting of T_1-T_2 data to quantify the exchange rate in geopolymer cements. The 2D relaxation data is complemented by NMR cryoporometry data to better investigate the porous structure.

Methods: We investigated three geopolymers with different water contents: Na_2O: Al_2O_3: SiO_2: H_2O = 1:1:4:15 (HW), 1:1:4:14 (MW) and 1:1:4:13 (LW). Samples were cured for 60 days and saturated in water for 8 days. T_1-T_2 and T_2-T_2 measurements were performed with a Magritek SpinSolve magnet operating at 43 MHz ^{1}H frequency. Time domain fitting of the T_1-T_2 data was performed using equations described in Ref. [2]. Fifty bootstraps were used with an SNR of 500 to estimate the mean and standard deviation of the solution. Cryoporometry experiments were performed with a Bruker vertical bore magnet operating at 500 MHz ^{1}H frequency. The temperature was varied from 170 K to 273 K with 76 steps. Spin echo data was measured with an echo time of 20 μs. Cryoporometry data was fit to the Gibb's Thomson Equation to find the pore size distribution.

Results: Two T_2 relaxation rates measured in water saturated geopolymer cement and the sample is therefore a candidate for study by T_2-T_2 exchange measurements. However, T_1-T_2 measurements show that one population has an effective $T_1 < 1$ ms, which makes probing the exchange by changing the mixing time in the T_2-T_2 exchange experiment infeasible. Time domain fitting of the T_1-T_2 data finds exchange times of 5.3 ± 0.15 ms, 4.2 ± 0.13 ms, and 3.1 ± 0.9 ms for the LW, MW, HW samples respectively. Cryoporometry data shows a single pore size, lending support to the previously proposed hypothesis [3] that the exchange is between wall and pore volume instead of pores of different sizes.

Conclusions: Using 2D relaxation NMR and cryoporometry, a sustainable cement with varying water contents was evaluated. We demonstrate that time domain fitting of T_1-T_2 data can be used to find the exchange time. The exchange time in geopolymer cement is dependent on water content. We hypothesize that exchange is between the pore wall and the pore volume.

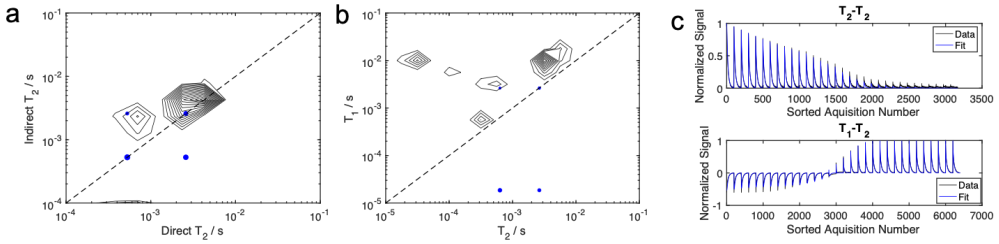

Figure 1- Inverse Laplace Transform of data (black) and eigenmodes of the fit (blue) for T_2-T_2 data (a) and T_1-T_2 data (b). Negative eigenmodes are predicted in the T_1-T_2 ILT. Comparison of the obtained data and fit results in the time domain (c). The fit from T_1-T_2 is compared to T_2-T_2 data to demonstrate that the data was fit correctly and can be used to predict T_2-T_2 exchange data.

References: [1] L. Monteith et al., Phys. Rev. E (2006). [2] R.D. Dorth et al., J. Chem. Phys. (2009). [3] P.J. McDonand et al., Phys. Rev. E (2005).

Monitoring Gas Hydrate Formation/Dissociation with Magnetic Resonance Imaging in a Metallic Core Holder

M. Shakerian,[1] A. Afrough[1], S. Vashaee[1], F. Marica[1], Y. Zhao[2], J. Zhao[2], Y. Song[2], B. J. Balcom[1]

[1]Univeristy of New Brunswick, Fredericton, [2] Dalian University of Technology, Dalian, China

Introduction: World-wide methane gas hydrate deposits are promising sources of energy. In the present work, methane hydrate formation and dissociation processes were studied employing an MR/MRI compatible metallic core holder at magnetic field of 0.2 T.

Methods: Hydrate formation occurred in water-saturated sand employed in the sample vessel, shown in Fig. 1b, at 1500 psi and 4 °C [1,2]. A hydrate-bearing sand pack, with 96% initial hydrate saturation, underwent dissociation by depressurization at 290 psi and 4°C. The sample, apparatus and MR/MRI measurements employed in the dissociation experiment were the same as that of the formation studies.

Results and discussion: Rapid 1D SPRITE MRI measurements [2] mapped the growth pattern of hydrate in the sand pack, as shown in Fig. 1a. Quantitative 3D π-EPI MRI measurements, shown in Fig. 2, revealed a variety of phenomena occurring during hydrate dissociation including water migration, bed failure, and crack growth. The bulk T_1-T_2 measurements, shown in Fig. 4, identified gas trapped in the pore space and estimated an excess pore gas pressure of 8200 psi. The peak P_4, interpreted as gas in the pore space, was also observed in the formation study.

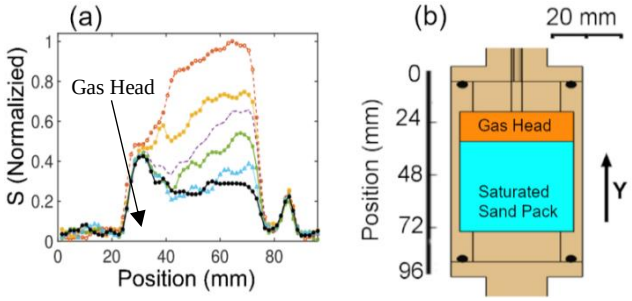

Fig. 1: (a) space and time resolved ^{1}H fluid content profiles of hydrate formation at 2, 2.25, 2.75, 3.45, 3.75 and 4 hours after introduction of the gas. (b) Schematic of the sample.

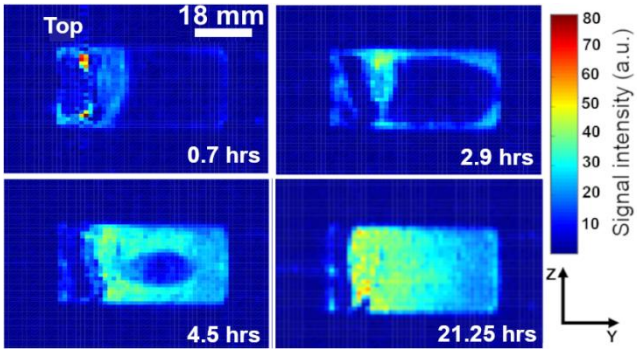

Fig. 2: 2D slices obtained from 3D π-EPI images of ^{1}H content in the hydrate system at time 0.7, 2.9, 4.5 and 21.2 hours of dissociation.

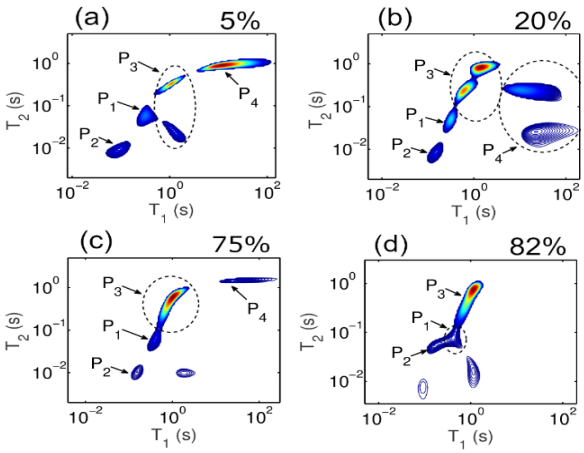

Fig. 3: Bulk T_1-T_2 of the hydrate-bearing sand pack as a function of time during hydrate dissociation. Recovered water saturation is reported at top right: (a) 0.2 hours (b) 2.4 hours, (c) 5 hours and (d) 21.9 hours. Peak P_1 is 290-psi bulk gas in the gas head, P_2 is 290-psi gas in the pore space, P_3 is bulk-like water and water in the pore space, while P_4 is capillary-trapped residual gas saturation.

Conclusions: 1D dhk SPRITE profiles showed that the initial hydrate formation was inhomogeneous in the longitudinal direction. MRI measurements showed that dissociation occurred in a core shrinking pattern, with pronounced water migration toward the low-pressure surface. Bulk T_1-T_2 measurements discriminated different molecular species and fluid environments. Bulk T_1-T_2 results show that the majority of gas is temporarily confined as capillary trapped gas upon dissociation.

References: [1] Shakerian, J. Magn. Reson. (2018). [2] Shakerian, Int. Symp. SCA (2017).

The Clinical Application of Diffusion-Weighted Image for Differentiating Myeloma From Bone Metastasis in the Extremities

Seul Ki Lee
Department of Radiology, St. Vincent's Hospital, College of Medicine, The Catholic University of Korea, Republic of Korea

Introduction

Myeloma and metastatic bone tumor of the extremities are common malignant bone marrow lesions which may be difficult to differentiate because of similar imaging findings. The purpose of this study was to evaluate diffusion-weighted image (DWI) of bone marrow in the differentiation of myeloma and bone metastasis in extremities.

Methods

10 patients with myeloma (mean age, 63.2 years; 3 men and 7 women) and 21 patients with bone metastasis (mean age, 60.2 years; 11 men and 10 women) underwent 3T magnetic resonance imaging (MRI) of the extremity with DWI (b = 50, 800, 1400 s/mm^2) were enrolled. Two apparent diffusion coefficient (ADC) maps were created using different b value combinations. In the first and second ADC maps, the b value 50 s/mm^2 was combined with b = 800 s/mm^2 (ADC_{800}) and b = 1400 s/mm^2 (ADC_{1400}), respectively. The ADC values of bone marrow in myelomatous and metastatic involvement were measured using region of interest (ROI) drawn as large as possible on picture archiving and communication system (PACS). The regions of hemorrhage, necrosis, or cystic change were excluded, comparing conventional MRI side by side. For each ADC map, a mean ADC value and a standard deviation (SD) were recorded. Comparison of the ADC values was performed by the Mann-Whitney U test. The receiver operating characteristic (ROC) curve with areas under the curve (AUC) was used to obtain the cut off values and to evaluate the diagnostic performance of DWI. $P < 0.05$ was considered as significant.

Results and Discussion

ADC_{800} and ADC_{1400} of myeloma were significantly lower than those of bone metastasis: 857 μm^2/sec vs. 1128 μm^2/sec (P = 0.003); 750 μm^2/sec vs. 1045 μm^2/sec (P = 0.002), respectively. Although the SD_{800} was not different between myeloma and bone metastasis: 199 vs. 280 (P = 0.065), the SD_{1400} of myeloma was significantly lower than that of bone metastasis: 155 vs. 241 (P = 0.023). A ROC curve was constructed for all parameters and the ADC_{1400} (AUC = 0.875, P < 0.001) had the best AUC for differentiating myeloma from bone metastasis, followed by the ADC_{800} (AUC = 0.860, P < 0.001), SD_{1400} (AUC = 0.775, P = 0.016), and SD_{800} (AUC = 0.700, P = 0.025). The cutoff value for ADC_{1400} in diagnosing myeloma from bone metastasis was ≤ 784 μm^2/sec (sensitivity 90%, specificity 90%), for ADC_{800} of ≤ 930 μm^2/sec (sensitivity 90%, specificity 81%), for SD_{1400} of ≤ 165 (sensitivity 70%, specificity 80%), and for SD_{800} of ≤ 260

(sensitivity 90%, specificity 57%), respectively. Since we wanted to investigate the difference in cellularity between myeloma and bone metastasis, ADC of higher *b* value was more suited for this analysis. We also chose SD of ADC values for the analysis of the distribution of ADC values within the bone marrow lesions. Quantification of tumor ADC heterogeneity has the potential to represent the uniform and highly packed arrangement of myeloma cells within the bone marrow.

Conclusion

ADC values and SD derived from DWI of the extremity can differentiate myeloma from bone metastasis with a high sensitivity and specificity. A *b* value of 1400 s/mm^2 seems optimal for imaging bone marrow lesion.

Multi-Region Models for Predicting Features of T1-T2 Experiments

JE Maneval (1), DL Craft (1), ML Nelson (2), LW Thrane (3), SL Codd (3) and JD Seymour (4)

(1) Department of Chemical Engineering, Bucknell University, Lewisburg, PA, USA, (2) Department of Physics, Montana State University, Bozeman, MT, USA, (3) Department of Mechanical Engineering, Montana State University, Bozeman, MT, USA, (4) Department of Chemical and Biological Engineering, Montana State University, Bozeman, MT, USA

Introduction: In this study, we develop and apply a series of transport-based models that aim to describe result of T_1-T_2 measurements in multi-phase or multi-region systems. Motivation for this work is provided by the observations of anomalous rises in T_1 signals by Song, *et al*. [1]. That study also included predictions of the observed effects by random-walk simulations. Here, we use a continuum-transport model based on the Bloch-Torrey equations [2-4] for our explanations of the measurements to enhance physical insights into the problem.

Results and Discussion: Models are developed for a series of settings of increasing complexity. We first consider the use of a single-pore/single-region model to provide the basic ideas, to present the assumptions of the simulation approach, and to help guide interpretation of results. For this model, we find that the noted anomalous-rise effects cannot be predicted. However, the model does provide insights into other features of the T_1-T_2 time-domain response data and can be used to motivate the development of more sophisticated models that feature on interacting regions. We demonstrate our findings with experimental and computational results from an ion-exchange system whose surface relaxation characteristics can be controlled.

Two-pore and two-region models are developed to allow for differences in material and length-scale characteristics between two regions. The approach we use is based on a generalization of the ideas presented by Zielinski, *et al*. [5]. We find that the effects observed by Song, *et al*. can be produced by suitable choices of the parameters in these models. Specifically, the addition of inter-pore/inter-region exchange of magnetization along with contrasts in relaxation characteristics between regions are essential for predicting anomalous signal increases. We demonstrate our findings by applying the models to systems in which exchange of magnetization between two domains is important (*e.g*., the hydrate-formation studies of Thrane, *et al*., [6]).

Conclusions: All models provide direct evidence for two important features of the T_1-T_2 relaxation spectrum. The first is the existence of modes associated with (observed) T_2 values that are greater than their corresponding (observed) T_1 values. Such modes are commonly predicted by the models presented here. Hence, such modes should be expected in the results of this type of measurement. The second feature is the importance of strong, negative-amplitude modes which are essential to the formation of the anomalous signal increases. Both of these features present challenges to the development of inverse Laplace Transform codes [7] but are found to be essential features of measurements in multiphase systems.

References: [1] Song, et al., *Phys. Rev. Letters*, **113**(2014), 235503. [2] Torrey, *Phys. Rev.* **104**(1956), 563. [3] Brownstein and Tarr, *Phys. Rev A* **19**(1979), 2446. [4] Belton and Hills, *Mol. Phys*., **61**(1987), 999. [5] Zielinski, et al. *J. Chem. Phys*., **117**(2002), 5361. [6] Thrane, et al., *J. Mag. Res*., **303**(2019), 7. [7] Chandrasekera and Mitchell, *Phys. Rev. E*, **98**(2018), 043308.

Improved one-dimensional and two-dimensional permeability NMR models

L. Wang, L. Z. Xiao*, Y. Zhang, G. Z. Liao, L. L. Wang, W. Z. Yue

State Key Laboratory of Petroleum Resource and Prospecting, China University of Petroleum, Beijing 102249, China

The permeability of the reservoir or porous media can be obtained through NMR measurements. The most commonly used models are SDR model and Coates model. The Coates model is considered more accurate in evaluating permeability of porous media with multiphase fluid [1]. Therefore, the analysis of the physical meaning of the empirical coefficient C in Coates model is particularly important. The main pore structure of shale and tight-sand in unconventional reservoirs is Nano pores [2]. The proportion of heavy oil in crude oil is 70%, of which 30%-40% are polymer components. Therefore, the migration of macromolecule in nano pore channels is the key problem in enhancing oil recovery of shale oil. Herein, we using mesoporous materials filled with macromolecules as samples, extraction experiments were carried out with petroleum ether and ethanol. Combined with corresponding NMR experiments Fig1, Fig2, one-dimensional and two-dimensional NMR permeability models were proposed respectively.

Compared with Coates model, the proposed one-dimensional NMR permeability model introduce the tortuosity, film thickness, and pore throat ratio Eq(1). These parameters make the calibration coefficient C in Coates model have practical physical significance. The permeability obtained by this model is basically consistent with mercury intrusion permeability and Darcy flow permeability.

$$k = \frac{\varphi d^2}{2\tau^2}\left(\frac{BVM}{BVI}\right)^2 \left\{ \frac{27}{20} \cdot \frac{\left(1+\frac{r_t}{r_b}\right)^2\left[1+\frac{r_t}{r_b}+\left(\frac{r_t}{r_b}\right)^2+\left(\frac{r_t}{r_b}\right)^3+\left(\frac{r_t}{r_b}\right)^4\right]}{\left[1+\frac{r_t}{r_b}+\left(\frac{r_t}{r_b}\right)^2\right]^3} \right\} \quad (1)$$

Moreover, we carried out T_1-T_2 and D-T_2 experiments on the samples. The results show that low filed NMR T_1-T_2 can clearly determine the interface effect in mesoporous material. If the film thickness and BVI (bound fluid volume),BVM (free fluid volume) parameters of the measured can not be determined, we give another permeability prediction model of NMR by D-T_2 spectrum Eq(2). The results of two-dimensional permeability model and one-dimensional permeability model are basically the same.

$$k = \frac{\varphi}{2\tau^2}\left(\rho T_{2lm}\right)^2 \left\{ \frac{27}{20} \times \frac{\left(1+\frac{r_t}{r_b}\right)^2\left[1+\frac{r_t}{r_b}+\left(\frac{r_t}{r_b}\right)^2+\left(\frac{r_t}{r_b}\right)^3+\left(\frac{r_t}{r_b}\right)^4\right]}{\left[1+\frac{r_t}{r_b}+\left(\frac{r_t}{r_b}\right)^2\right]^3} \right\} \quad (2)$$

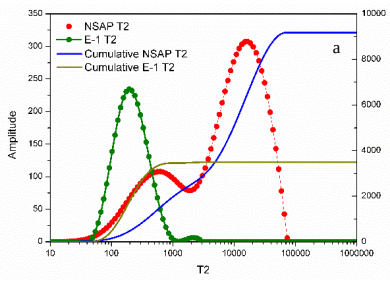

Fig 1 T_2 and T_2 cumulative spectrum

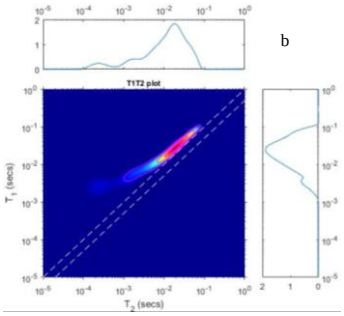

Fig 2 Mesoporous samples T_1-T_2

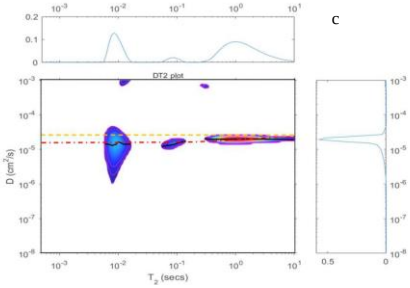

Fig 3 Mesoporous samples D-T_2

References

[1] Richard Sigal. Petrophysics, 2002, 43, 38.
[2] R.M. Slatt, N.R. Obrien, AAPG Bulletin, 2011, 95(12): 2017-2030.

Good statistics from noisy multidimensional distributions

A. Reymbaut[a], P. Mezzani[a,b], J. P. de Almeida Martins[a], D. Topgaard[a]
[a]Lund University, Sweden, [b]Università degli Studi di Milano, Italy

Introduction: Most investigated samples are heterogeneous over the spatial resolution of diffusion NMR/MRI measurements. Consequently, the measured diffusion signal writes as a Laplace transform of the 4D diffusion tensor distribution $P(D_{iso},D_{\Delta},\theta,\phi)$, with isotropic diffusivity D_{iso}, diffusion anisotropy D_{Δ}, and spherical angles θ and ϕ. Inverting this Laplace transform is essential for retrieving a given sample's microstructure. However, it is known to be a very ill-conditioned problem.

Methods: We compare *in silico* four inversion methods in terms of accuracy and precision: the Gamma distribution fitting of powder-averaged signals (Gamma) [1], the unregularized free inversion of powdered-averaged signals (Free2D) [2], the covariance tensor fitting (Cov) [3], and the full unregularized free inversion (Free4D) [4]. The data was obtained *via* a typical $10\times b$=100, $10\times b$=700, $15\times b$=1400, $20\times b$=2000 (s/mm^2) acquisition for both linear and spherical diffusion encodings on a powder of 100 identical sticks ($D_{\parallel}$ = 3 µm^2/ms, $D_{\parallel}=D_{\perp}/100$), and on a single stick with the same diffusional features. Noise was added to reach a signal-to-noise ratio (SNR) of 40.

Results and discussion: Fig. 1 presents the aforementioned comparison with boxplots of the mean isotropic diffusivity $\mathrm{E}[D_{iso}]$, mean anisotropy $\mathrm{E}[D^2_{aniso}] = \mathrm{E}[D^2_{iso}D^2_{\Delta}]$ and variance of isotropic diffusivities $\mathrm{V}[D_{iso}]$ ($\mathrm{E}[\cdot]$ and $\mathrm{V}[\cdot]$ denote the macroscopic average and variance), over 100 realizations of each method. In the single stick case, Cov and Free4D are the only methods showing consistently high accuracies and precisions. In the stick powder case, the inversion methods share comparable precisions, but only Free2D and Free4D show consistently high accuracies. While Free2D and Free4D are rather CPU time-consuming, Gamma and Cov's systematic errors arise from applying these approximations to *b*-values that are beyond their ranges of validity.

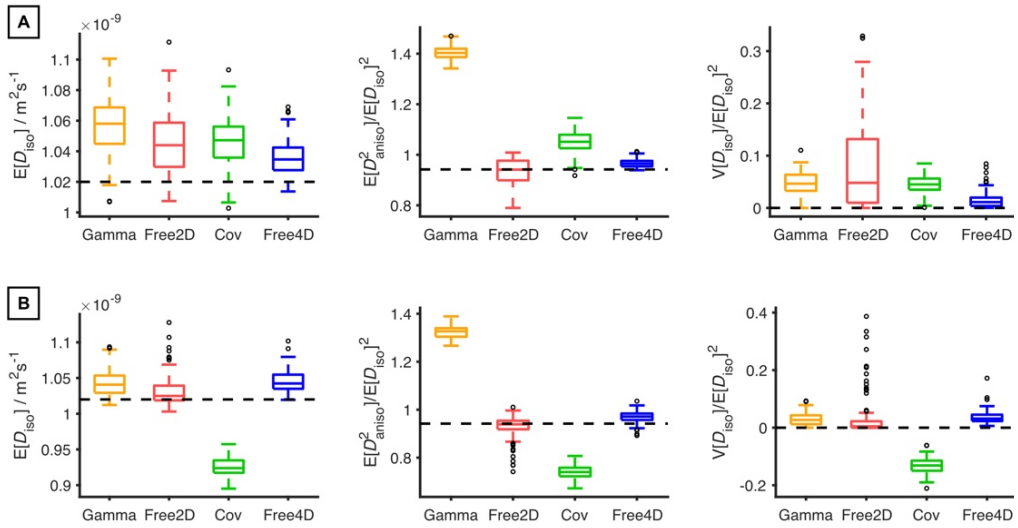

Fig. 1: Boxplots comparing 100 realizations of the Gamma, Free2D, Cov and Free4D inversion methods for a single stick (A) and a stick powder (B). Displayed metrics are the mean isotropic diffusivity (left), the normalized mean anisotropy (center) and the normalized isotropic variance (right). Dashed horizontal lines: ground truth.

Conclusion: The full unregularized free inversion (Free4D) is the most consistent method in terms of accuracy and precision when estimated on diffusion populations exhibiting either macroscopic or microscopic diffusion anisotropy. Further tests will be conducted in order to assess the effect of isotropic heterogeneity and SNR on the above methods.

References: [1] S. Lasič *et al.*, Front. Physics (2014) [2] J. P. de Almeida Martins *et al.*, Phys. Rev. Lett. (2016) [3] C.-F. Westin *et al.*, Neuroimage (2016) [4] D. Topgaard, NMR Biomed. (2019).

Benchtop NMR spectroscopy and diffusion measurements to characterize enzymatic hydrolysis online and at line

E.R. McCarney[a], *R. Dykstra*[b], *and K. E. Washburn*[c]
[a]Korimako Chemical Ltd., Wellington, New Zealand, [b]Victoria University Wellington, Wellington, New Zealand, [c]Nofima AS, Tromsø, Norway

Introduction. Benchtop NMR spectroscopy is still finding its footing in industrial applications. NMR spectroscopy in general has much to offer in regards to process and quality control. Unfortunately, high-field NMR instrumentation is often uneconomical or not suitable for the location where it is needed. Benchtop NMR can solve these two issues, but forces a compromise on performance, such as sensitivity and chemical shift dispersion. Often, these issues are tolerable or can be overcome with advanced acquisition or processing methods. One promising application is monitoring of enzymatic hydrolysis, which is seeing increased usage to create high value materials from traditionally low value by-products. Hydrolysis breaks down tissue through enzymatic hydrolysis of peptide bonds releasing peptides, amino acids, oils, and metabolites. Development of this processing method is hampered by a lack of tools to characterize the reaction in real time. Current analysis methods rely on taking offline samples, deactivating the enzymes, and performing analysis on the products after the reaction has already run its course. Nuclear magnetic resonance benchtop spectroscopy and diffusion ordered spectroscopy (DOSY) were investigated as methods for online and at-line process monitoring of enzymatic hydrolysis.

Methods. NMR measurements were performed to monitor the enzymatic hydrolysis reactions on red cod, salmon, and shrimp. The raw material was homogenized and then digested with a peptidase cocktail. The reaction was performed in a beaker and pumped through a benchtop NMR spectrometer, where proton NMR spectra were recorded. Samples were also collected in parallel for offline measurement comparisons. Diffusion measurements were measured at line by transferring a sample to an NMR tube and immediately collecting DOSY spectra without deactivating the enzymes.

Results and discussion. Both the online and offline measurements were able to follow the reaction process. Offline measurements offer the benefit of a suite of established methods to characterize the reaction, however, they showed faster reaction rates than the online measurements that suggested that the enzymatic hydrolysis process continued for a period of time during the deactivation period. At-line diffusion measurements were capable of estimating mean peptide size that directly relates to the degree of hydrolysis, at a reduced temporal resolution compared to one-dimensional proton spectra.

Conclusions. Online monitoring provides a more accurate description of the reaction progression than offline methods. Diffusion measurements are also able to characterize the average molecular size throughout the reaction as a key indicator of the hydrolysis progression. Application of these methodologies to several types of raw materials indicates the technique is robust.

Probing surface-to-volume ratio in anisotropic media

N.Moutal[1], *I. I. Maximov*[2], *D. S. Grebenkov*[1]
[1]PMC, Ecole Polytechnique, CNRS, IP Paris, Palaiseau, F-91128 France
[2]Norwegian Centre for Mental Disorders Research, and University of Oslo, Oslo, Norway

Introduction: We propose a new approach for estimating surface-to-volume ratio of anisotropic media. It is based on our generalization of Mitra's formula [1] to any gradient profile and pore shape. We show that the original formula may lead to significant errors in the estimated surface-to-volume ratio. We correct for these errors and introduce a new "isotropy" criterion ensure that the diffusion weighted sequence is insensitive to the mesoscopic anisotropy of the medium. We implement a simple numerical algorithm to design optimal "isotropic" gradient sequences with required properties.

Methods: We consider an arbitrary gradient profile **g**(t) from t=0 to t=T (echo time), with the refocusing condition: $\int_0^T \boldsymbol{g}(t)dt = \mathbf{0}$. We denote by D_0 the intrinsic diffusion coefficient of the spin-bearing particles. Using mathematical techniques detailed in [2], we derived the short-time asymptotic behavior of the apparent diffusion coefficient probed by diffusion MRI [3].

Results and discussion: Our formula generalizes the Mitra's one via the factor η:

$$D(T) = D_0\left(1 - \eta\frac{4}{3\sqrt{\pi}}\frac{S}{V}\sqrt{D_0 T} + O(T)\right), \quad \text{Eq. 1}$$

$$\eta = Tr\left(S^{(3)}T^{(3)}\right), \quad \text{Eq. 2}$$

where the 3x3 ``structural'' matrix $S^{(3)}$ describes the pore shape and the 3x3 ``temporal'' matrix $T^{(3)}$ describes the gradient profile. An accurate estimation of S/V from the measured $D(T)$ requires thus the knowledge of the factor η (which was set to $\eta = 1/3$ in Mitra's formula).

Even for the simplest case of a spherical pore and a linear gradient encoding, η strongly depends on the gradient waveform, varying from 0 to 1/3. In general, applying the classical Mitra formula without the correct value of η may lead to significant underestimating of S/V.

In anisotropic media, the estimated S/V generally depends on the orientation of the scanner with respect to the sample and on the pore shape. It follows from Eq. 2 that this dependence is removed if the gradient sequence satisfies the "isotropy" condition when $T^{(3)} \propto I$. This advantage of the new "isotropic" sequence is demonstrated in Fig. 1.

Conclusion: The generalization (1) of Mitra's formula is expected to have a great interest for clinical applications where a precise determination of surface-to-volume ratio and pore anisotropy is required.

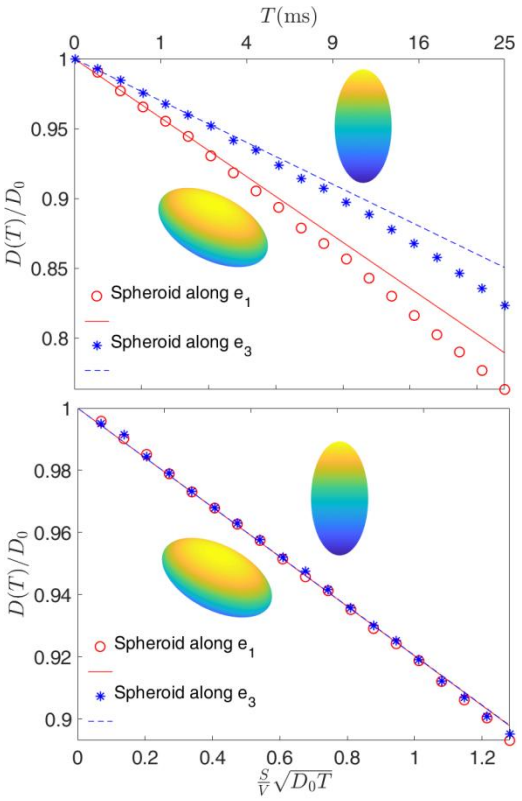

Fig. 1: Effective diffusion coefficient inside a spheroid with semi-axes 10μm and 5μm and intrinsic diffusion coefficient $D_0 = 1\,\mu m^2/ms$. Results from Monte Carlo simulations are shown by symbols and the generalized Mitra formula (1) is plotted as line. (Top) q-MAS sequence [4]: different orientations produce different D(T) curves. (Bottom) Optimized sequence with isotropic $T^{(3)}$: the D(T) curves coincide and have a much longer range of validity.

References: [1] P. P. Mitra, P. N. Sen, L. M. Schwartz, and P. Le Doussal, Phys. Rev. Lett. **68** 3555-3558 (1992)
[2] D. S. Grebenkov, Rev. Mod. Phys. **79** 1077-1137 (2007)
[3] N. Moutal, I. I. Maximov, and D. S. Grebenkov, IEEE TMI (in press) DOI: 10.1109/TMI.2019.2902957
[4] S. Eriksson, S. Lasič, and D. Topgaard, J. Magn. Reson. **226** 13-18 (2013)

Quantifying the mitochondrial content with diffusion MRI

N. Moutal[1], *D. S. Grebenkov*[1], *S. Clerjon*[2], *G. Pages*[2], *and J.-M. Bonny*[2]
[1] PMC, Ecole Polytechnique, CNRS, IP Paris, F-91128 Palaiseau France
[2] AgroResonance - UR370 QuaPA, F-63122 Saint Genès Champanelle, France

Introduction: In this work, we show how diffusion MRI protocols with high b-values may be applied to a non-invasive quantification of mitochondria and other microscopic organelles. While mitochondria play a major biochemical role and are related to several diseases, their current studies require invasive microscopy techniques such as TEM. Therefore, solving this challenging problem with diffusion MRI would be of great clinical interest.

Methods: The microscopy experiments were conducted at 9.4T *ex vivo* on pork muscle at a temperature of 16°C. We applied a PGSE sequence with δ=3.2ms, Δ=10ms, and b-values up to 10000s/mm^2, for 6 non-collinear gradient directions and 32x32 (0.3mm)^3 voxels. Additionally, a fat suppression scheme [1] was employed to reduce the contribution from lipids. Two contrasted muscle samples were analyzed: Masseter (M1), an oxidative muscle with high mitochondrial content, and Longissimus Dorsi (LD2), a glycolytic muscle with low mitochondrial content.

Results and discussion: For both samples, the signal shows a fast decay at low b-values and a slow decay at high b-values (see Fig.1). The slow-decaying signal is attributed to water trapped inside mitochondria. A bi-exponential fit is applied:

$$S = S_0\left[(1-\rho)\exp\left(-b\sum_{i,j} e_i\, D^f_{i,j}\, e_j\right) + \rho\exp(-bD^s)\right] \quad \text{(Eq.1)}$$

where S_0 is the reference signal (at b=0), ρ is the mitochondrial water fraction, D^f is the apparent diffusion tensor of "fast" water inside muscle cells and D^s is the apparent diffusion coefficient of "slow" water inside mitochondria.

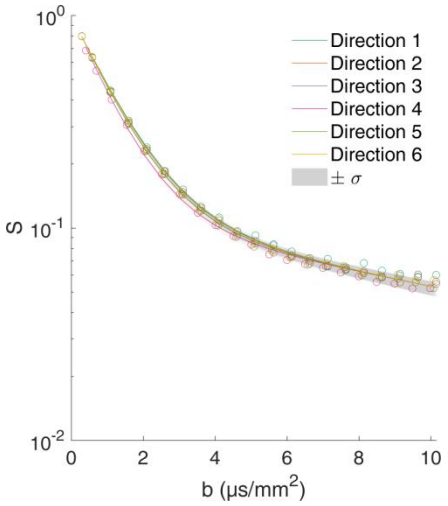

Fig.1 Signal from one voxel of sample M1 and different gradient directions (circles) and fit by Eq. 1 (lines). At high b-values, one observes a slow-decaying residual signal. The noise level is around 0.003.

As mitochondria are filled with around 64% of water [2], one can infer the mitochondrial volume fraction (MVF) from ρ as MVF ≈ 1.5ρ. Figure 2 shows the map of MVF for both samples. Sample M1 displays two regions with respectively high (~15%) and low (~5%) MVF whereas sample LD2 has a uniform low (~3%) MVF. These results are in qualitative agreement with the muscle type as discussed above, and the values of MVF are consistent with the literature (see [3] for a comparison with mouse and dolphin). Histological slices are planned in order to confirm and explain the existence of two different regions in sample M1.

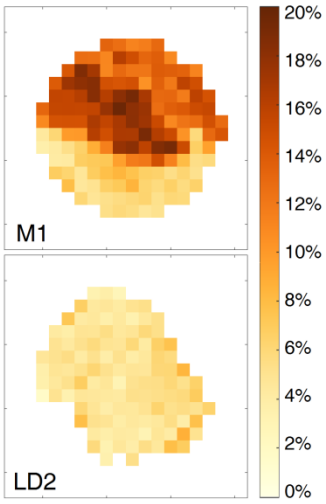

Fig.2 Estimated mitochondria volume fraction (MVF) for both samples.

Conclusion: The residual signal at high b-values in muscles is naturally explained by mitochondria. This work is a proof of concept and a prerequisite for developing *in vivo* methods to quantify the content of various organelles in muscle, e.g. for studying mitochondrial dysfunction in aging.

References: [1] J. M. Gomori et al., Radiology 168, 493-495 (1988).
[2] M. L. Williams, Biochim. Biophys. Acta 118, 221-229 (1966).
[3] B. Pathi et al., J. Exp. Biol. 215 (11), 1871-1883 (2012).

Title: Method improvements for diffusion tensor imaging of turbulent fluids

Authors: Amy-Rae Gauthier, Noah Stocek, and Ben Newling

Abstract:

The study of anisotropic turbulence is of great interest to the fluid dynamics community; however, measurements of turbulent systems present many challenges. It has been shown that turbulent fluctuations can be modelled using a diffusion equation, and therefore diffusion tensor imaging (DTI) can be used to measure the anisotropy of those fluctuations. Since the system is fast-moving (>10 m/s) the Single Point Ramped Imaging with T1 Enhancement (SPRITE) pulse sequence with bipolar motion-sensitizing gradients is used to generate a diffusion weighted image (DWI). Six different motion-sensitization schemes provide the six projections needed to measure the full tensor. This method has been applied to multiple systems both gas and liquid, each of which presents their own measurement challenges. This poster will present improvements made to this DTI experiment as well as the results of those improvements.

How MRI can assist Rheology?

M.Ferrari[1], *M. Jenny*[1], *S. Kiesgen De Richter*[1], *S. Leclerc*[1], *C. Métivier*[1], *X. Zhang*[2], *P. Coussot*[2]
[1]LEMTA, Univ. de Lorraine, Nancy, France, [2]Navier, Univ. Paris Est Champs sur Marne, France.

Rheology is the study of the flow of matter in response to an applied force. The studied fluids are often complex and the standard macroscopic rheology analysis is not sufficient to understand certain phenomena associated with flow or material heterogeneities. A "local" rheology analysis is then crucial. In addition, the MRI technique is a convenient solution especially when the fluid is opaque. Here are three examples of MRI/Rheology applications that we are developing in the laboratory:

Thixotropic suspension: The study of non-Brownian fiber suspension rheometry in a Taylor-Couette device is done thanks to the velocity profiles obtained by MRI measurements (Bruker spectrometer at 14.1 T equipped with a Rheo-NMR system) [1]. The local rheological data are acquired for different shear rates and volumetric factions. At low angular velocities, MRI-derived velocity profiles highlight the localized flow. This observation confirms the viscoplastic fluid behavior previously identified with the rheometer. The position of the fluid/solid interface depends on the volume fraction and shear rate. Near the jamming transition, the local rheology shows also constant and discontinuous shear thickening. The study of these suspensions shows an irreversible behavior. Since the fibres are non-Brownian, their position and orientation require a mechanical action to be modified. The orientation and/or migration of the fibres are therefore very important parameters influencing the rheology of these suspensions.

Temperature and velocity measurements: The study of thermal transfer by conduction and convection represents a wide field of industrial and environmental applications. We investigate the possibility to measure temperature profiles with MRI in a fluid layer submitted to heat transfer [2]. By imposing a vertical temperature gradient, we study the temperature fields in both conductive and convective regimes. The temperature fields are obtained by measuring the transverse relaxation time T2 in glycerol, a Newtonian fluid. We show that for a conductive regime, temperature measurements are in very good agreement with the theoretical profile. In the convective regime, when comparing the temperature and velocity fields obtained by MRI (Bruker Avance Biospec 2.4T), we get an excellent agreement in terms of flow structure. Temperature uncertainties are found to be less than 1 ◦C for all our results.

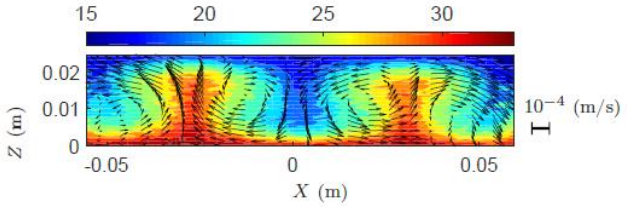

Fig. 1: Superimposition of the velocity vectors on the temperature field for _T = 13.7, Ra = 7795

Wall slip mechanism: We carried out a series of experiments with the aim of completing our knowledge of wall slip characteristics [3]. A part of the study is based on internal measurements of the velocity profile in a capillary obtained by MRI with a Bruker spectrometer at 14.1 T. A flow rate-controlled syringe injects the inverse emulsion into glass capillaries of different diameters (0.6 to 2 mm). We observe a linear variation of the velocity with the stress, but at the approach of the yield stress value the velocity increases steeper, apparently more like a quadratic law. This suggests a change of both regime and physical process for wall slip when the yield stress fluid is in its liquid regime along the wall.

References: [1] Jenny, Ferrari, Gaudel, Kiesgen de Richter, EPL (2018). [2] Leclerc, Métivier, Exp. Fluids (2018). [3] Zhang, Lorenceau, Bourouina, Basset, Oerther, Ferrari, Rouyer, Goyon, Coussot, J. Rheo. (2018).

Flow imaging in a model fractured porous media at low magnetic field

M. Fleury, N. Gland

IFP Energies nouvelles, 92852 Rueil-Malmaison, France

Imaging of flow in fractured porous media and the quantification of fracture-matrix mass exchange is a general issue in many applications: Enhanced Oil Recovery, CO_2 storage, aquifer contaminants etc. We studied the flow and mass exchange in a model fractured porous media consisting of two half cylinders of a carbonated porous media separated by a thin spacer 300 µm thick (Figure 1). This system is placed in a cell fitting into the MRI system.

The MRI system is a proton 20 MHz vertical permanent magnet system (Oxford Instrument) equipped with a 30mm 3D imaging probe in which we programmed various imaging sequences: beside 1D standard longitudinal density profiles [1] a 13-interval velocity imaging sequence [2], 2D spin-echo density imaging as well as multi-slice fast spin-echo (FSE) used in medical imaging. The 2D images produced have a resolution of 320x320µm with a slice thickness of 4 to 8 mm. The home-made flow cell allows the injection of different fluids under moderate pressure (confining pressure up to 80 bar) and at a temperature of about 30°C (magnet temperature). This cell is entirely made of a specific poly-ether-ketone (PEEK) together with a special confining elastomer sleeve producing residual proton signals in a relaxation time range below 1 ms. With an outer diameter of 30 mm, it can accommodate samples of diameter 20 mm in diameter, and up to 50 mm in length.

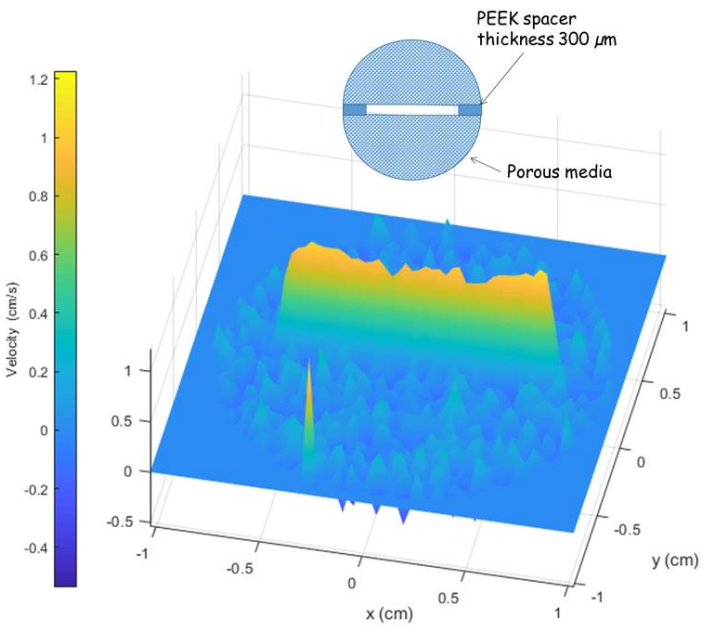

Figure 1: Schematic of the model fractured porous media, diameter 20 mm and length 40 mm (above) and, 2D quantitative velocity flow imaging through the fracture (below).

We studied specifically the injection of a foam through the fracture and the possibility to displace hydrocarbons trapped in the matrix by capillary effects. In this gas-water-oil 3 phase system, we combined imaging and T_2 relaxation time distribution data to quantify the amount of fluids present in the matrix. Water properly doped with paramagnetic solutions is not detected in the images but only in the T_2 distribution to confirm quantitative aspects of 2D images.

Despite the relatively lower sensitivity of the MRI system used compared to classical 200MHz systems, it is well suited to study axisymmetric flows in porous media with reasonable image acquisition times.

References

[1] G. Batôt, M. Fleury, L. Nabzar, Reducing CO2 Flow Using Foams, Energy Procedia 114 (2017) 4129–4139. https://doi.org/10.1016/j.egypro.2017.03.1553.

[2] N. Spindler, P. Galvosas, A. Pohlmeier, H. Vereecken, NMR velocimetry with 13-interval stimulated echo multi-slice imaging in natural porous media under low flow rates, J. Magn. Reson. 212 (1) (2011) 216–223. https://doi.org/10.1016/j.jmr.2011.07.004.

MRI flow cell development to monitor in-situ and in-real time dissolution of porous food products

Gert-Jan Goudappel, Theo Blijdenstein, Adrian Voda
Unilever,Vlaardingen, The Netherlands

Many food products and ingredients are stored in dry form until meal preparation. Consumer appreciation of such products is for a major part determined by their dissolution behaviour. Macroscopic assessment of dissolution behaviour provides only limited insight in mechanisms by which water enters porous food materials.

For this purpose, an experimental MRI flow cell setup was designed and implemented on a Bruker 300 MHz NMR wide bore system for non-invasive µ-imaging of water ingress and dissolution. Measurements can be performed in-real time and in-situ under consumer relevant convection and temperature (ambient to 95 °C) conditions. Convection of water was achieved by continuous flow from a water reservoir of 5 litres with adjustable flow rate.

Water ingress profiles were obtained using a Flash sequence and acquired as a 2D sample slice with a minimum achieved time resolution (including I/O handling) of 8 seconds. Water mobility (T2) maps were recorded in stop-flow conditions on a time average of 2 - 4 minutes.
The data were processed with home-written Matlab codes, which allowed for fast import, image intensity normalisation, background correction, rotation and ROI selection.

The ingress profiles allowed to study the effect of porosity and swelling on water diffusion regimes in a wide range of food products. Examples will be provided of composite savoury products where porosity and presence of swelling ingredient can have a pronounced impact on water ingress and ultimately dissolution behaviour.

New spatial encoding strategy for systems with ultra-short transverse relaxation times

V. Sarou-Kanian[1], *M. Yon*[1], *D. Massiot*[1], *M. Deschamps*[1], *E. Salager*[1], *F. Fayon*[1]
[1]CNRS, CEMHTI UPR3079, Univ. Orléans, F-45071 Orléans, France.

Introduction: Magnetic resonance imaging (MRI) and self-diffusion coefficient measurements are amongst the main applications of NMR. Both rely on spatial encoding using pulsed magnetic field gradients (PFG). Practically, PFG are applied during hundreds of microseconds (µs) up to several milliseconds (ms). However, when high gradient strengths (>1000 G/cm) are required the gradient rise time may also reach hundreds of µs and limit the shortest spatial encoding time.
In most MRI or diffusion sequences, the signal acquisition occurs after an echo delay (gradient, spin or stimulated), which usually lasts for more than a millisecond. In the majority of liquids or media with high mobility, this instrumental limit is irrelevant as their transverse relaxation times (T_2, T_2*) are much longer than the spatial encoding time. Nevertheless, this is no longer the case for solids, paramagnetic liquids, or porous media, for which these standard methodologies are inefficient. To address the issue of PFG rise time in MRI or diffusion measurements for spin systems with ultra-short T_2* or T_2 (<< 1 ms), we propose a new strategy based on an ultrafast spatial encoding using overlapping frequency swept pulses applied in conjunction with strong pulsed field gradients.

Methods:

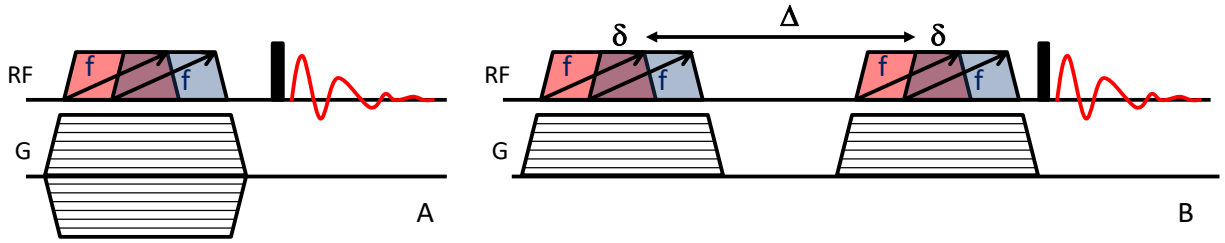

Fig. 1: Chemical shift imaging (A) and diffusion with stimulated echo sequence (B) using the ultrafast spatial encoding scheme.

Results:

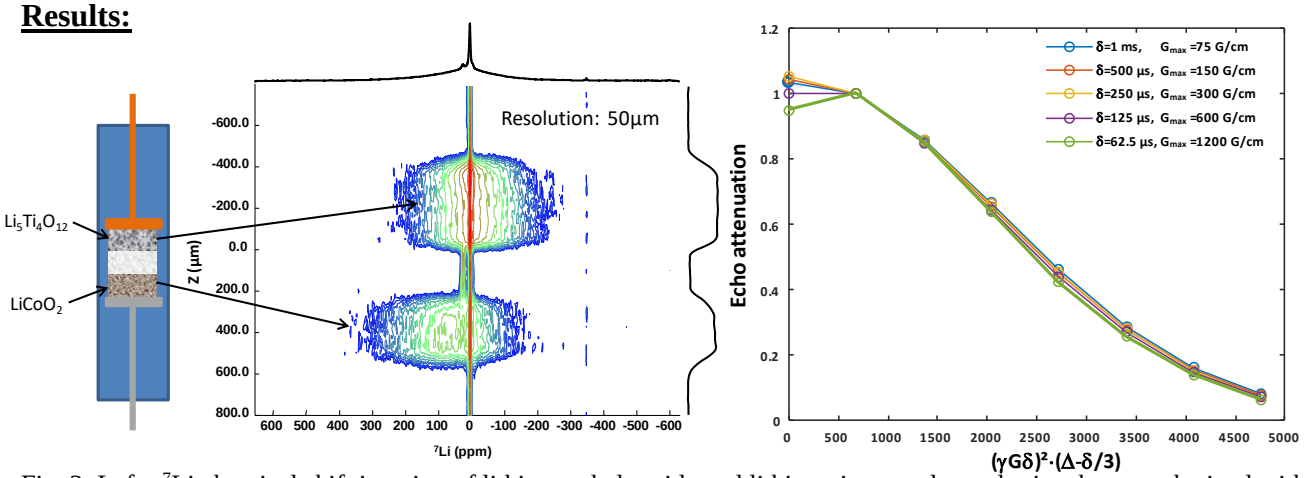

Fig. 2: Left : ^{7}Li chemical shift imaging of lithium cobalt oxide and lithium titanate electrodes in a battery obtained with the sequence in Fig. 1A. Right: Echo attenuation curves of water from a diffusion STE sequence (Fig. 1B) with different δ (1ms → 62.5 µs). The maximum gradient strength is calculated to keep the factor $\gamma^2G^2\delta^2\cdot(\Delta-\delta/3)$ constant. Δ=47.5 ms.

Conclusion: The combination of very strong pulsed field gradients (>1000 G/cm) and overlapping frequency swept pulses enables ultra-short spatial encoding times (<< 1ms). It is implemented for MRI as well as for diffusion experiments. This development paves the way for the investigation of numerous systems with ultra-short T_2.

3D Imaging of flow pattern in soil – plant systems

S. Haber-Pohlmeier[1], J. Wang[2], A. Pohlmeier[3], P. Galvosas[2]

[1]RWTH Aachen University, ITMC, Aachen, Germany, [2]MacDiarmid Institute for Advanced Materials and Nanotechnology, School of Chemical and Physical Sciences, Victoria University Wellington, New Zealand, [3]Research Center Jülich, IBG-3, Jülich, Germany.

Introduction: Understanding root water uptake is indispensable for the optimization of plant growth and crop yield against the background of growing world population. One strategy to understand how root water uptake functions is the knowledge of water flow from bulk soil to the root. In contrast to direct flow imaging of fluxes in above-ground plant parts [1], little is known about flow patterns and velocities in the soil-root compartment. This is due to the low flow velocities in the range of some tens of µm/s. In this work, we extend the mapping of velocities in this range with the help of a step-by-step approach: Firstly, by using a phantom with heterogeneous flow and secondly, by using a live plant under steady state illumination in a scanner. To profit from sufficient signal to noise and rapid multi-slice acquisition in interleaved mode we used the 13 interval STEMSI [2] with incorporated Stimulated Echo Acquisition Mode (STEAM) [3].

Methods: The flow phantom consisted of a sink immersed in saturated sand under stationary total flow velocity conditions, regulated by constant external pressure difference. *Q*-space imaging was performed in multi-slice mode using 2 to 8 *q*-steps, allowing the calculation of velocity vectors as well as spatially resolved propagators. For imaging flow velocities in a real soil plant system we investigated a broad bean in sand under constant illumination and water supply from the bottom. Plant growth requires pure tap water without T_1 accelerating agents such as Cu^{2+} so that long T_1 relaxation must be compensated for by multi-slice mode with interleaved slice selective excitation. The number of *q*-steps was identical to the measurements of the flow phantom. In addition to velocity imaging the root system architecture was scanned using a T_2-weighted RARE sequence.

Results and Discussion: For the flow phantom we could identify three flow regimes from homogeneous plug flow in sufficient distance above the suction cup to convergent flow patterns directed towards the sink and a parabolic flow velocity profile in the capillary. In contrast to [2] distinct transverse components occurred directing the flow into the sink and 3D flow velocity vectors were calculated (Fig. 1). The validity of the measured data is confirmed by comparing MRI-derived and applied flow velocities. For the first time, we were able to observe flow velocities of down to 10 µm/s with the modified STEMSI sequence. Thus, the expected magnitude of flow rates due to natural transpiration is now achievable in a period of time in which plant growth did not affect the shape of the root system and the water uptake patterns. We obtained spatially resolved maps of the propagator from a set of four or eight *q*-steps to visualize the relative contributions of diffusion and flow. Due to the low transpiration rate of 5 cm^3 /day, the flow velocities inside lateral roots did not exceed the range of 10 µm/s and could be followed along the root system.

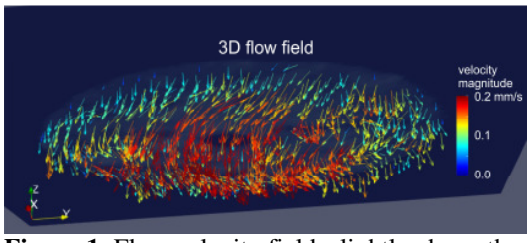

Figure 1: Flow velocity field, slightly above the suction cup with transverse components.

Conclusion:
The modification of the STEMSI sequence allows reliable imaging of low flow velocities and diffusion in the multi-slice interleaved mode. This enables one to acquire and study the spatially resolved patterns of water uptake in selected plant root systems and potentially to optimize irrigation strategies.

References: [1] Van As, Encycl. Magn. Res. (2012).[2] Spindler et al, J. Magn. Res. **212**, 216-223 (2011). [3] Frahm, et al., J. Magn. Res. **64**, 81-93 (1985).

MR signal for powdered specimens

Herberthson, M.[1], *Yolcu, C.*[2], *Knutsson, H.*[2], *Westin, C-F.*[2,4], *Özarslan, E.*[2,3]

[1]Dept. of Mathematics, Linköping University, Linköping, Sweden, [2]Dept. of Biomedical Engineering, Linköping University, Linköping, Sweden, [3]Center for Medical Image Science and Visualization, Linköping University, Linköping, Sweden, [4]Dept. of Radiology, Brigham and Women's Hospital, Harvard Medical School, Boston, MA, USA.

Introduction: We derived analytical expressions for an orientational average [1] that is relevant to examinations of porous media via diffusion MR as well as multidimensional solid-state NMR spectroscopy. In these disciplines, there is a nonnegative symmetric diffusion or chemical shift tensor that represents the locally anisotropic structure of the medium. The experimental parameters are captured by another such tensor. We shall denote these tensors by **D** and **B**, respectively. The MR signal for a specimen comprising randomly-oriented (powdered) ensemble of **D** tensors is given by $\bar{S} = \left\langle e^{-\mathrm{tr}(\mathbf{DRBR}^t)} \right\rangle_{\mathbf{R}} = \left\langle e^{-\mathrm{tr}(\mathbf{R}^t\mathbf{DRB})} \right\rangle_{\mathbf{R}}$; here the average is taken over all rotation matrices $\mathbf{R} \in \mathrm{SO}(3)$.

Methods: The tensors **D** and **B** are characterized by their respective eigenvalues a,b,c and d,e,f. The average is calculated by expressing a general rotation matrix **R** in terms of suitable angular coordinates, and performing the integration explicitly. When needed, expressions are expanded in power series. After integration, the sums are expressed in terms of hypergeometric functions.

Results and discussion: The average signal, $\bar{S}$, is a function of the eigenvalues a,b,c,d,e,f and is expressed in several ways as series of hypergeometric functions. As an example, for a general **D** and an axisymmetric **B** (setting $e=f$), $\bar{S}$ is given by

$$\bar{S} = e^{-f\,\mathrm{tr}(\mathbf{D})}\frac{\sqrt{\pi}e^{(f-d)c}}{2}\sum_{n=0}^{\infty}\frac{[(a-b)(d-f)]^{2n}}{16^n\left(2n+\frac{1}{2}\right)!}\binom{2n}{n}\,{}_1F_1\left(2n+1;2n+\tfrac{3}{2};\tfrac{1}{2}(f-d)(a+b-2c)\right). \quad \text{Eq. 1}$$

Here, ${}_1F_1(\alpha,\beta;x)$ is the confluent hypergeometric function with parameters α, β and argument x. Although mathematically equivalent, the numerical behaviour of such series are largely influenced by permutations of $\{a,b,c\}$ and $\{d,e,f\}$. Typically, a quickly converging series is obtained through a careful ordering of the eigenvalues.

In the Figure, we illustrate the signal decay for a rank-1 measurement tensor **B** having eigenvalues $(d,0,0)$ for six different **D**-tensors having the same trace (same slope near $d=0$), and the same minimum eigenvalue (same asymptotics). The signal decay curves for the axisymmetric **D**-tensors (dashed lines) deviate substantially from those in absence of axisymmetry (solid curves).

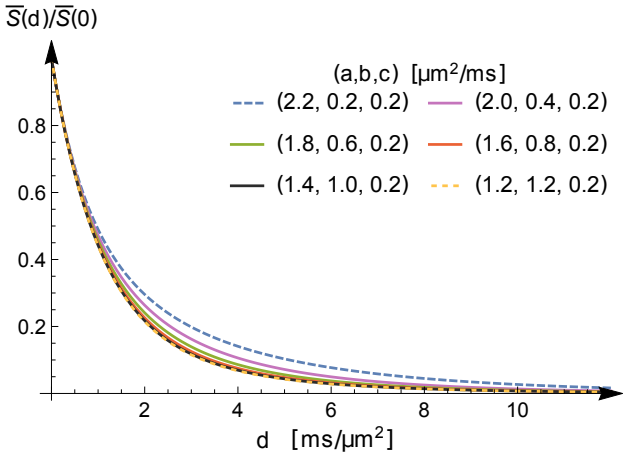

Conclusion: Our results lead to an efficient estimation of the average signal, extending the previously available expressions [2-4] to cases in which the tensors are not axisymmetric. The quantity we evaluated is the Laplace transform of a tensor distribution describing a uniform ensemble of rotated copies of a given tensor. Thus, our work extends [5] to a new type of tensor distribution.

References: 1. Herberthson, M, Yolcu, C, Knutsson, H, Westin, CF & Özarslan, E. *Sci Rep*, 9, 4899, (2019).
2. Bloembergen, N & Rowland, TJ. *Acta Metallurgica* 1, 731-746 (1953).
3. Joabsson, F, Nydén, M, Linse, P & Söderman, O. *J Phys Chem B* 101, 9710-9716 (1997).
4. Eriksson, S, Lasič, S, Nilsson, M, Westin, CF & Topgaard, D. *J Chem Phys* 142, 104201 (2015).
5. Jian, B, Vemuri, BC, Özarslan, E, Carney, PR & Mareci, TH. *NeuroImage* 37, 164-176 (2007).

Characterization of Anomalous Jet and Bubble Interaction in a Fluidized Bed

Christopher M. Boyce[1], Alexander Penn[2,3], Maxim Lehnert[3], Klaas P. Pruessmann[2], Christoph R. Müller[3]

[1]Department of Chemical Engineering, Columbia University, New York, NY, USA
[2]Institute of Biomedical Engineering, ETH Zurich and University of Zurich, Zurich, Switzerland
[3]Department of Mechanical and Process Engineering, ETH Zurich, Zurich, Switzerland

Introduction: The motion and interaction of voids, such as bubbles and jets, in fluidized beds has a strong impact on the performance of several industrial processes, yet these dynamics are not well understood. Here, we use recently developed rapid MRI techniques for studying granular flows [1] to characterize the dynamics of interacting bubbles and jets injected into a fluidized bed.

Methods: Measurements were performed using a 190 mm diameter fluidized bed within a custom-built 16-channel radiofrequency coil and a Philips 3T medical scanner. Engineered particles 1 mm and 3 mm in diameter consisting of agar shells encapsulating oil were fluidized incipiently by upward airflow. Echo planar imaging with the SENSE algorithm was used to image local particle concentration and this technique was combined with phase contrast imaging to measure local particle velocity. Bubbles were injected by sending pulses of air flow through adjacent gas orifices and jets were injected by sending a continuous flow of gas through the same orifices. The spatial resolution achieved was 3 mm by 3 mm within a 10 mm thick central vertical slice through the bed, and the temporal resolution was 7 ms for particle concentration images and 18 ms for particle velocity images.

Results and Discussion: Figure 1 shows two injected bubbles rising side-by-side, demonstrating that bubbles do not interact significantly in a bed of smaller particles, but bubble interaction leads to a bubble collapse instability in larger particles [2]. Bubble collapse is attributed to gas flow channeling to a slightly larger bubble, causing the smaller bubble to collapse. Figure 2 shows two injected jets interacting, showing that in small particles, bubbles break off from the jets in an alternating pattern, while in larger particles, bubbles break off simultaneously. For both phenomena, the difference in behavior between the smaller and larger particles is attributed to the permeability of a packing of particles to gas flow increasing with increasing particle size.

References:

[1] A. Penn, T. Tsuji, D. O. Brunner, C. M. Boyce, K. P. Pruessmann, and C. R. Müller, Sci. Adv. **3**, e1701879 (2017).
[2] C. M. Boyce, A. Penn, A. Padash, M. Lehnert, K. P. Pruessmann, and C. R. Müller, Phys. Rev. Fluids **4**, 034303 (2019).

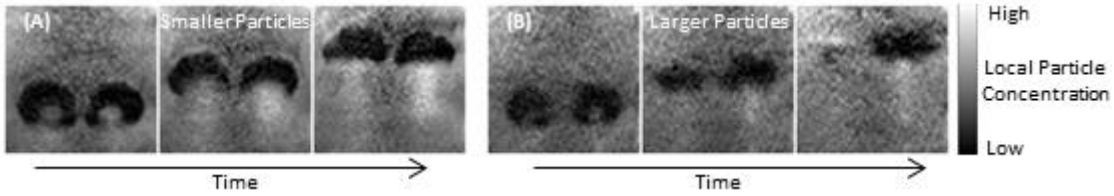

Figure 1. Rapid MRI measurements of two bubbles injected side-by-side into incipiently fluidized particles, showing (A) bubbles rising without significant interaction effects in smaller particles and (B) collapse of one bubble due to interaction in larger particles [2].

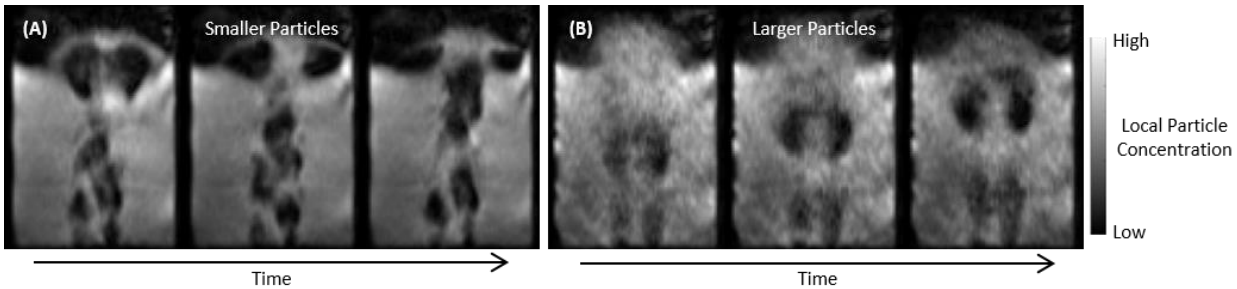

Figure 2. Rapid MRI measurements two jets injected side-by-side into fluidized particles, showing (A) alternating structured gas bubbling in smaller particles and (B) simultaneous structured gas bubbling in larger particles.

Monitoring slow motion in porous media using 3D propagator mapping

J. Wang[1], S. Haber-Pohlmeier[2], A. Pohlmeier[3], K. Pitman[1], M. Markwitz[1], A. Chan[1], P. Galvosas[1]
[1]MacDiamid Institute for Advanced Materials and Nanotechnology, School of Chemical and Physical Sciences, Victoria University Wellington, Wellington, New Zealand
[2]RWTH Aachen University, ITMC, Aachen, Germany
[3]Research Center Jülich, IBG-3, 5 Jülich, Germany

Introduction: NMR phase shifts and signal attenuation due to pulsed magnetic field gradients are commonly used in *q*-space imaging to monitor flow and diffusion of fluids in bulk or porous materials. If combined with *k*-space for regular Magnetic Resonance Imaging (MRI) *dynamic imaging* delivers spatially resolved maps of propagators [1, 2], holding the information on coherent motion (such as flow) and incoherent motion (such as diffusion or dispersion). Earlier work has adopted this approach for the 3D mapping of flow through sand using 13-interval stimulated echo multi-slice imaging (13-interval STEMSI) which allowed to monitor velocities as small as 60μm/s [3]. 13-interval STEMSI also reduced the influence of the gradient cross-term originating from sample inhomogeneities using alternating pulsed field gradients as proposed in [4]. Here we report on the further development of the 3D mapping method by augmenting 13-interval STEMSI with the concepts of Stimulated Echo Acquisition Mode (STEAM) Imaging [5].

Methods: While the original 13-interval STEMSI was designed as a multi-slice imaging method only one out of five radio frequency pulses were slice selective [3]. This is of no concern for samples which do not change over time, however, the intended application for the 13-interval STEMSI was to monitor water flow in and around plant roots. Here, the growing root system imposes a severe time constraint for the acquisition of the 6D data set (a 3D velocity vector needs to be mapped on a 3D image) which required rapid interleaved acquisition. The 13-interval STEMSI was therefore redesigned only using slice selective radio frequency pulses where STEAM [5] was used for the stimulated echo backbone of the pulse sequence.

Results and Discussion: Using slice selective radio frequency pulses exclusively allowed to acquire imaging data in the currently selected slice while all other slices undergo T_1 relaxation. This enables rapid iteration through all slices during one relaxation delay of $5\times T_1$. While this concept is known from medical imaging here it was combined with *dynamic imaging* suitable for the application in porous materials with substantial susceptibility heterogeneities. Experimental procedures have been optimised, tested and validated on various samples and phantoms. While imaged Lego® pieces ensured that image acquisition is free of spatial distortion three flow phantoms have been used to verify accurate flow acquisition. a) Flow in a pipe allowed the acquisition of parabolic flow profiles while cross-validating total flow rates. b) Flow through a column of glass beads with a diameter of about 1.5 mm was used to obtain regular images and flow patterns. c) Vertical flow through a sand column ensured consistency with results earlier obtained in [3]. The thus optimised experimental protocol was eventually used for the acquisition of flow in plant root systems.

Conclusion: 13-interval STEMSI was re-implemented using slice selective radio frequency pulses only. This allows rapid image data acquisition in interleave slices, thus minimising the acquisition time while maximizing signal-to-noise ratios after careful optimisation of experimental parameters.

References: [1] Callaghan, J. Phys. E **21** 820-822 (1988). [2] Callaghan, *Translational Dynamics & Magnetic Resonance*. Oxford University Press, (2011). [3] Spindler, J. Magn. Reson. **212** 216-223 (2011). [4] Cotts, J. Magn. Reson. **83** 252-266 (1989). [5] Frahm, J. Magn. Reson. **64** 81-93 (1985).

A Low-field NMR detector for probing *in situ* SABRE hyperpolarisation

Fraser Hill-Casey[1], *Kieran Marsh*[1], *Matheus Rossetto*[1], *and Meghan E. Halse*[1]
[1]Department of Chemistry, *University of York, York, UK*

A signature trait of NMR spectroscopy is the limited sensitivity due to the low, field-dependent polarisation across nuclear spin states. Several hyperpolarisation methods have been developed to overcome this sensitivity barrier such as Dynamic Nuclear Polarisation (DNP), Spin Exchange Optical Pumping (SEOP), and *Para*hydrogen-Induced Polarisation (PHIP). While DNP and SEOP require expensive and complex instrumentation, p*ara*hydrogen (p-H_2) based methodologies can be implemented using relatively low-cost and compact devices. In particular, the non-hydrogenative PHIP method, called Signal Amplification By Reversible Exchange (SABRE), provides a promising method to generate renewable hyperpolarisation on a time-scale of tens of seconds in a cost-efficient manner [1].

SABRE catalytically transfers spin order from p-H_2, the nuclear singlet isomer of H_2, to the target analyte via a reversible exchange reaction mediated by a transition-metal catalyst in solution. Polarisation transfer is achieved in the very low field regime (0 – 10 mT) prior to signal detection in the NMR spectrometer. The SABRE hyperpolarisation method has been successfully implemented to provide polarisation levels on the order of tens of percent for ^{1}H [2] and ^{15}N [3] for a range of N-heterocyclic compounds that bind reversibly to the SABRE catalyst on a suitable timescale. However, a limiting factor to the more widespread application of SABRE-based techniques is the optimisation of polarisation transfer to new classes of molecules and to other nuclei.

In this work, we describe an instrument that allows for the SABRE polarisation transfer process to be probed in the field in which it takes place. This instrumentation will allow for a comprehensive investigation into the polarisation transfer process, including the interplay between the spin dynamics that drives polarisation transfer, the kinetics of the chemical exchange of both the substrate and p-H_2, and NMR relaxation. Crucially, this scheme provides the ability to probe the magnetic states created and their relaxation properties without the complication of sample transport through ill-defined magnetic field gradients typically experienced when the sample is transferred between the polarisation transfer field and the NMR detector. The major components of this system consist of a low cost, liquid nitrogen based p-H_2 generator to provide a variable (~52-60 %) level of p-H_2 enrichment, a computer controlled sample polarizer and a variable field NMR detector, which operates over the range from 10 mT down to the Earth's magnetic field (~ 50 μT). This work will focus on the combination of these elements to produce an integrated and flexible system that can be used to probe all aspects of the polarisation transfer process.

References

1. Adams R.W. et al., Science, 323, 1708-11 (2009).
2. Rayner P.J. et al., PNAS, 114 (16), E3188-E3194 (2017)
3. Theis T. et al., JACS, 137 (4), 1404-1407 (2015)

Author Index